



HAL
open science

Wear of hot forging tools: towards an objective optimization of the durability.

Nasrine Boualem

► **To cite this version:**

Nasrine Boualem. Wear of hot forging tools: towards an objective optimization of the durability.. Mechanics [physics.med-ph]. Université Polytechnique Hauts-de-France, 2024. English. NNT : 2024UPHF0026 . tel-04779884

HAL Id: tel-04779884

<https://theses.hal.science/tel-04779884v1>

Submitted on 13 Nov 2024

HAL is a multi-disciplinary open access archive for the deposit and dissemination of scientific research documents, whether they are published or not. The documents may come from teaching and research institutions in France or abroad, or from public or private research centers.

L'archive ouverte pluridisciplinaire **HAL**, est destinée au dépôt et à la diffusion de documents scientifiques de niveau recherche, publiés ou non, émanant des établissements d'enseignement et de recherche français ou étrangers, des laboratoires publics ou privés.

Thèse de doctorat
Pour obtenir le grade de Docteur de
L'UNIVERSITÉ POLYTECHNIQUE HAUTS-DE-FRANCE et l'INSA-HAUT-DE-FRANCE

Discipline, spécialité : **Mécanique, énergétique, génie des procédés, génie civil**

Présentée et soutenue par

Nasrine BOUALEM

Le 03/09/2024, à Valenciennes

École doctorale : École Doctorale Polytechnique Hauts-de-France (ED PHF n°635)

Équipe de recherche, Laboratoire : Laboratoire d'Automatique, de Mécanique et d'Informatique
Industrielles et Humaines (LAMIH UMR CNRS 8201)

**Wear of hot forging tools: towards an objective optimization
of the durability**

**Usure des outils de forgeage à chaud : vers une optimisation
objective de la durée de vie**

Devant le jury composé de

Présidente du jury :

Emmanuelle VIDAL-SALLE, Professeur INSA Lyon – LaMCoS UMR CNRS 5259

Rapporteurs :

Régis BIGOT, Professeur ENSAM Metz – LCFC EA 4495

Marion RISBET, Professeur Université de Technologie de Compiègne – Roberval CNRS FR 3272

Examineurs :

Jérémie BOUQUEREL, Maître de conférences HDR, Centrale Lille – UMET UMR CNRS 8207

Philippe BRISTIÉL, Docteur, STELLANTIS Poissy

Philippe MOREAU, Ingénieur de Recherche UPHF, LAMIH UMR CNRS 8201

Directeurs de thèse

Laurent DUBAR, Professeur UPHF, LAMIH UMR CNRS 8201

Mirentxu DUBAR, Professeur UPHF, LAMIH UMR CNRS 8201

Membres invités

José Gregorio LA BARBERA SOSA, Ingénieur d'étude UPHF, LAMIH UMR CNRS 8201

Tarik SADAT, Maître de conférences UPHF, LAMIH UMR CNRS 8201

Remerciements

Ce mémoire concrétise trois années de thèse effectuées au LAMIH CISIT à Valenciennes et à STELLANTIS Poissy. Je tiens d'abord à remercier Mme Mirentxu DUBAR et M. Laurent DUBAR, mes directeurs de thèse, qui ont assuré l'encadrement de mon travail.

Je tiens à exprimer toute ma reconnaissance à M. Philippe BRISTIEL pour m'avoir accueilli au sein du groupe STELLANTIS et pour son accompagnement précieux.

J'exprime toute ma gratitude à M. Philippe MOREAU, qui a également dirigé ce travail de recherche avec une grande implication.

Je remercie M. Régis BIGOT de l'ENSAM de Metz et Mme Marion RISBET de l'UTC pour l'intérêt qu'ils ont porté à ce travail et pour avoir accepté de l'examiner en tant que rapporteurs. Je remercie également Mme Emmanuelle VIDAL-SALLE de l'INSA Lyon, et M Jérémie BOUQUEREL de Centrale Lille pour avoir accepté d'examiner ce travail.

Je remercie également M. José Gregorio LA BARBERA SOSA et M. Tarik SADAT pour avoir partagé leur expérience et leur passion, notamment dans les domaines de la mécanique et de la métallurgie.

Ce travail doit beaucoup aux personnes de l'équipe technique, pour qui j'ai la plus grande estime, notamment M. Rudy DUBOIS et M. Raphaël DELTOMBE, qui m'ont été d'une aide précieuse pour les observations MEB et les analyses topographiques.

Finalement, je tiens à remercier ma famille, mes collègues et tous ceux qui ont contribué à rendre si agréable mon séjour au LAMIH et à STELLANTIS Poissy.

Bonne lecture...

Résumé

Durant le processus de forgeage à chaud, les outils sont soumis à des chargements mécaniques et thermiques cycliques sévères. Ces conditions de formage extrêmes peuvent endommager les outils par le développement d'usure abrasive, de fissuration, de fatigue thermique et mécanique. Ces dommages compromettent la résistance mécanique des outils et réduisent leur durée de vie. Pour optimiser la durée de vie des outils, plusieurs facteurs doivent être pris en compte, tels que les propriétés du matériau de l'outil, la géométrie de l'outil, l'oxydation, la lubrification et les paramètres de forgeage (température, pression et vitesse de glissement).

L'objectif de cette thèse est de comprendre comment le nombre de cycles de forgeage répétés impacte les outils de forgeage à chaud, en termes de modifications de l'état de surface, de changements des propriétés mécaniques et de la microstructure, de modifications géométriques, et de l'évolution du comportement tribologique. L'objectif est de proposer une étude tribologique qui considère l'état d'usure des matrices, avec la possibilité de l'intégrer dans des simulations numériques du processus de forgeage.

Tout d'abord, une détermination de la loi rhéologique de la nuance 38MnSiV5 (matériau de la pièce) est effectuée par des essais de compression dans l'objectif d'alimenter les simulations numériques des procédés de forgeage. Ensuite, pour étudier l'influence du cycle de forgeage sur l'état de surface des outils, une analyse topographique est réalisée sur des outils ayant différentes géométries et différents cycles de vie (nouvel outil, en cours de vie et en fin de vie). L'étude révèle que la rugosité de surface augmente tout au long du cycle de vie de l'outil en raison de phénomènes complexes tels que l'usure.

Les propriétés mécaniques, telles que la dureté et le module de Young des outils, sont également influencées par le cycle de vie de forgeage et par les changements des conditions de contact. Les tests de nano-indentation montrent une diminution de la dureté ainsi qu'une diminution ou une stabilisation du module de Young selon la zone et en fonction du cycle de vie. Les résultats des tests ont ensuite été corrélés avec les résultats de l'analyse microstructurale obtenus par SEM/EDS. Ils montrent la formation de fissures dans la couche d'oxyde et une transition de la martensite à la cémentite globulaire. De plus, la formation d'une couche de décarburation est constatée dans certaines zones, ce qui semble lié à la formation d'une couche d'oxyde non adhérente.

Une étude tribologique du procédé de forgeage est effectuée en utilisant le banc d'essai WHUST, qui sert à reproduire les conditions de contact du procédé industriel. Différentes géométries et configurations de conditions de contact sont analysées en fonction du cycle de vie. Cette analyse a révélé une stabilisation ou une diminution de l'indicateur de frottement à haute température. La présence d'oxydes et les changements de géométrie des outils influencent de

manière significative le comportement tribologique et d'usure : les couches d'oxydes, dont l'épaisseur augmente avec le nombre de cycles de forgeage, agissent comme des barrières thermiques, influençant le comportement de friction et d'usure des outils. Cependant, elles servent également de sites d'initiation de fissures, contribuant à l'endommagement de la surface au fil du temps.

Les modifications géométriques induites par l'usure affectent les conditions de contact et la performance globale des outils de forgeage. Les simulations numériques mettent en évidence que les changements de géométrie des outils entraînent des variations de la pression de contact et de la température.

Abstract

During the hot forging process, tools are subjected to severe cyclic mechanical and thermal loads. These extreme forming conditions can damage the tools through the development of abrasive wear, cracking, and thermal and mechanical fatigue. These damages compromise the mechanical strength of the tools and reduce their service life. To optimize the service life of the tools, several factors must be considered, such as the properties of the tool material, tool geometry, oxidation, lubrication, and forging parameters (temperature, pressure, and sliding speed).

The aim of this thesis is to understand how the number of repeated forging cycles impacts hot forging tools in terms of surface state modifications, changes in mechanical properties and microstructure, geometric modifications, and the evolution of tribological behavior. The objective is to propose a tribological study that considers the wear state of the dies, with the possibility of integrating it into numerical simulations of the forging process.

First, the rheological law of the 38MnSiV5 grade (workpiece material) is determined through compression tests to feed the numerical simulations of the forging processes. Next, to study the influence of the forging cycle on the surface state of the tools, a topographical analysis is performed on tools with different geometries and at different stages of their life cycle (new tool, mid-life, and end-of-life). The study reveals that surface roughness increases throughout the tool's life cycle due to complex phenomena such as wear.

Mechanical properties, such as hardness and Young's modulus of the tools, are also influenced by the forging cycle and changes in contact conditions. Nano-indentation tests show a decrease in hardness as well as a decrease or stabilization of Young's modulus depending on the area and life cycle stage. The test results were then correlated with microstructural analysis findings obtained through SEM/EDS. These analyses show the formation of cracks in the oxide layer and a transition from martensite to globular cementite. Additionally, the formation of a

decarburized layer is observed in certain areas, which appears to be related to the formation of a non-adherent oxide layer.

A tribological study of the forging process is conducted using the WHUST test bench, which replicates the contact conditions of the industrial process. Different geometries and configurations of contact conditions are analyzed according to the life cycle stage. This analysis revealed a stabilization or decrease in the friction coefficient at high temperatures. The presence of oxides and changes in tool geometry significantly influence the tribological and wear behavior: oxide layers, which increase in thickness with the number of forging cycles, act as thermal barriers, affecting the friction and wear behavior of the tools. However, they also serve as crack initiation sites, contributing to surface damage over time.

Geometric modifications induced by wear affect the contact conditions and overall performance of the forging tools. Numerical simulations highlight that changes in tool geometry lead to variations in contact pressure and temperature.

Table of Contents

Table of Contents	6
Figures and Tables.....	8
General introduction	13
Chapter 1. Hot forging of crankshafts: design, life cycle, wear and oxidation of dies	17
1.1. Hot forging of crankshaft.....	18
1.2. Hot forging die	23
1.2.1. Chemical composition of die material.....	23
1.2.2. The role of alloying elements	23
1.2.3. Machining and Heat Treatments of the dies	24
1.2.4. Nitriding of hot forging dies	26
1.3. Microstructural analysis after heat treatment and nitriding	27
1.4. Die failure causes	29
1.5. Damage mechanisms of hot forging tools.....	31
1.5.1. Wear Mechanisms.....	32
1.5.2. Thermal fatigue.....	34
1.5.3. Mechanical fatigue	36
1.6. Oxidation of steels during hot working	37
1.7. Conclusion	40
Chapter 2. Rheological behavior determination of 38MnSiV5 steel grade at high temperature ..	43
2.1 Preliminary thermal cycle to replicate the required grain size.....	44
2.2 Mechanical behavior of 38MnSiV5 steel grade at high temperatures	48
2.2.1. Compression tests procedure.....	48
2.2.2. Compression test results	50
2.2.3. Correction of stress-strain curves	51
2.3. Conclusion	58
Chapter 3. Influence of hot forging cycles on the topography and mechanical properties of the tool	60
3.1. Identification of the analysed zones.....	61
3.2. Influence of hot forging cycles on the topography	65

3.2.1. Methodology for topography analysis	65
3. 2.2. Results and Discussion	66
3.2.3. Conclusion	71
3.3. Influence of hot forming cycles on the mechanical properties of hot forging tool.....	71
3.3.1. Experimental Procedures	71
3.3.2. Results and Discussion	73
3.3. Conclusion	85
Chapter 4. Influence of hot forging cycles on the tribological behavior of the die	87
4.1. Parameters affecting friction.	88
4.2. Methodology of tribological tests	89
4.3. Numerical Determination of the tribological conditions	90
4.4. Oxides Analysis	92
4.5. Tribological tests	96
4.6. Results and discussion	977
4.6.1. Friction analysis.....	977
4.6.2. Surface contact analysis.....	99
4.6.3. Summary of friction results	103
4.6.4. Summary of topography results.....	104
4.7. Influence of oxides and geometry changes on contact conditions	105
4.7.1. The influence of oxides on thermal and mechanical contact.....	108
4.7.2. The influence of the geometry-on thermal and mechanical contact	109
4.8. Numerical analysis of the influence of geometric variations on contact pressure: Approach with the assembly of real geometries	1111
4.9. Conclusion	1155
General conclusion.....	118
References	122
Appendix 1 : Data for all curves after corrections and fitting	1277
Appendix 2: Evolution of the topography of the tool as function of lifecycles.....	1366
Appendix 3 : Evolution of the topography of the WHUST specimens as function of lifecycles.....	137

Figures and Tables

Figure 1: Some car brands manufactured by Stellantis.	13
Figure 2: Die forging at Stellantis Mulhouse	18
Figure 3: Crankshaft designed for three-cylinder petrol engines.....	19
Figure 4: Time-Temperature diagram of 38MnSiV5 steel	20
Figure 5: Diagram of the hot forging process of the crankshaft.	21
Figure 6: The 3 steps of the forging of the crankshaft on the mechanical press at Stellantis	21
Figure 7: Pieces obtained after hot forging steps: a) after distribution, b) after roughing, c) after finishing	22
Figure 8: The different heat treatments undergone by Stellantis dies (ϵ = Low proportion).....	24
Figure 9: The microstructure of X38CrMoV5 in the annealed state	25
Figure 10: Hardness evolution as a function of the second tempering temperature of X38MnSiV5 steel (Barrau O., 2004)	26
Figure 11: a) Structure of the nitrided layer, etched with Nital, b) Tempered martensitic structure in lamellae, etched with Nital.....	28
Figure 12: Angel hairs in nitrided layer	28
Figure 13: Die Failure causes (Chander & Chawla, 2017).	29
Figure 14: Example of cracks observed after crankshaft hot forging.	30
Figure 15: Die damages mechanisms shown here at various points on the lower die (Lange <i>et al.</i> , 1992) (Grobaski, 2004).	31
Figure 16: Hot forging dies wear mechanisms (Abachi, Akkök, & Gökler, 2010) (Kim, <i>et al.</i> , 2006)	32
Figure 17: The presence of wear on the hot forging dies for crankshaft (20,000 cycles) at Stellantis	34
Figure 18: Thermal fatigue observed in the hot forging die for crankshafts (20,000 cycles) at Stellantis.	35
Figure 19: Mechanical crack formed on the H21 steel during hot forging process in the inner corner radius (a) after about 2400 forging cycle (b) crack 's close – up indicated in (a), (c) after about 4200 forging cycles, (d) crack 's close –up indicated in (c) and (e) dispersion of cracks after about 5200 forging cycles on the surface of the die. (Emamverdian, <i>et al.</i> , 2021).....	36
Figure 20: Mechanical fatigue observed in the hot forging die for crankshafts (20,000 cycles) at Stellantis	37
Figure 21: The impact of heating temperature on oxide scale composition (Behrens, <i>et al.</i> , 2018)	38
Figure 22: Classical three-layer oxide scale system (Graf, <i>et al.</i> , 2013). (Serebriakov, 2020).....	38
Figure 23: The decomposition of the oxide layer into strata based on their composition on X38CrMoV5 (Barrau O., 2004)	39

Figure 24: Sample preparation for determining the prior austenitic grain size in the billet: a) initial geometry of the billet, b) dimensions of the piece extracted from the billet, c) location of 8 samples to measure the grain size.	45
Figure 25: Micrographs of sample 1 (Figure 24c) obtained from the billet heated at 1290 °C and quenched in water.	45
Figure 26: Grain size distribution in the billet	46
Figure 27: Comparison between the grain size distribution of the industrial billet and the grain size distributions of samples obtained after thermal etching at 1220°C and 1250°C.....	48
Figure 28: Diagram of the thermomechanical treatments of the compression tests	49
Figure 29: a) General view of the Gleeble machine. b) Test chamber of the Gleeble 3500 before the compression test. Localization and description of the elements of the test.	49
Figure 30: Stress-strain raw curves at different temperatures and strain rates.	50
Figure 31: Stress-strain curves for the condition 950°C-0.01s-1 before and after friction correction.	54
Figure 32: Characteristic stress-strain curves of a material subjected to work hardening (WH), dynamic recrystallization (DRV), and dynamic recovery (DRX) (Chalon, 2016).	54
Figure 33: Evolution of the saturation stress as a function of the Zener-Hollomon parameter. ...	56
Figure 34 : Stress-strain curves, at different temperatures and strain rates, before and after all corrections	57
Figure 35: The selected zones: concave (1), convex (2), flat (3) and bottom of the engraving (4)	621
Figure 36: Temperature measurement results of the convex zone after forging and after lubrication: (a) target area, (b) thermal picture	64
Figure 37: a) Measurement zone: Convex zone , b) CAD model, c) 3D printed mold, d) replica of the area	65
Figure 38: Interferometer photo and measurement parameters.	66
Figure 39: Arithmetical mean height (Sa) evolution as a function of the die's life cycle.	68
Figure 40: The evolutions of Sp and Sv parameters as a function of the die's life cycle.....	68
Figure 41: Hysitron TI 980 TriboIndenter nanoindenter	72
Figure 42: Nano-indentation test sample (0 cycle convex zone)	72
Figure 43: Evolution of Hardness versus position in the tool depth and tool life (convex zone). 73	
Figure 44: Evolution of Hardness versus grid number in the tool depth (convex zone 0 cycle) ..	74
Figure 45: Evolution of Hardness versus position in the tool depth and tool life: (a) concave zone, (b) flat zones	75
Figure 46: Evolution of Young's modulus versus position in the tool depth and tool life (convex zone)	76
Figure 47: Evolution of Young modulus versus position in the tool depth and tool life : (a) concave zone, (b) flat zones.	76
Figure 48: SEM images of the microstructure of a new nitrided tool (3 % nital etching).....	77
Figure 49: SEM images of the microstructure of a new nitrided tool (no etching)	78

Figure 50: SEM images of the microstructure of convex zone at: 11800 cycles (a) and 20000 cycles (b)	78
Figure 51: SEM images of samples from the convex zone at 11800 and 20000 cycles.	80
Figure 52: TRC Diagram of X38CrMoV5 Steel (Salem, 2009)	81
Figure 53: The EDS spectra extend up to 5 keV for the convex zone at different lifecycle stages (0; 11,800; 20,000 cycles).	82
Figure 54: SEM images of samples from the concave zone at 11800 and 20000 cycles.	83
Figure 55: The EDS spectra extend up to 5 keV for the concave zone at different lifecycle stages (0; 11,800; 20,000 cycles).	83
Figure 56: SEM images of samples from the flat zone at 11800 and 20000 cycles.	84
Figure 57: The EDS spectra extend up to 5 keV for the flat zone at different lifecycle stages (0; 11,800; 20,000 cycles).	85
Figure 58: Parameters affecting friction (Klocke, 2013)	88
Figure 59: The methodology used to replicate the contact conditions on the WHUST test bench.	89
Figure 60: Photograph of the WHUST test bench and its operating principle	90
Figure 61: The numerical model used for the forging process simulation (Stellantis)	91
Figure 62: Contact pressure evolutions for the concave, convex, and flat zones: a) as a function of temperature, b) as a function of sliding velocity.	91
Figure 63: Energy dispersive spectroscopy (EDS) analysis on the convex zone at lifecycles 11,800 and 20,000 cycles.	93
Figure 64: SEM Images: a) Sample from the billet, b) Sample from the WHUST specimen.	93
Figure 65: Energy dispersive spectroscopy (EDS) analysis on the oxides originating from the industrial billet and the WHUST specimen.	94
Figure 66: X-ray diffraction (XRD) analysis on the convex zone at lifecycles 11,800 and 20,000 cycles.	95
Figure 67: (a) tribometer set-up (b) heating induction system for the specimen.	96
Figure 68: Example of the geometry of the contact surfaces :1) concave, 2) convex, 3) flat	97
Figure 69: Example of the evolution of normal (F_n) and tangential (F_t) forces as a function of displacement (WHUST test with convex contactor at 11,800 cycles)	98
Figure 70: Images of WHUST specimens after the WHUST test and the top view of the convex contactors (condition 350MPa-10mm/s-1250°C) at different lifecycles (0;11,800 and 20,000 cycles).....	1000
Figure 71: Topography of convex contactors at the condition: 350MPa-10mm/s-1250°C and at different lifecycles (0;11,800 and 20,000 cycles).....	1011
Figure 72: The evolutions of S_a (Arithmetical mean height) parameter as a function of the die life cycle of convex contactors at the condition: 350MPa-10mm/s-1250°C	1022
Figure 73: The evolutions of S_v (Valley Depth) and S_p (Maximum peak Height) parameters as a function of the die's life cycle of convex contactors at the condition (350MPa-10mm/s-1250°C).....	1022

Figure 74: a) Tool radii (new tool: 8mm, mid-life: 9mm; end of life: 10mm, b) Primary input parameters for numerical simulation.	1077
Figure 75: The numerical results of the surface temperature for the billet and the tool, with and without oxides.	10808
Figure 76: The numerical results of the contact pressure experienced by the billet and the tool : (a) with oxides, (b) without oxides.	10909
Figure 77: The numerical results of the temperature experienced by the billet in contact with three different tool geometries (radius 8, 9, and 10 mm) representing three different stages of tool life.	1100
Figure 78: The numerical results of the contact pressure experienced by in contact with three different tool geometries (radius 8, 9, and 10 mm) representing three different stages of tool life (new, mid-life, and end-of-life).....	1111
Figure 79: The 2D model of the numerical simulation using ABAQUS.....	1122
Figure 80: a) Three zones: convex, concave, and flat on the surface of the hot forging die, b) schematic of the tool geometry showing the assembly of the three zones.	1122
Figure 81: Evolution of contact pressure versus position for the 3 die zones (Concave, Convex, and Flat) at different lifecycle stages for initial tightening	1143
Figure 82: a) Mean contact pressure, b) Maximum contact pressure	1144
Figure 83: Results of the 2D model of the numerical simulation using ABAQUS	1144
Figure 84: Effect of surface temperature and holding time on the lubricant remaining on the surface (Sin' czak, 2007)	1200
Table 1: Chemical Composition of 38MnSiV5 (%m)	19
Table 2: Time of presence of the billet in each step of hot forging.....	22
Table 3: The chemical composition of X38CrMoV5 (measured in mass %) is monitored using a spark spectrometer at the Central Tooling department at Stellantis Mulhouse.	23
Table 4: Factors affecting wear (Chander <i>et al.</i> , 2017).....	32
Table 5: Factors affecting abrasive wear (Singh, 1973).....	33
Table 6: Oxide layer thickness variation vs temperature in the presence of water vapor on the virgin material (Bruckel, 2003).....	39
Table 7: Experimental design of thermal etchings at 1250°C and 1220°C with the corresponding holding times and heating rates. Mean austenitic grain size obtained after etching.	47
Table 8: Friction coefficient (μ) values as a function of deformation temperature and strain for 20MnCr5 steel grade (Puchi-Cabrera <i>et al.</i> 2019).....	52
Table 9: Friction coefficient (μ) values after interpolation and extrapolation computations using MATLAB.....	53
Table 10: Pictures of the concave, convex, flat, and engraving bottom zones during the lifespan cycles.	63

Table 11 : Maximum temperature T_{\max} and maximum contact pressure P_{\max} from numerical simulation of the hot forging of the crankshaft.....	64
Table 12: Roughness parameters and their relationships with damage phenomena (Jaber. A, 2022)	67
Table 13: The evolution of the topography of the different zone as a function of the lifecycle ...	70
Table 14: Local contact conditions for each geometric zone	92
Table 15: The average thicknesses of the oxides for the concave, convex, and flat zones at 11,800 and 20,000 cycles.....	96
Table 16: Evolution of the friction indicator I_F as a function of lifecycle for the convex zone at the condition: 350MPa-10mm/s-1250°C	99
Table 17: Evolution of the friction indicator as a function of lifecycle for each condition (Table 1)	1033
Table 18: The evolutions of S_a , S_p and S_v parameters as a function of the die life cycle of all conditions.....	105
Table 19: Mechanical and thermal properties of the oxides and carbon steel at high temperature (Angelo <i>et al.</i> ,2016).....	107
Table 20: The average radii determined for the concave and convex zones at different lifecycles.	1133

General introduction

In a world where environmental awareness is becoming increasingly important, eco-design and product sustainability are becoming imperatives for companies. Stellantis, a global leader in the automotive industry, is firmly committed to this approach, adopting a holistic view of the lifecycle of its products. The company is the result of the merger between two giants of the automotive industry, Fiat Chrysler Automobiles (FCA) and Groupe PSA, in January 2021. This merger has created a new entity that brings together iconic automotive brands (Figure 1) such as Fiat, Jeep, Peugeot, Citroën, and Opel. Stellantis, with a workforce of over 400,000 people, operates globally, with a presence in more than 130 countries and a diverse range of products, from passenger cars and light commercial vehicles to luxury and electric vehicles.



Figure 1: Some car brands manufactured by Stellantis.

The company doesn't only lead in technological innovation, but it is also committed to eco-design, the sustainability of parts and tools, and the promotion of the circular economy. From conception to the end of the vehicle life, every stage is planned to minimize the environmental impact. This includes the use of recycled and recyclable materials, the implementation of resource-efficient production processes, as well as efforts to extend vehicle life through reuse, repair, and recycling programs. In this way, the durability of parts and tools is an important aspect of Stellantis' business. The materials used are carefully selected for their resistance to wear and corrosion, ensuring the reliability and longevity of the products.

In order to reduce environmental impact, and the costs of production, Stellantis aims to increase the lifecycle of its production tools. The study and analysis of degradation, wear, and damage of hot forging tools remain significant challenges. In this context, a partnership has been established between Stellantis and LAMIH (Laboratory of Automatics, Mechanics, and Industrial and Human Computer Science UMR CNRS 8201) under a CIFRE agreement managed by the French National Association for Research and Technology (ANRT).

The work conducted in this research focuses on studying the wear of hot forging tools throughout their lifecycle. The tools under investigation are produced at the Stellantis Mechanical Plant located at the Mulhouse site. Mechanical Plant has three operational departments: foundry, central tooling, and forging. The Central Tooling department designs, manufactures and markets tools, including dies that are used for stamping or casting components. The Foundry produces aluminum die-castings, supplying cylinder blocks and bearing caps. The Forging department employs a combination of manual and automated manufacturing machines, facilitating the production of specific engine assembly parts, such as connecting rods, pinions, shafts, crankshafts, crown, etc...

While the hot forging process gives the part the mechanical strength and the metallurgy adapted service conditions, its main disadvantage is the failure of tools due to repeated and significant mechanical, thermal, and tribological stresses (Alimi, 2016).

The average lifecycle of Stellantis forging tools (also known as forging dies) is around 20,000 manufactured pieces for the tool under investigation. However, a tool may be at the end of its life after 15,000 parts, or after 25,000 parts, for reasons often unknown to the manufacturer. This tool lifecycle depends on various factors, including the materials used for fabrication, the thermal and thermochemical treatments undergone by the tooling prior to its use, the geometry (design) of the tools, the choice of lubricant used in forging, and the thermomechanical stresses during the hot forging process (Gronostajski, Hawryluk, Kaszuba, & Ziemba, 2016) (Kumar, 2014) (Daouben, 2008).

Different constraints encountered during hot forging include mechanical loads, extreme thermal conditions (heating temperature, heating due to friction and plastic deformation of the parts), and chemical stresses (reactivity of surfaces in the presence of lubricant, oxidation of the part) (Serebriakov, 2020). These constraints lead to surface deteriorations of the dies. These damages are typically mechanical and thermal fatigue, abrasive and adhesive wear, and rarely plastic deformation. These phenomena significantly alter the mechanical durability of the tools and reduce their lifecycle (Gronostajski, 2019). Tool failure doesn't only result in a production line shutdown but also requires considerable time for replacement and adjustment, which is unacceptable in an industrial context. Stellantis' knowledge regarding the damage and wear phenomena of forging tools still needs to be completed. Process control in forging is driven by

numerical simulation, but it is currently limited to the analysis of the manufactured component. Regarding the tools, the available information is limited to general indications, without a comprehensive consideration of the changes they undergo throughout their lifecycle.

The aim of the research carried out in this thesis is to understand how the number of repeated forging cycles impacts hot forging tools, in terms of modifications to the surface state, changes in mechanical properties and microstructure, and geometric modifications. The main observations will therefore be tribological. The objective is to propose a tribological study that considers the wear state of the dies, with the possibility of integrating it into numerical simulations of the forging process.

The crankshaft forging process was selected for investigation. This choice is based on both the complexity of the tooling geometry and the challenges encountered during the forging operation of this crankshaft. The crankshaft is a rich object of learning. The tool surface consists of different zones with varying geometries (flat, concave and convex surface), each of them being subjected to different contact conditions in terms of sliding velocities, contact pressure, temperature levels, contact time.

Carrying out tests and measurements on-site is complicated because of production constraints, accessibility to the forming area and the significant costs that such measures could involve. One of the solutions is to carry out characterisation and analysis tests under conditions close to industrial conditions in a scientific laboratory.

To address the research objectives, the study will be structured around four chapters. The first chapter presents and describes in detail the different stages in the forming of crankshafts, the manufacture of the tool, the failures and damage observed on the tools and previous studies conducted on the tool grade. The second chapter focuses on the formulation of a rheological law for the billet, incorporating more precise data in line with the need to improve numerical forging simulations. The third chapter concerns the study of the influence of forging cycles on the topography and near-surface mechanical properties, specifically carried out on the rough lower forging die. The final chapter examines the influence of forging cycles on the tribological behavior of hot forging tools.



Chapter 1. Hot forging of crankshafts: design, life cycle, wear and oxidation of dies

This chapter presents and describes the different steps of the crankshafts forging and tools production. Then, the chemical composition and microstructure of the grade used and the machining steps of the hot-forging tools, the failure and damage observed on the tools throughout their lifecycle are presented. Finally, a dedicated literature review on the oxides appearing on billets and tools during the hot forging concludes this chapter.

1.1. Hot forging of crankshaft

Hot forging is a metal forming process that involves forming a malleable metal part, often referred to as a billet or workpiece, into a specific shape using various techniques such as hammering, upsetting, stamping, die forging (Figure 2). These processes are carried out when the temperature of the workpiece is approximately 75% of its melting point (Liitjhering & Williams, 2007).



Figure 2 : Die forging at Stellantis Mulhouse.

For the purpose of this research, the hot forging of the crankshaft designed specifically for three-cylinder petrol engines (Figure 3) was selected for this study. The material grade used is 38MnSiV5 steel grade (Table 1).



Figure 3: Crankshaft designed for four-cylinder petrol engines.

Table 1: Chemical Composition of 38MnSiV5 (% m).

Elements	C	Mn	Cr	Si	P	Al	Ti	Mo	N	Cu	S
% m	0,36- 0,40	1,20- 1,50	0,10- 0,20	0,50- 0,80	≤ 0,02	0,01- 0,04	≤ 0,02	≤ 0,06	≥ 0,01	≤ 0,30	0,03- 0,06

In the forging unit at the Stellantis Mulhouse site, steel bars (6 meters length) made of 38MnSiV5, undergo a cold-cutting process to create cylindrical billets measuring 316 mm in length and 85 mm in diameter. Once the billets are cut, they are then transported to production zone. The billet is then heated. The heating process, an important initial step, involves subjecting the billet to temperatures ranging from 1270°C to 1290°C using an induction heater for approximately 320 seconds. The heating power employed is 1.8 MW, representing half of the maximum power of the heater (3.4 MW). Throughout the heating process, the temperature of the hot billet is closely monitored at the heater's outlet by a pyrometric sensor. During heating, a change in the initial

microstructure of the 38MnSiV5 steel (ferrite + pearlite) takes place. The crystalline structure gradually transforms into austenite (Figure 4) from 815°C and then grain growth occurs.

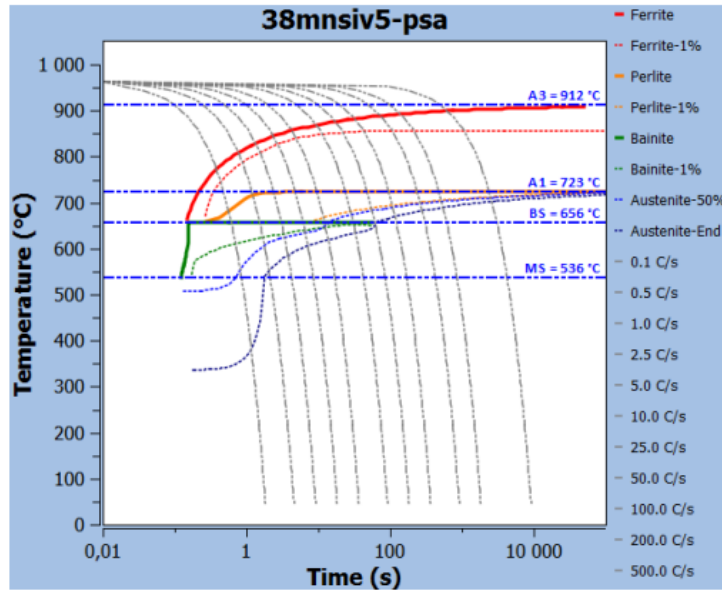


Figure 4 : Time-Temperature diagram of 38MnSiV5 steel.

Following the heating step, the billets, now at the optimal temperature, are transferred from the induction heater to the mechanical press using a robot. The entire transfer operation takes approximately 15 seconds.

A mechanical press is used to produce the crankshafts at a rate of 250 pieces per hour. There are three main steps in the forging of the crankshaft (Figure 5), in which the billet is handled on six dies preheated to a temperature of around 140°C:

- the distribution step: this step involves the distribution of material to facilitate subsequent steps.
- the roughing step: this step involves shaping the rough billet (Figure 6) and (Figure 7a and 7b), which closely resembles the finished one (Figure 6) and (Figure 7c). The volume ratio between the two stages is low, typically just a few percent. The rough billet has narrower dimensions to avoid folds and filling defects during the finishing step.
- the finishing step: this is the final forging step that results in achieving the final geometry of the billet, requiring very little machining to obtain a finished billet (Figure 6) and (Figure 7).

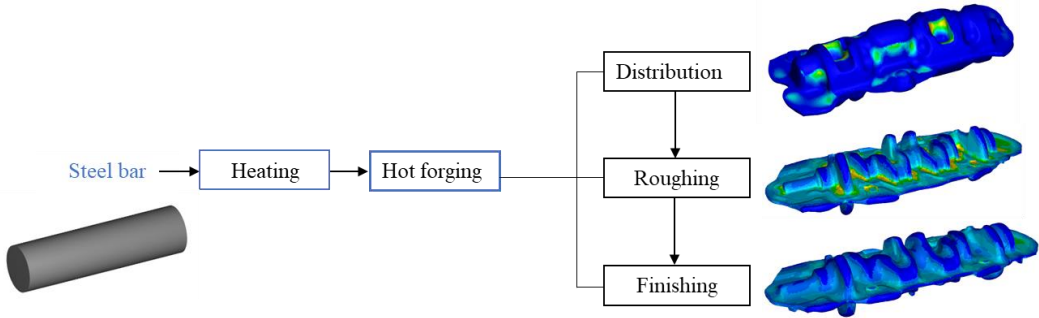


Figure 5: Diagram of the hot forging process of the crankshaft.



Figure 6: The 3 steps of the forging of the crankshaft on the mechanical press at Stellantis.

Time measurements are presented in Table 2. These times include the positioning of the billet on the tool, the press stroke and the time taken for the part to be picked up by the transfer system.

Table 2: Time of presence of the billet in each step of hot forging

Step	Time (s)		
	The billet on the lower die	Forging stroke	Transfer by robot
Distribution	2	0.5	2
Roughing	4	0.2	
Finishing	3	0.3	

When the impressions are empty, a spray system applies lubricant (1 liter of liquid for each piece, a mixture of 25% of graphite-based lubricating liquid and 75% water), and cold air is blown to remove oxides. The air and especially the evaporation of the water have a relative cooling effect on the tool. The finished workpiece is transferred by robot to the hydraulic press used for deburring, the excess material, known as the burr, is removed from the workpiece profile.

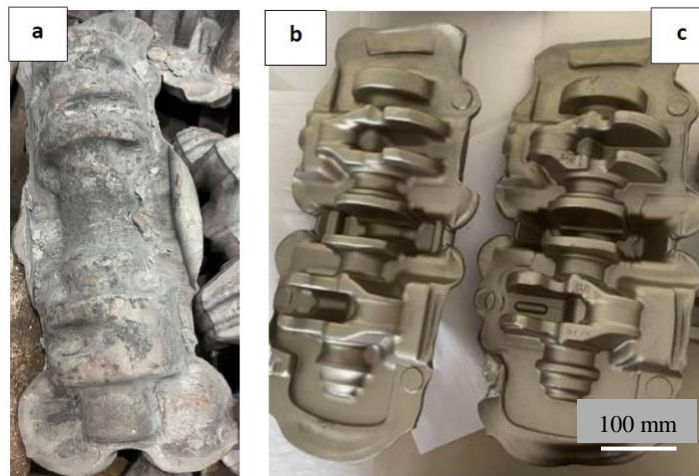


Figure 7: Pieces obtained after hot forging steps: a) after distribution, b) after roughing, c) after finishing.

1.2. Hot forging die

Crankshaft forging process requires the design, manufacture, and maintenance of complex tools, specifically customized dies for each part. This is carried out at the Central Tooling department of Stellantis. The cost of the raw material comprising the tooling, in addition to machining and both mass and surface treatment, accounts for 5 to 15% of the overall cost of the parts produced through the process.

1.2.1. Chemical composition of die material

The selection of die material for forging applications is primarily contingent on factors such as the temperature generated within the dies, the applied load, and the cooling method employed for the dies. Most hot work tool steels belong to the category of low carbon steels and are alloyed with medium to high alloying elements. Detailed compositions of hot work tool steels under the AISI standard can be found in literature (Altan, Ngaile, & Shen, 2004).

Stellantis use X38CrMoV5 steel grade to produce crankshaft forging tools. X38CrMoV5 falls into the category of steels that are resistant to thermal shock, it is characterized by low to medium carbon content, along with alloying elements such as nickel, chromium, molybdenum, and vanadium (Table 3).

The Central Tooling department at Stellantis Mulhouse site receives parallelepiped blocks of X38CrMoV5 steel with dimensions ($700\text{ mm} \times 270\text{ mm} \times 170\text{ mm}$) and a weight of 250 kg from four different suppliers. Upon receipt, the laboratory of the central tooling department checks the chemical composition of the steel comply with the standard. An analysis of the chemical composition (Table 3) is conducted using a spark spectrometer on samples extracted from one of the blocks.

Table 3: The chemical composition of X38CrMoV5 (measured in mass %) is monitored using a spark spectrometer at the Central Tooling department at Stellantis Mulhouse.

% m	C	Mn	Si	S	P	Cr	Mo	V	W	Co	Ni	Cu
min.	0,34	0,2	-	-	-	4,80	1,20	0,40	-	-	-	-
max.	0,42	0,50	1,20	0,010	0,025	5,50	1,50	0,60	0,20	0,20	0,20	0,20

1.2.2. The role of alloying elements

The alloying elements play an important role in the thermomechanical properties of steel and therefore have a significant impact on the flow of the material. Notably, chromium enhances the hardenability of the steel which in turn reduces grain coarsening during austenitization and delays softening during tempering and contributes to reduced high-temperature oxidation. It also

forms carbides that enhance abrasion resistance (Barrau, Boher, Gras, & Rezai-Aria, 2003) (Alimi, 2016).

In addition, molybdenum provides the steel with excellent resistance to hot wear through the presence of extremely hard carbides ranging from 1500 (M_6C) to 2000 Hv (M_2C) and delays softening. (Barrau, Boher, Gras, & Rezai-Aria, 2003).

On the other hand, vanadium helps generating hard carbides (MC 3000 Hv). Small additions (up to 0.2% by mass) are highly effective in preventing grain coarsening during heat treatment. In tool steels, it is commonly used in conjunction with chromium, molybdenum, and tungsten. Its poor oxidation resistance beyond $600^\circ C$ is compensated by the presence of chromium. Additionally, the carbon content of the steel is closely related to the vanadium content, which is limited by hardenability, forgeability after quenching, and tempering concerns (Barrau O., 2004) (Alimi, 2016).

Finally, Silicon is used as a deoxidizer in the liquid steel during the final stage of production. Contents of approximately 1% result in an increase in yield strength, oxidation resistance beyond $1000^\circ C$, and hardenability due to constructive collaboration with other alloying elements like molybdenum. It also helps reducing the stability of M_2C carbides, thereby decreasing the metal brittleness (Barrau, Boher, Gras, & Rezai-Aria, 2003).

1.2.3. Machining and Heat Treatments of the dies

The die machining process at Stellantis begins with High-Speed Machining (HSM). Then, the dies undergo bulk heat treatments followed by electrical discharge machining (sinking machining). After the machining stage, the dies undergo heat treatments (Figure 8) in a vacuum furnace. Heat treatments are especially important processes that determine the microstructure of the steel and, consequently, the mechanical properties of the material.

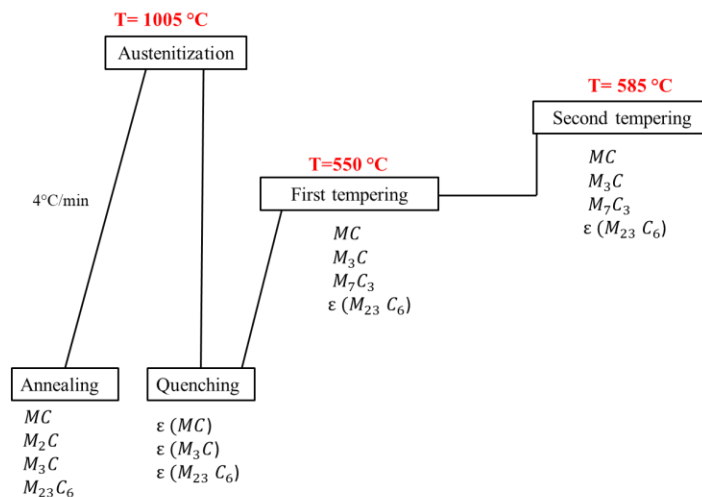


Figure 8: The different heat treatments undergone by Stellantis dies (ϵ = Low proportion).

Firstly, steel undergoes an annealing process to homogenize its structure, which consists of alpha ferrite and carbides at that point (Figure 9). This annealing softens the material and makes it more workable (Alimi, 2016). In the annealed state, the metal has a hardness of around 20 HRC.

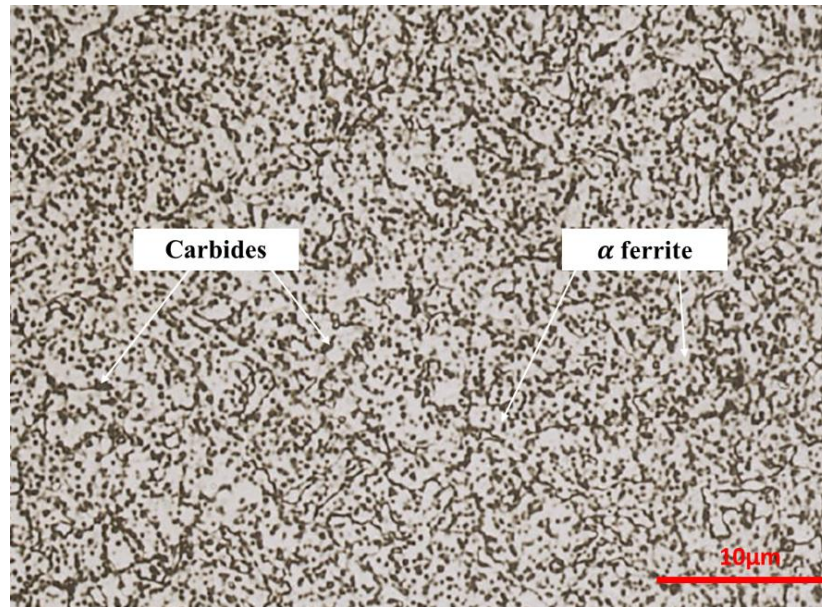


Figure 9: The microstructure of X38CrMoV5 in the annealed state.

Temperature is elevated to 1005°C at a controlled heating rate of 4°C/min; austenitization is carried out by holding at a temperature of 1005°C for one hour under. It dissolves carbides and induces an austenitic transformation (Mebarki, 2004), resulting in an increased core hardness. The temperature is monitored using a thermocouple positioned 45 cm from the core of the die. This operation is followed by quenching and tempering to enhance mechanical properties.

Quenching involves rapid cooling through nitrogen injection under pressure (3 bar) to 80°C, lasting at least an hour and a half. After quenching, the first tempering stage occurs at 550°C for 6 hours which relieves the residual stresses from the rough quench and results in tempered martensite and the precipitation of secondary carbides. The residual austenite from the initial quench transforms into secondary martensite after the first tempering. The secondary martensite is then further tempered during the second tempering stage (Barrau, Boher, Gras, & Rezai-Aria, 2003). By adjusting the temperature, the second tempering imparts the desired hardness to the steel. The hardness evolution concerning the temperature of the second tempering is depicted in the (Figure 10) in our case, the second tempering is performed at 585°C. (Barrau, Boher, Gras, & Rezai-Aria, 2003) (Alimi, 2016).

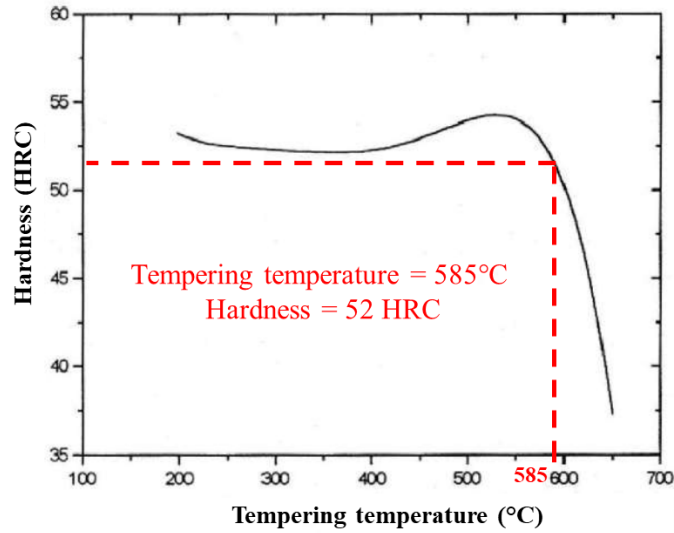


Figure 10: Hardness evolution as a function of the second tempering temperature of X38MnSiV5 steel (Barrau O., 2004).

The second tempering temperature does not influence the variety of carbides (Barrau O., 2004), as the same types of precipitates are found at the end of the first tempering (Figure 8). The second tempering is conducted at a temperature below 600°C, carbide coalescence is not observed. However, the high dislocation density introduced during quenching decreases while maintaining its "entanglement" structure (Mebarki, 2004).

After heat treatment, the dies are transferred to the electrical discharge machining station. Once the machining is complete, the geometry of the die and the surface condition are inspected, and then the dies are transferred to the nitriding treatment station.

1.2.4. Nitriding of hot forging dies

Surface treatments like nitriding are used to enhance the surface properties of metallic materials, particularly their wear resistance. During the nitriding process, the material is exposed to a nitrogen-rich atmosphere at elevated temperatures, typically between 500°C and 1100°C, depending on the steel grade and the processes used. The nitrogen concentration decreases from the treated surface towards the core, where it reaches zero. (Barrau, Boher, Gras, & Rezai-Aria, 2003)

Stellantis crankshaft forging dies are introduced into a furnace chamber enriched with ammonia and heated to a temperature of 525°C for 44 hours. The catalytic cracking of ammonia molecules on the surface of the treated piece generates atomic nitrogen, which partially diffuses into the first microns of the piece. The main parameters which control this nitriding process are: the treatment time, the temperature, the dissociation rate of the atmosphere (fraction of NH₃ are

dissociated and recombined into N_2 and H_2 molecules) and the effective nitriding depth (depth at which the hardness exceeds the core hardness). Stellantis Mulhouse site standards specify a nitride depth between 0.2 mm and 0.4mm, with a surface hardness ranging between 800 and 1100 Hv. Surface hardness is measured by a portable hardness tester. At this stage, the dies are ready for use.

The advantages of nitriding include low dimensional variations (if the treatment is uniform), good mechanical properties (hardness, friction, fatigue), and good corrosion resistance (Barrau, Boher, Gras, & Rezai-Aria, 2003).

1.3. Microstructural analysis after heat treatment and nitriding

The microstructure of the steel after heat treatments and nitriding is revealed on a sample extracted from a tool block of X38CrMoV5 steel thermally treated and nitrided at Stellantis (under the same conditions as the heat treatments and nitriding of the dies). The sample is cut and prepared using metallography techniques, including embedding in epoxy resin and mechanical polishing with increasingly fine abrasive papers up to P1200. Mirror polishing is carried out until achieving a surface finish of 3 μm , using a Nap polishing cloth. Finally, a chemical etching is performed with a 3 % nitric acid solution for precisely 15 seconds.

The nitrided material can be divided into four zones: the combination zone, the diffusion zone, the overcarburized zone and the material core (Figure 11 a). Firstly, the combination zone, also known as the white layer (Widomski *et al.*, 2021) due to its appearance after Nital etching, is located very close to the surface. It is composed of iron nitride, either ϵ (Fe_2-3N) or γ' (Fe_4N), or a mixture of the two compounds ($\epsilon+\gamma'$) (Jacq, 1994). In our study, the thickness of the combination layer is approximately 10 μm . Sometimes, this layer is removed from forging dies through a polishing process (Daffos, 2004) (Jacq, 1994). Secondly, the diffusion zone of about 100 microns which is composed of a solid solution of nitrogen with or without nitride precipitates. Nitrogen substitutes for carbon is inserted into the crystal lattice. This layer exhibits residual compressive stresses (with a maximum of 700 MPa and an average value of 250 MPa) (Daffos, 2004) (Jacq, 1994). In our case, the diffusion layer reaches a surface hardness of 1100 Hv (160 μm). Thirdly, over carburized zone of about ten microns acts as an interface between the diffusion layer and the core of the material. This zone serves as a mechanical balance because it corresponds to residual tensile stresses (approximately 100 MPa). Finally, the core of the material, which structure has not been affected by the surface treatment temperature or nitrogen diffusion (Daffos, 2004) (Jacq, 1994).

Figure 11b illustrates the tempered martensitic microstructure of X38CrMoV5 steel. The tempered martensite is composed of alpha ferrite (BCC) and cementite in the form of lamellae (Barrau, Boher, Gras, & Rezai-Aria, 2003). The microstructure also comprises nanometric-sized precipitates, a high density of dislocations, and secondary carbides (Alimi, 2016); (Medjedoub, 2004).

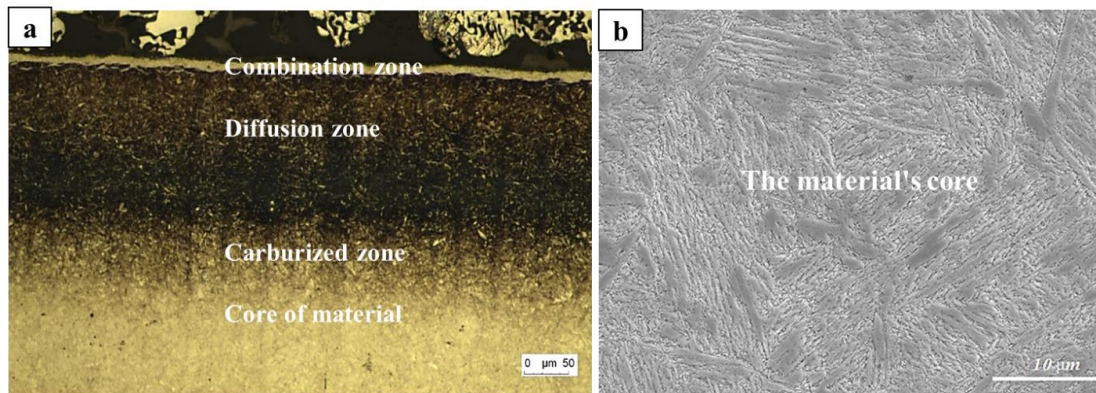


Figure 11: a) Structure of the nitrated layer, etched with Nital, b) Tempered martensitic structure in lamellae, etched with Nital.

Additionally, filamentous areas (Figure 12) commonly referred to as "angel hairs," are carbon atoms that become trapped at the former austenitic grain boundaries and associate with iron atoms to form cementite-type carbides (Fe_3C). This intergranular precipitation of carbides displaces chromium from the solid solution, thereby reducing the hardness potential of the nitrated material (Karamiş, 1993). This phenomenon is intrinsic to the nitriding process.

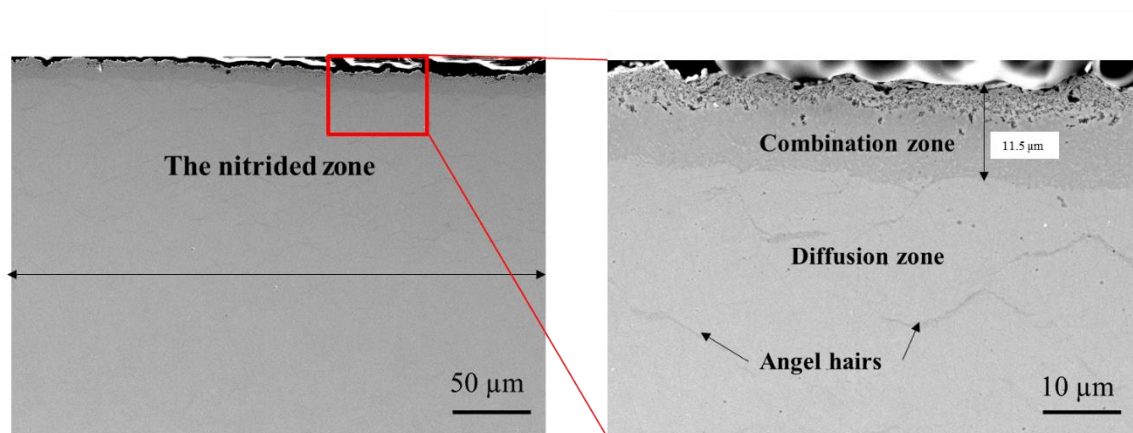


Figure 12: Angel hairs in nitrated layer.

1.4. Die failure causes.

Chandler *et al.* (Chander & Chawla, 2017) classify Hot forging die failures causes into three main categories (Figure 13): catastrophic failures, manufacturing failures, and operational failures.

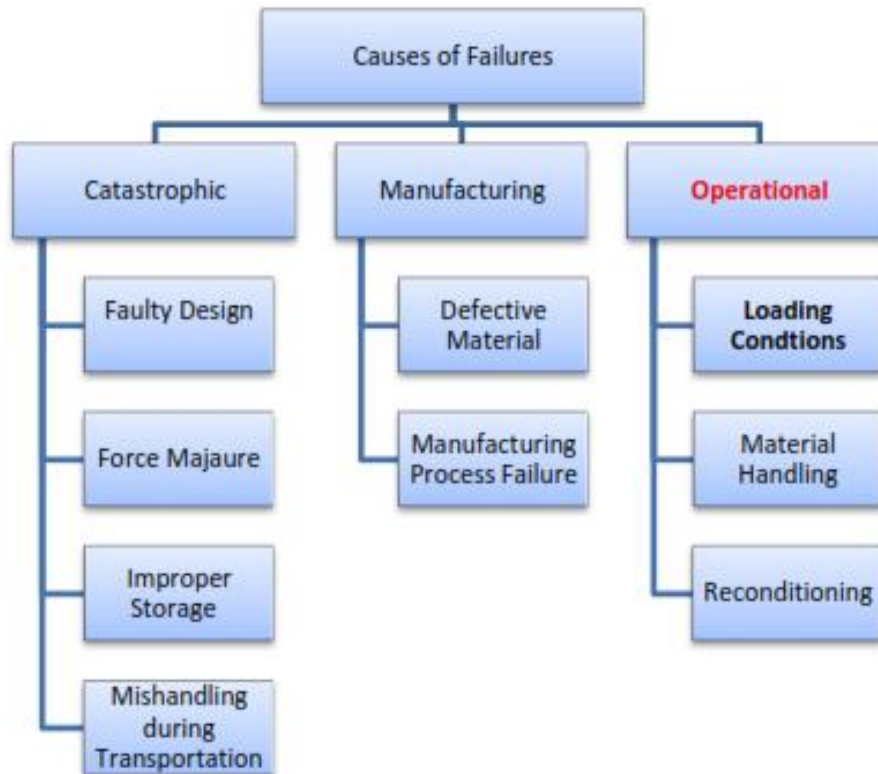


Figure 13: Die Failure causes (Chander & Chawla, 2017).

Catastrophic failures can be attributed to a range of factors such as faulty design, imperfect arrangement, inappropriate storage, and mishandling during movement. Manufacturing causes are associated with material non-conformity and the fabrication process. Inappropriate machining processes or/and inadequate heat treatment and can result in suboptimal toughness and decreased fatigue resistance. Insufficient lubrication during forming, often driven by inaccessibility or a time-saving approach, can lead to uneven stress patterns, ultimately causing die failure. (Santaella, Oliveira, & Button, 2009).

Operational causes, representing the most direct and immediate causes of die failure (Figure 14), are linked to the operating conditions during the die's use (Chander & Chawla, 2017). In the hot working process, forging dies are exposed to three primary factors that contribute to their deterioration and eventual failure: cyclic loading, thermal loads, friction and erosion. To facilitate the deformation of the material being forged, it must be heated to a temperature ranging from 1000 to 1200°C. This elevated temperature reduces the yield point of the material, enhancing its malleability and making it easier to shape. The contact with hot metal subjects the dies to temperatures between 600°C and 900°C. As the material is shaped, the dies subsequently cool down, experiencing rapid and extreme temperature changes that lead to thermal stress and fatigue. Cyclic loading, inherent to the forging process, significantly impacts the lifespan of forging dies. The repeated and fluctuating mechanical loads during forging result in fatigue, wear, and deformation of the die surfaces (Chander & Chawla, 2017).

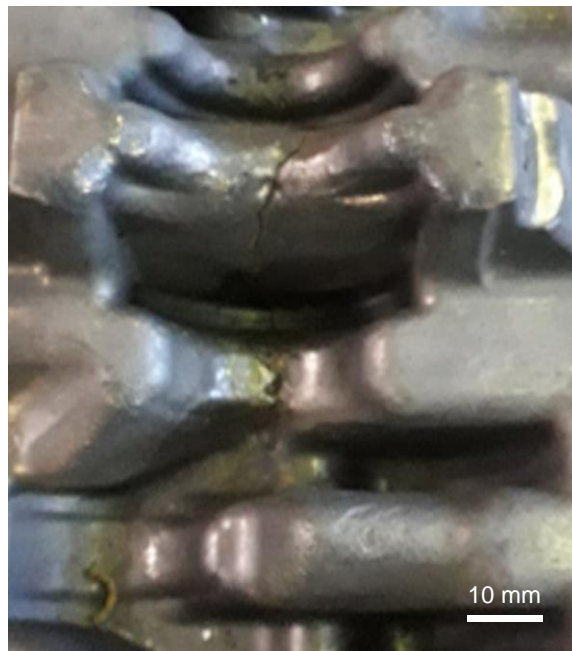


Figure 14: Example of cracks observed after crankshaft hot forging.

1.5. Damage mechanisms of hot forging tools

Historical data on forging die life provides valuable insights into the various damages that affect die durability. A comprehensive study of over 120 different cavity forms from twenty different forging operations revealed the following distribution of die damages (Figure 15). Wear is the most common cause of forging die failure, accounting for over 70% of cases. Mechanical fatigue and gross cracking are responsible for more than 25% of die failures. The rest of the damages are attributed to thermal fatigue cracking and plastic deformation (Lange *et al.*, 1992) (Grobaski, 2004).

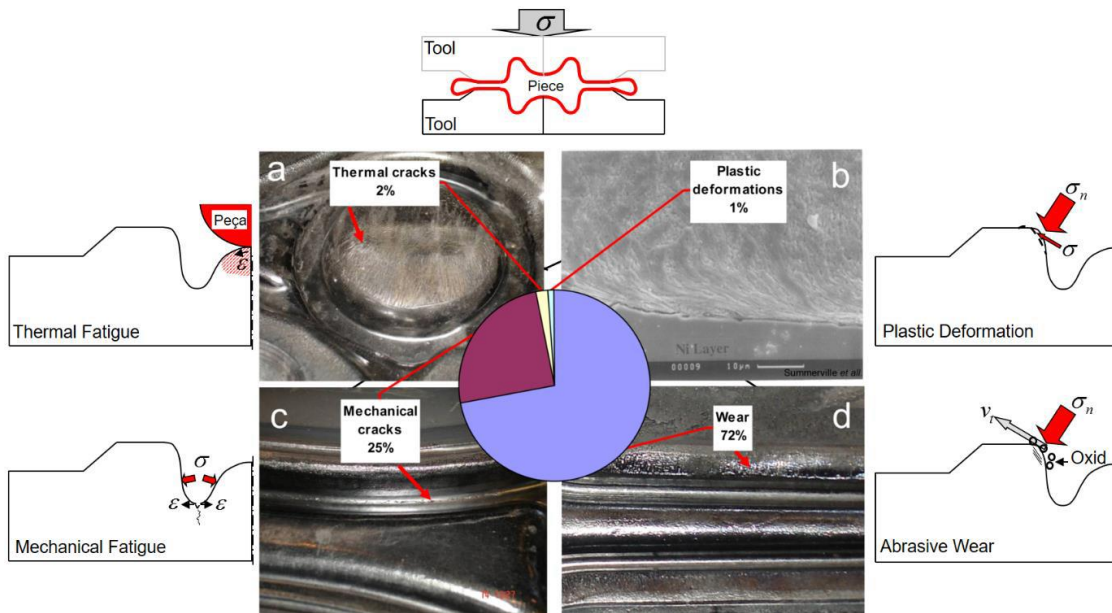


Figure 15: Die damages mechanisms shown here at various points on the lower die (Lange *et al.*, 1992) (Grobaski, 2004).

In many cases, these mechanisms act concurrently, even during the initial stages of the die operational life. Damage is typically concentrated on the die surface and subsurface layers, necessitating a localized characterization approach to understand and mitigate the damage. By extracting local properties, it is possible to estimate the extent of mechanical damage in the subsurface of the most affected areas of the die (Chander *et al.*, 2017). Based on this, some of the damaging mechanisms are described in the following paragraphs.

1.5.1. Wear Mechanisms

Wear is an inherent aspect of the hot metal flow and spreading within the impression of a forging die. Several factors influence the wear phenomenon and these are summarized in Table 4. Wear tends to be more pronounced when the design is complex, when the metal being forged possesses high hot strength, or when there is scale present on the work metal (Mazurkiewicz *et al.*, 2011)

Table 4: Factors affecting wear (Chander *et al.*, 2017).

Temperature	Atmosphere	Contact area
Load	Material properties	Finish
Velocity	Lubrication	Shape
Vibration	Sliding distance	Type of motion

Wear can be classified in three main ways. First, by how the wear appears, such as pitting, spalling, scratching, polishing, crazing, fretting, gouging, or scuffing. Second, by the physical mechanism that causes the damage, like adhesion, abrasion, oxidative, or delamination. Third, by the environmental conditions surrounding the wear (Bayer, 2004). Figure 16 shows the various types of wear encountered in forging industrial situations and their respective percentages.

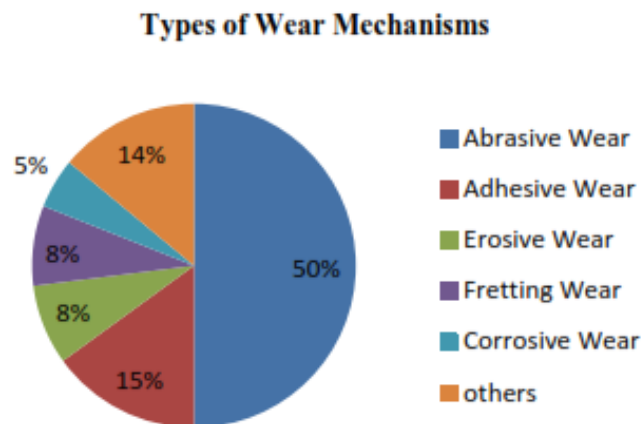


Figure 16: Hot forging dies wear mechanisms (Abachi, Akkk, & Gkler, 2010) (Kim *et al.*, 2006).

Typically, a single mechanism is the primary driver of wear, but the importance of each mechanism can change as the conditions of the tribosystem, like load, velocity, and friction change. This means that materials may exhibit different wear behaviors as these parameters change. (Doege *et al.*, 1994) (Barrau, O *et al.*, 2003) (Mazurkiewicz *et al.*, 2011) (Chander *et al.*, 2017).

- **Abrasive Wear**

Abrasive wear becomes a significant problem in tribosystems where dust and wear debris cannot be controlled or excluded (Singh, 1973). The abrasive wear mechanisms, including ploughing, cutting, and fragmentation, are influenced by the properties of both wear material (tool material) and abrasive material (Table 5). Most factors influencing abrasive wear behaviour are tied to the mechanical properties of the materials involved. If, the mechanical interaction between the abrasive material and the wear material is of great significance, chemical processes like corrosion or oxidation play a role as they affect the wear rate of materials in the specific environment (Chander *et al.*, 2017)

Abrasive wear is observed in regions where material flow across the tool surface is significant (radii, fillets, boss). This phenomenon is more pronounced in areas with high sliding velocities and substantial loading forces. Additionally, elevated temperatures promote oxidation, leading to the detachment of highly hard oxide particles from the workpiece and matrices, creating micro-machining-like fissures and grooves on the tool surface. (Alimi, 2016)

Table 5: Factors affecting abrasive wear (Singh, 1973)

Wear material properties	Abrasive material properties
Hardness-Yield Strength-Elastic modulus Microstructure-Ductility-Toughness Work-hardening characteristics- Fracture Toughness-Corrosion resistance	Particle size-Particle shape Hardness-Yield strength- Fracture properties-Concentration

One aggravating factor for abrasive wear is the loss of tool hardness due to microstructural changes in the material at high temperatures. A service temperature close to the tempering temperature (550°C) can modify the material microstructure, directly impacting its hardness. This microscopic alteration has direct consequences on the material hardness and influences its performance under high temperature working conditions.

The visual observation of hot forging dies for crankshafts at the end of their life (20,000 cycles) reveals asperities with scratches parallel to the sliding of the material, indicating the presence of abrasive wear in different areas of the die (Figure 17).



Figure 17: The presence of wear on the hot forging dies for crankshaft (20,000 cycles) at Stellantis

- **Adhesive Wear**

Adhesive wear models are based on the fact that small surface irregularities adhere together, with tips sheared from softer surfaces sticking to harder ones during sliding. In severe cases, this can lead to 'galling,' tearing microscopic material chunks. This occurs more frequently when both surfaces are of the same material or when lubrication is insufficient, especially at high temperatures or fast sliding speeds (Bayer, 2004).

During adhesion and the transfer of material, the workpiece material can undergo work hardening, making it harder than the original workpiece it came from. Additionally, oxide particles can mix into the adhered material, further increasing its hardness through particle strengthening. Regions of hard adhered material can raise the tool surface roughness. When subsequent workpieces are processed, this hard adhered material might cause indentations or scratches on the surface, leading to a worsened surface finish (Hanson, 2008) (Chander *et al.*, 2017).

1.5.2. Thermal fatigue

Thermal fatigue is observed in hot forging dies, arises from repetitive cycles of heating and cooling. Temperature variations across a material lead to stress and strain differentials caused by thermal expansion. When the resulting stress surpasses the hot tensile limit of the material, it results in the yielding of surface layers. Over numerous heating and cooling cycles, this yielding can lead to the initiation and subsequent growth of interconnected network of cracks, commonly referred to as “Heat checking” (Figure 18). During operation, the depth of these cracks may increase due to heightened local stresses, marking the onset of the failure process.

During forging, oxides form, and forging residues can fill the heat checking, generating additional stresses. Geometrically singular areas, such as angles, curvature radii, and fillets, undergo a higher concentration of thermal stresses compared to other tool areas due to heat transfer across multiple facets.

In contrast to wear and plastic deformation, where damage may lead to noticeable defects in the forged parts, fatigue-induced cracks can be less immediately visible in their impact on the formed parts. Fatigue cracks typically grow over time, and their effects on the formed parts may not be readily apparent. As a result, it may seem as if the failure occurs suddenly when these cracks reach a critical depth, causing the die to fail. (Sjöström, 2004) (Chander, et al., 2017).

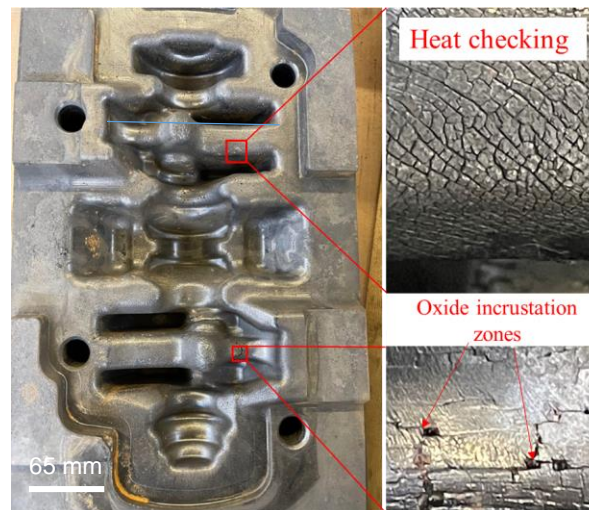


Figure 18: Thermal fatigue observed in the hot forging die for crankshafts (20,000 cycles) at Stellantis.

In such cases, the consequences can be significant. The sudden failure of a die interrupts production, requiring the replacement of damaged die components. This interruption can result in substantial economic losses and significant delays in production schedules. Managing and monitoring fatigue-induced cracks in dies are crucial not only for maintaining the efficiency of manufacturing operations but also for minimizing the economic and logistical challenges associated with unexpected die failures (Chander, et al., 2017).

1.5.3. Mechanical fatigue

The mechanical fatigue in die surfaces subjected to hot forging involves the accumulation of critical strains on the die surface, eventually leading to cracking and major failure. This process is driven by cyclic stresses and repeated external loading imposed on the die surface. Figure 19 illustrates a typical mechanical crack formation and propagation on a hot forging die, made of X30WCrV9-3 (H21) steel, subjected to different numbers of cycles. (Emamverdian, et al., 2021)

In Figure 19(a), corresponding to about 2400 forging cycles, a thin crack appears on the transversal plane with seemingly low depth. Figure 19 (b) confirms that this crack is formed on the surface/interface proximity, and its width is not constant. With an increase in the number of forging cycles, material weakening may occur, accompanied by a decrease in hardness on the surface layer due to cyclic thermomechanical loading. Consequently, grooves begin to develop and to grow in depth (see details in Figure 19 (c) and (d)).

This crack configuration was observed after about 4200 forging cycles. (Emamverdian, et al., 2021). Further increases in the number of cycles, approximately 5200 forging cycles, can lead to the formation of clusters of cracks, as depicted in Figure 19 (e).

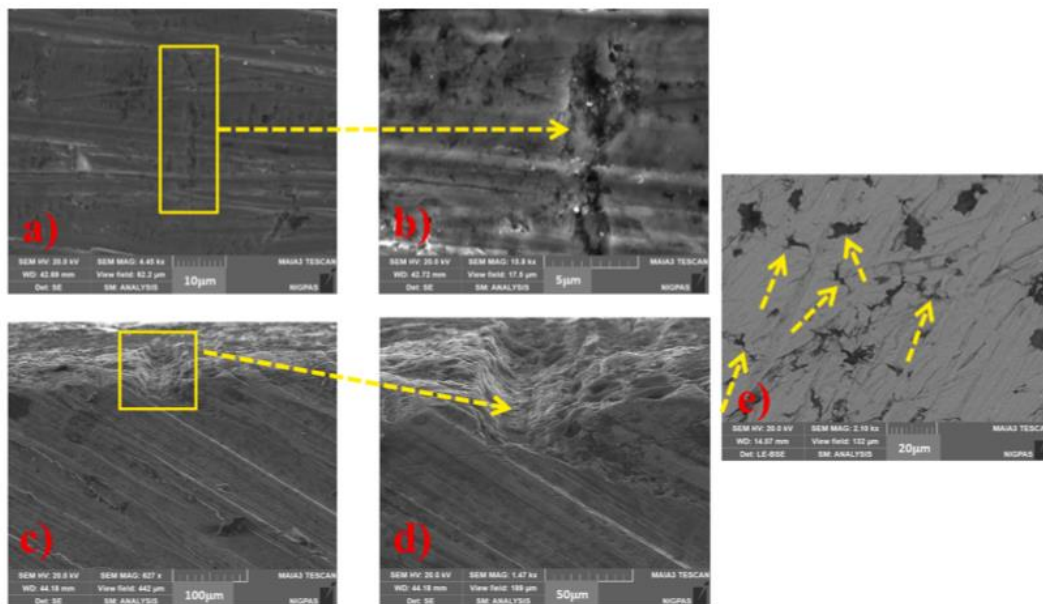


Figure 19: Mechanical crack formed on the H21 steel during hot forging process in the inner corner radius (a) after about 2400 forging cycle (b) crack 's close – up indicated in (a), (c) after about 4200 forging cycles, (d) crack 's close –up indicated in (c) and (e) dispersion of cracks after about 5 200 forging cycles on the surface of the die. (Emamverdian, et al., 2021).

In regions of thermomechanical stress concentrations, such as at curvature radii and junction fillets, mechanical fatigue, often accompanied by thermal fatigue, is observed (Figure 20). Fissure initiation typically occurs in the form of progressive crack propagation.

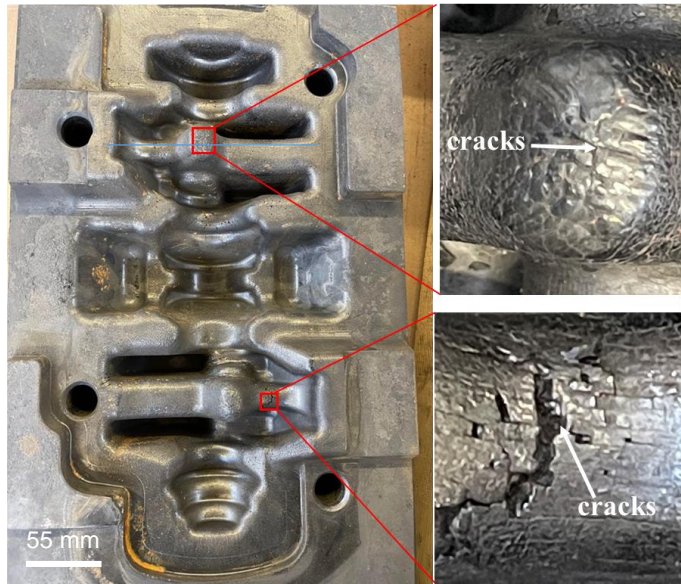


Figure 20: Mechanical fatigue observed in the hot forging die for crankshafts (20,000 cycles) at Stellantis

1.6. Oxidation of steels during hot working

During the heating process and/or during forming, oxides are produced on the surface of the billet and tools. Wustite (FeO), magnetite (Fe_3O_4) and hematite (Fe_2O_3) are the three primary iron oxides known to form during the hot working of structural carbon steels. Notably, wustite, exhibits lubricating properties when exposed to high temperatures. Magnetite shares similar lubricating characteristics in high-temperature conditions. Conversely, hematite, serves as an abrasive agent contributing to wear during the hot forming process (Zambrano *et al.*, 2015).

Different factors have an impact on the formation, structure, and chemical composition of oxide scales. The heating temperature (Figure 21), duration, and cooling rate are among the important factors affecting the formation of oxide scales (Behrens *et al.*, 2018) (Zambrano *et al.*, 2015). The typical three-layered oxide scale system is shown in (Figure 22), especially between 700 and 1000 °C (Zambrano *et al.*, 2015) (Graf *et al.*, 2013) (Serebriakov, 2020).

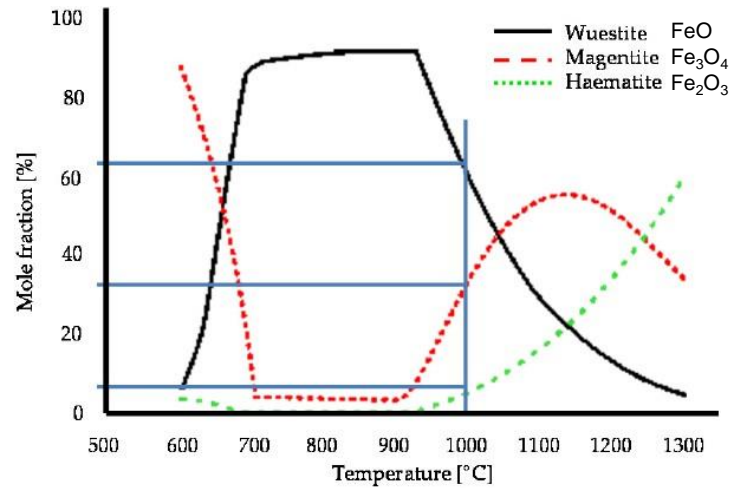


Figure 21: The impact of heating temperature on oxide scale composition (Behrens *et al.*, 2018).

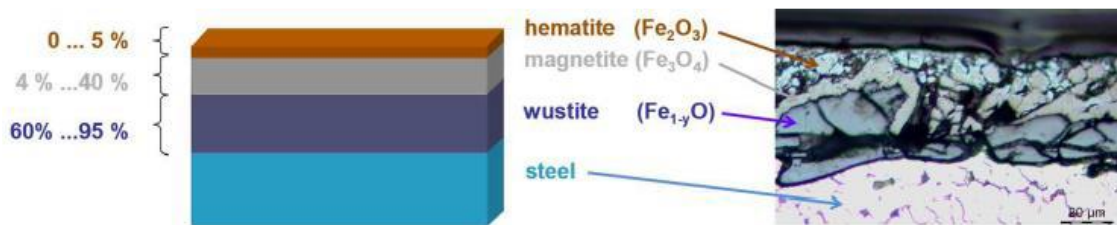


Figure 22: Classical three-layer oxide scale system (Graf, *et al.*, 2013). (Serebriakov, 2020)

The X38MnSiV5 grade undergoes oxidation in its virgin state and in its nitrided state. With virgin steel, at temperature above 570°C, an outer layer of hematite (Fe₂O₃) and an inner layer of magnetite (Fe₃O₄) can be distinguished (Figure 23). A third layer indicates an internal oxidation containing chromium as well (Fe,Cr)₃O₄ and magnetite. The chromium enrichment occurs at the oxide/steel interface. The increase in chromium content appears to impart a protective nature to these layers against high-temperature oxidation (Bruckel, 2003).

Fe_2O_3
Fe_3O_4
$(Fe, Cr)_3O_4 + Fe_3O_4$
Base metal

Figure 23: The decomposition of the oxide layer into strata based on their composition on X38CrMoV5 (Barrau O., 2004)

Wustite (FeO) does not form on this steel, even beyond 570°C. The chromium content exceeding 2% in iron alloys prevents the formation of a wustite layer (Gemelli, *et al.*, 1996) (Armanet, 1984) (Barrau O., 2004). In fact, the introduction of chromium shifts the wustite formation temperature to higher values (around 850°C for steels containing 5% chromium (Schutze, 1997)).

The nature of the oxide layers formed between 600°C and 700°C remains the same; however, the growth kinetics of these layers can vary by a factor of four (Table 6). The thickness of the layers observed at 700°C is less uniform but thicker compared to those formed at 600°C. In general, X38CrMoV5 forms adherent oxides under static conditions (Jean, 1999) (Barrau O., 2004).

Table 6: Oxide layer thickness variation vs temperature in the presence of water vapor on the virgin material (Bruckel, 2003).

Oxidation temperature	Holding time	Total thickness of the oxide layer
600°C	90 Hours	35 μm
700°C		160 μm

Notably, the oxide layers formed on nitrided, and virgin materials exhibit differences in morphology, with nitrided materials having an acicular structure and virgin materials showing a cellular structure (Barrau O., 2004). Less oxides containing chromium are formed on the nitrided material (Daffos, 2004). Chromium is partially trapped by the formed nitrides, limiting its mobility under thermal agitation.

The introduction of nitrogen creates a diffusion barrier that impedes the mobility of iron atoms, resulting in the formation of thinner oxide layers on nitrided steel in comparison to those on virgin steel. Moreover, the presence of a combination layer reinforces this diffusion barrier, leading to a deceleration of the oxidation kinetics (Barrau O., 2004).

1.7. Conclusion

In this chapter, after describing the main stages in the crankshaft forming process, we reviewed the literature on the different phenomena of thermomechanical damage to tools during hot forging, the behavior of the materials involved, and the third bodies (oxides, lubrication) present at the interface between the billet and the tool.

The analysis of the forging process has highlighted the complexity of tool geometries and the challenges encountered during crankshaft forging. Identification of failures and defects observed in tools at different stages of their lifecycle revealed predominant degradation modes such as wear, thermal fatigue, and mechanical fatigue. Worn tools also exhibit surface oxides embedded within cracks. The origin of these oxides could be solely from the billet if the contact temperature is below 570°C, or, both the billet and the tool simultaneously if the tool temperature exceeds 570°C.

The changes undergone by the tools emphasize the importance of considering several aspects in our study, related to tool surface condition, geometric variations, oxidation, and the influence of contact conditions on tool mechanical properties and microstructure. Microstructural analysis of new tools confirms the presence of a tempered martensitic structure with a surface nitrided layer exhibiting a hardness of 1100 Hv.

The results of previous investigations of fatigue tests, heat treatments, and oxidation studies have enabled the contextualization and guidance of our choices regarding tool characterization. Fatigue phenomena is present on the crankshaft forging tools. Our approach involves tracking damage phenomena (fatigue and wear) throughout the lifecycle of the die. Finally, the study of billet/tool contact requires consideration of aspects related to friction and lubrication. In order to numerically model the crankshaft forming process, the first step is to correctly identify the rheology of the billet to obtain a correct numerical evaluation of the mechanical (contact pressure), kinematic (sliding speed) and thermal (interface temperature) data. The rheological behaviour of 38MnSiV5 is described in the next chapter.

**Chapter 2. Rheological behavior
determination of 38MnSiV5 steel
grade at high temperature**

Stellantis currently uses the rheological laws for 38MnSiV5 taken from the FORGE NxT finite element software database to numerically simulate the hot forging of crankshafts. Therefore, the relevance of these data is unknown and it is necessary to determine stress-strain curves adapted to the current conditions. The aim of this chapter is to accurately determine the rheology behavior of the 38MnSiV5 grade at the temperatures and strain rates encountered in the industrial environment. The hot compression test is the most appropriate test for establishing the flow laws of materials in the case of hot forging. The Gleeble 3500, a fully integrated closed-loop numerically controlled thermal and mechanical testing system developed by Dynamic Systems Inc., is used for these characterization tests.

The test parameters cover a range of temperatures from 950 °C to 1250 °C and strain rates from 10^{-2} s^{-1} to 10 s^{-1} to replicate the actual operating conditions encountered by the material. To obtain reliable behavior laws that are as close as possible to the behavior of 38MnSiV5 on an industrial site, it is necessary to ensure that the distribution and grain size of the austenite present in the samples at high temperatures just before the compression tests match those of the industrial billets. This requires the determination of a specific preliminary thermal cycle. In our case, this thermal cycle is also used as a thermal etch, enabling us to measure the initial distribution and grain size of the sample.

After the compression tests, the raw flow stress curves must be corrected to remove friction phenomena between the sample and the dies during compression, as well as to consider the adiabatic heating of the sample and potential variations in strain rates. The methodology for carrying out these corrections is described in this chapter.

2.1 Preliminary thermal cycle to replicate the required grain size

Before the compression test, the samples must be heated using a thermal cycle. This aims to closely match the grain size and distribution observed in the industrial hot-forging billets with the samples manufactured and tested on the Gleeble machine. This thermal cycle also homogenizes the temperature of the sample and its metallurgical structure, facilitating, among other things, the dissolution of carbides (Da Silva *et al.*, 2016).

a- Billet microstructure

Firstly, the approach involves measuring the prior austenitic grain size on the industrial hot forging billet. Then, preliminary tests and measurement operations are carried out to determine the optimal thermal cycle, in terms of homogenization temperature, holding time, and heating rate.

Chapter 2. Rheological behavior determination of 38MnSiV5 steel grade at high temperature

Thus, a cylindrical billet, with dimensions of 316 mm in height and 85 mm in diameter, made of 38MnSiV5 steel, from the production of crankshafts at the Forge unit (Figure 24a), is heated in an induction heater at Stellantis. The heating temperature ranges between 1270 °C and 1290°C, with a holding time of 319 seconds. These heating parameters faithfully represent the heating conditions of the billet used in the crankshaft forging process.

The heated billet is then quenched in water. After this step, a piece is extracted from the billet (Figure 24b) and subdivided into 8 distinct samples (Figure 24c).

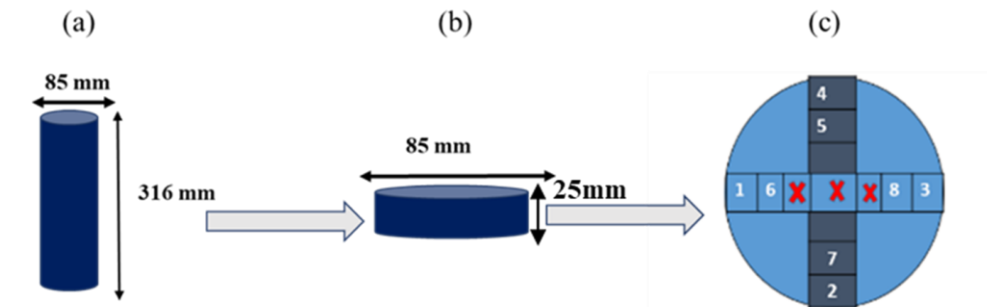


Figure 24: Sample preparation for determining the prior austenitic grain size in the billet: a) initial geometry of the billet, b) dimensions of the piece extracted from the billet, c) location of 8 samples to measure the grain size.

The deliberate exclusion of the middle section is undertaken to minimize potential distortions resulting from specific thermal gradients and eventually, chemical gradients (segregation), which are more pronounced in the central region. Each sample is cut and prepared using metallography techniques, including embedding resin epoxy. The samples then undergo polishing until a surface finish of 3 micrometres, is achieved using Nap polishing cloth. A chemical etching of the 8 samples is performed using the BECHET BEAUJARD reagent for 3 minutes and 30 seconds to expose the prior austenitic grain boundaries. Figure 25 shows the microstructure of sample 1.

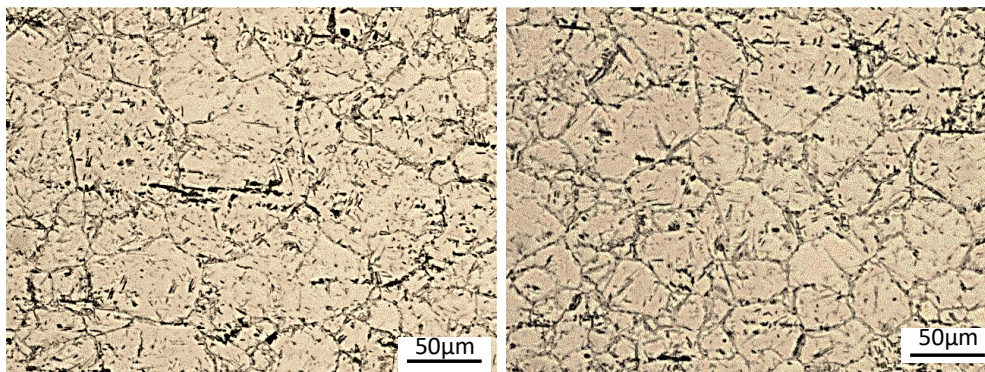


Figure 25: Micrographs of sample 1 (Figure 24c) obtained from the billet heated at 1290°C and quenched in water.

Figure 26 shows the mean grain size distribution observed in the 8 samples (Figure 24c). Approximately 250 grains are measured from each sample using ImageJ Software. A bimodal distribution is evident. Analysis of the measurements shows that over 70 % of the grains are smaller than 50 μm . The average grain size is $39 \pm 7 \mu\text{m}$.

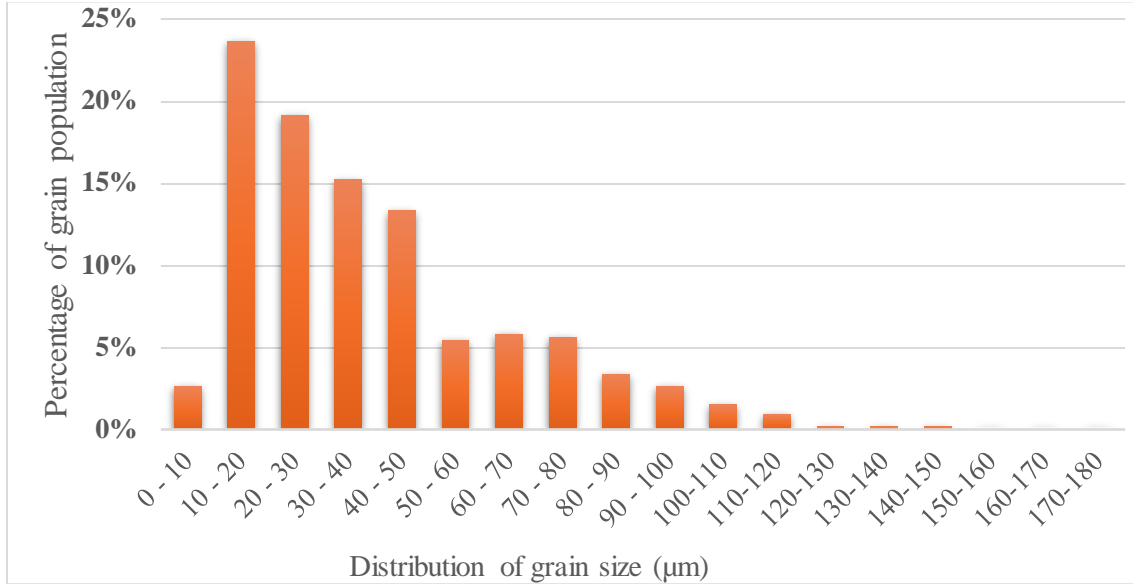


Figure 26: Grain size distribution in the billet.

b- The reproduction of the billet microstructure using Gleeble

In order to replicate the observed grain size distribution in the industrial samples, a series of thermal etching experiments are being conducted on our samples using the compression test machine. Each thermal etching is defined by the holding time, the heating rate and the homogenization temperature. The cooling rate is set at $1 \text{ }^\circ\text{C/s}$ up to $500 \text{ }^\circ\text{C}$ for all cases.

Table 7 presents the design of experiments used to obtain various grain sizes and the mean grain sizes obtained after etching. The choice of the temperature at $1250 \text{ }^\circ\text{C}$ corresponds to both the practical constraints of the compression machine related to the temperature control using a K-type thermocouple and closely approximates the industrial billet heating range ($1270 \text{ }^\circ\text{C}$ to $1290 \text{ }^\circ\text{C}$). The choice of a temperature of $1220 \text{ }^\circ\text{C}$ was made after thermal etching at $1250 \text{ }^\circ\text{C}$, in an attempt to get as close as possible to the size and distribution of grains found on the industrial site.

Table 7: Experimental design of thermal etchings at 1250°C and 1220°C with the corresponding holding times and heating rates. Mean austenitic grain size obtained after etching.

Homogenization temperature (°C)	Holding time (s)	Heating rate (°C/s)	Mean austenitic grain size (µm)
1250	180	3°C/s	62±7
	90		56 ± 5
	60	5°C/s	56±5
	30	3°C/s	49±6
1220	90		46±4

Comparing the average grain size for each thermal test with the billet result ($39 \pm 7 \mu\text{m}$) reveals that the sample tested at 1250 °C with a holding time of 30 seconds and a heating rate of 3 °C/s (with a grain size of $49 \pm 6 \mu\text{m}$), and the sample tested at 1220 °C, holding time of 90 seconds, and heating rate of 3 °C/s (grain size of $46 \pm 4 \mu\text{m}$) come closest to the industrial sample grain size. Figure 27 compares grain size distribution in the billet with the results of these two thermal etchings. The grain size distribution appears near except, mainly, for grain sizes between 10 and 30 µm. Finally, a preliminary thermal cycle at 1220 °C with a holding time of 90 seconds and a heating rate of 3 °C/s is selected. The choice is justified by the average grain size being closer to the grain size of the industrial billet.

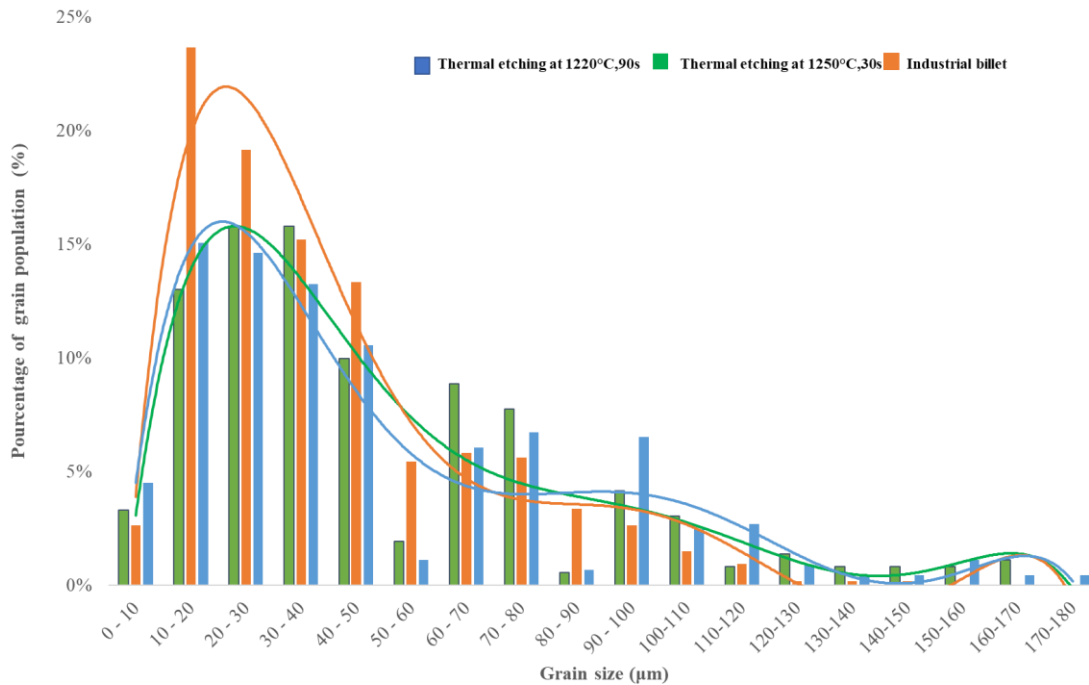


Figure 27: Comparison between the grain size distribution of the industrial billet and the grain size distributions of samples obtained after thermal etching at 1220°C and 1250°C.

2.2 Mechanical behavior of 38MnSiV5 steel grade at high temperatures

2.2.1. Compression tests procedure

Compression tests are carried out on cylindrical samples of 38MnSiV5 steel. The tests covered a temperature range T between 950 °C and 1250 °C with an increment of 100 °C for 4 strain rates $\dot{\epsilon}$ (0.01 s^{-1} , 0.1 s^{-1} , 1 s^{-1} , 10 s^{-1}). A total of 16 test conditions are studied. In order to ensure reliability, each test is repeated twice, i.e., 32 tests. The dimensions of the specimens are 12 mm in length and 8 mm in diameter. These test samples are machined from billets used in crankshaft production.

Figure 28 shows the thermomechanical treatments applied for the compression tests at different temperatures. All tests present a first thermal cycle in common, corresponding to that selected in section 2.2. Next, the temperature of the sample is increased or decreased at 3 °C/s

Chapter 2. Rheological behavior determination of 38MnSiV5 steel grade at high temperature

according to the test's temperature and maintained at this temperature for 90 s before the compression test is performed.

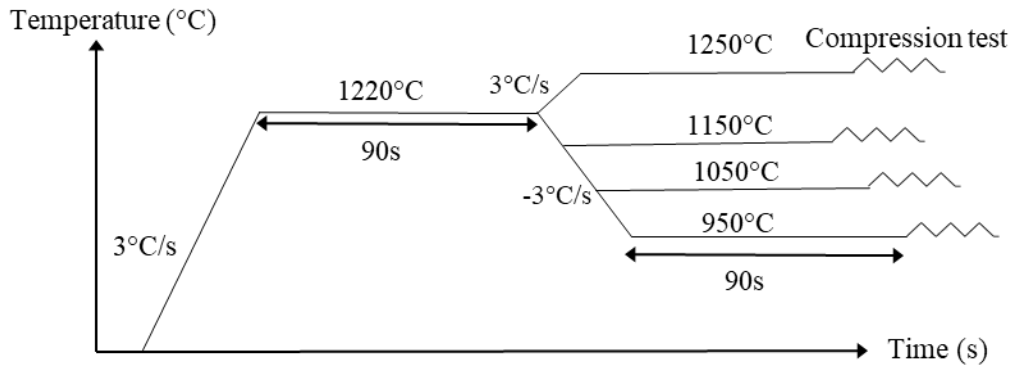


Figure 28: Diagram of the thermomechanical treatments of the compression tests.

Axisymmetric compression tests using Gleeble 3500 (Figure 29 a) are conducted in a vacuum with a pressure lower than 10^{-5} Torr in the test chamber (Figure 29 b). Each compression tool consists of a tungsten carbide die (WC die) covered by a tantalum foil which serves as a diffusion barrier to prevent sticking between surfaces at high temperatures. At the same time, the surfaces that are in contact with the specimen are lubricated with a high-temperature stable nickel-based grease in order to reduce friction between the contacting surfaces. Before each test, WC dies undergo grinding using a 220 mesh SiC abrasive paper to remove any debris that may remain on their surfaces due to the previous test and to ensure a clean and flat surface.

The compression samples are heated through conduction phenomena between the WC tools by the Joule effect. The heating rate during testing is maintained at 3 °C/s. Temperature control is achieved by placing a welded type K thermocouple (comprising chrome and alumel) on the test sample surface at the middle height (Figure 29 b). This control ensures precise temperature monitoring during the compression test.

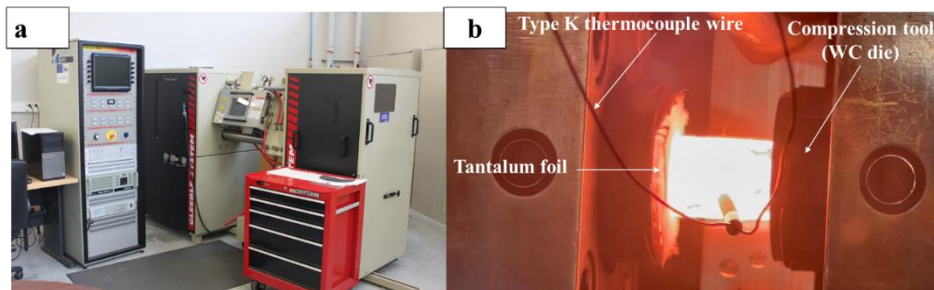


Figure 29: Gleeble 3500 machine: a) General view, b) Test chamber during the compression test; localization and description of the elements of the test.

2.2.2. Compression test results

Figure 30 shows, for the 2 repetitions, the raw curves of effective stress versus effective strain determined from the results of compression tests carried out at four temperatures T (950 °C, 1050 °C, 1150 °C and 1250 °C), for the 4 strain rates $\dot{\epsilon}$ (0.01 s^{-1} , 0.1 s^{-1} , 1 s^{-1} and 10 s^{-1}).

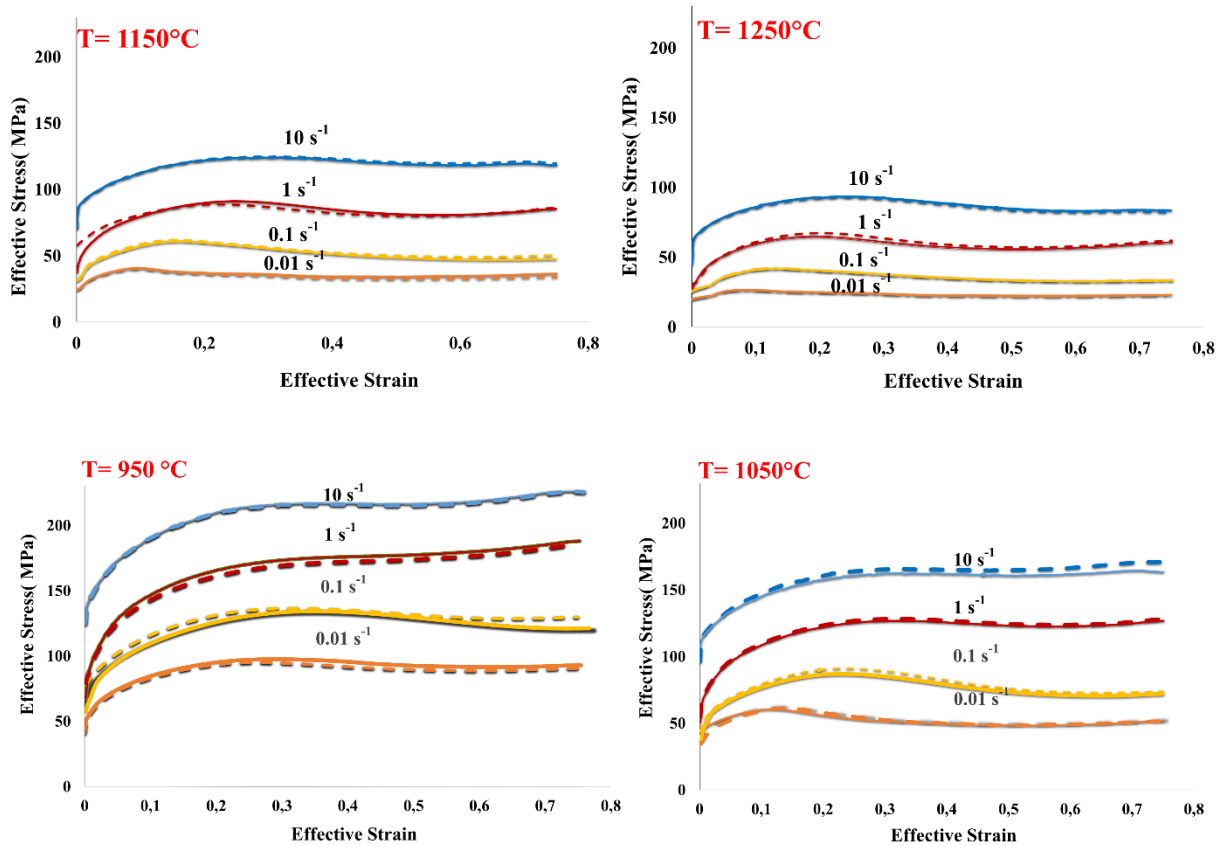


Figure 30: Stress-strain raw curves at different temperatures and strain rates.

As the temperature decreases, the effective stress level increases. At a constant temperature, as the strain rate increases the effective stress level rises, achieving a peak stress. This initial phase of the curve is mainly governed by work hardening (WH) and dynamic recovery phenomena (DRV). Afterward, the stress-strain evolutions stabilize or decrease due to the material softening induced by dynamic recrystallization (DRX). Finally, for specific strain rates and temperature (e.g., curves at 950 °C for 1 and 10 s^{-1}) (Figure 30), the material returns to a positive stress-strain evolution, resulting from the increased frictional forces. (Serebriakov, 2020) (Chalon, 2016), (Puchi-Cabrera *et al.* 2014, 2015).

Processing of the stress-strain curves is necessary to consider the contact conditions between the sample and the dies, as well as the inherent fluctuations in temperature and strain rate during the hot compression test.

2.2.3. Correction of stress-strain curves

The correction procedure involves two distinct stages. Initially, corrections were applied to consider the friction effects that occur when steel undergoes deformation under axisymmetric compression. This correction aimed to reduce the impact of friction on the obtained results, ensuring a more accurate representation of the material behavior. A second correction is applied to consider the effects of temperature and strain rate during the compression test. This step aims to refine the results by taking into account the influence of these variables on the material response, enhancing the precision and reliability of the obtained data.

- **Friction correction of stress-strain curves**

The methodology applied to perform the friction correction of the curves involves using the equation developed from the equilibrium of forces during the homogeneous compression of a flat disc (Christiansen *et al.*, 2016). Such a correction is commonly carried out by assuming a constant friction coefficient (μ) independent of deformation conditions, which is an unrealistic approach. Also, it is founded on the analysis of the flow stress curves determined with both lubricated and unlubricated samples of different initial diameter-to-height ratios, deformed under similar deformation conditions. In this section, a novel procedure proposed by Puchi-Cabrera *et al.* (2019) for the systematic correction of the flow stress curves, considering the changes in friction conditions during plastic deformation, has been used.

The equation (1) defines the average pressure on the tools (or uncorrected flow stress), \bar{P} , as a function of the friction-corrected flow stress (σ), the friction coefficient (μ), and the instantaneous values of the height (h) and diameter (d) of the sample during the compression test:

$$\bar{P} = 2\sigma \left[\frac{h}{\mu d} \right]^2 \left[\exp\left(\frac{\mu d}{h}\right) - \frac{\mu d}{h} - 1 \right] \quad (1)$$

It is assumed that there is no barrel effect at the edges of the sample and that the height of the sample is sufficiently small for the axial compressive stress to remain constant. The ratio d/h can be expressed as equation (2):

$$\frac{d}{h} = \frac{d_0}{h_0} \left(\frac{1}{\exp(-\varepsilon)} \right)^{3/2} \quad (2)$$

With d_0 and h_0 , the initial values of diameter and height of the sample and ε , the effective strain applied to the material, by considering that the sample undergoes deformation under compression conditions.

To determine the correction due to friction, there are two possible approaches: conducting compression tests with samples of various diameter/length ratios to determine the friction coefficients or adopting friction coefficients from a similar material. A comparable approach to that employed by Puchi-Cabrera *et al.* (2021) is used in this work from a similar material, 20MnCr5 steel. These data are extracted from a previous study conducted at LAMIH by Puchi-Cabrera *et al.* (2019), providing friction values for various temperatures ranging from 850 to 1200 °C, which correspond to the austenitic range of this steel (Table 8). This choice is justified by the fact that, in our case, the alloying elements will also be diluted in the austenitic iron matrix. Moreover, tests on 20MnCr5 are conducted on the same compression machine used for the 38MnSiV5 compression test, which means employing the same WC dies, tantalum foils, and nickel-based grease.

Table 8: Friction coefficient values (μ) as a function of deformation temperature and strain for 20MnCr5 steel grade (Puchi-Cabrera *et al.*, 2019).

Strain	Temperature, °C				
	850	900	1000	1100	1200
0	0.000	0.000	0.000	0.000	0.000
0.05	0.000	0.000	0.130	0.163	0.321
0.1	0.155	0.077	0.160	0.163	0.351
0.15	0.202	0.143	0.190	0.161	0.379
0.2	0.194	0.171	0.200	0.162	0.409
0.25	0.173	0.188	0.217	0.184	0.376
0.3	0.161	0.209	0.242	0.210	0.372
0.35	0.157	0.219	0.260	0.237	0.372
0.4	0.160	0.231	0.285	0.264	0.359
0.45	0.164	0.236	0.305	0.281	0.355
0.5	0.169	0.240	0.318	0.287	0.356
0.55	0.173	0.241	0.324	0.291	0.346
0.6	0.166	0.237	0.327	0.294	0.333
0.65	0.163	0.232	0.320	0.293	0.321
0.7	0.158	0.224	0.309	0.286	0.307
0.75	0.153	0.217	0.297	0.276	0.289
0.8	0.148	0.206	0.287	0.265	0.269
0.85	0.142	0.195	0.276	0.251	0.248
0.9	0.136	0.184	0.261	0.238	0.231
0.95	0.129	0.171	0.249	0.223	0.211
1.0	0.126	0.160	0.237	0.211	0.191

Chapter 2. Rheological behavior determination of 38MnSiV5 steel grade at high temperature

An interpolation-extrapolation calculation is performed in Matlab using the scatteredInterpolant function to obtain the friction coefficient values from the data reported in the previous study (Table 9)

Table 9: Friction coefficient (μ) values obtained after interpolation and extrapolation computations using MATLAB.

Strain	Temperatures (°C)			
	950	1050	1150	1250
0	0	0	0	0
0.05	0.0650	0.146	0.242	0.400
0.1	0.118	0.161	0.257	0.445
0.15	0.166	0.175	0.27	0.488
0.2	0.185	0.181	0.285	0.532
0.25	0.202	0.200	0.28	0.472
0.3	0.225	0.226	0.291	0.453
0.35	0.239	0.248	0.304	0.439
0.4	0.260	0.274	0.311	0.406
0.45	0.270	0.293	0.318	0.392
0.5	0.280	0.302	0.321	0.390
0.55	0.282	0.307	0.318	0.373
0.6	0.282	0.310	0.313	0.352
0.65	0.276	0.306	0.307	0.335
0.7	0.266	0.297	0.296	0.317
0.75	0.257	0.286	0.282	0.295
0.8	0.246	0.276	0.267	0.271
0.85	0.235	0.263	0.249	0.246
0.9	0.222	0.249	0.234	0.2275
0.95	0.210	0.236	0.217	0.205
1	0.198	0.224	0.201	0.181

Using the friction coefficient values (Table 9), friction-corrected flow stress σ as a function of strain can be determined for each test condition from Equations 1 and 2 since the evolutions of the average pressure (\bar{P}) and the ratio of d/h are known. Figure 31 shows an example of the results obtained after friction correction. The showed test is the first test carried out at a temperature of 950 °C and at 0.01 s⁻¹. The effective stresses decrease after correction for friction, with a maximum reduction of 6%.

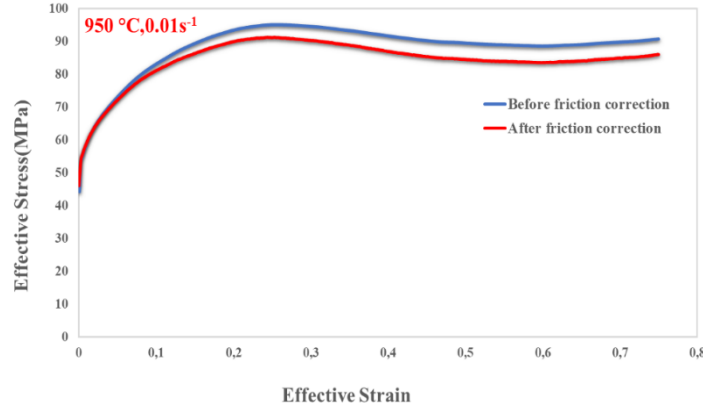


Figure 31: Stress-strain curves for the condition 950 °C-0.01 s⁻¹ before and after friction correction.

- **Temperature and strain rate correction**

The temperature and strain rate correction method is based on the model proposed by (Sah *et al.*, 1974). It involves the identification of the effective saturation stress due to work-hardening (WH) and dynamic recovery (DRV) : σ_s (Figure 32). The approach used is based on previous works conducted at LAMIH by (Chalon, 2016) (Puchi-Cabrera *et al.*, 2014, 2015).

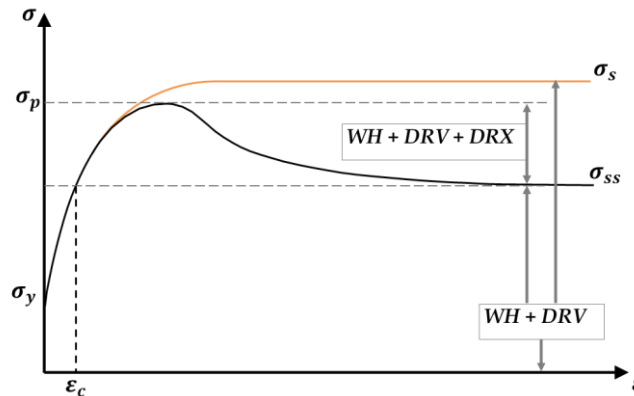


Figure 32: Characteristic stress-strain curves of a material subjected to work hardening (WH), dynamic recrystallization (DRV), and dynamic recovery (DRX) (Chalon, 2016).

When the material exhibits only work-hardening and dynamic recovery the data (stress-strain) can be fitted to the equation of the form (Sah *et al.*):

$$\sigma = \sigma_y + (\sigma_s - \sigma_y) \left[1 - \exp\left(-\frac{\varepsilon}{\varepsilon_r}\right) \right]^{\frac{1}{2}} \quad (3)$$

with σ_y , the yield stress. ε_r , the relaxation strain, depends on the initial work-hardening rate θ_0 through the relationship (Puchi-Cabrera *et al.*, 2014)

$$\varepsilon_r = \frac{(\sigma_s - \sigma_y)}{2\theta_0} \quad (4)$$

The parameters σ_y , σ_s and θ_0 are determined through least square nonlinear regression, considering that they are a positive value and $\sigma_y < \sigma_s$ using data from curves corrected for friction in the range of strain from 0 to the critical strain, ε_c for the onset of DRX given by the following expression:

$$\varepsilon_c = -\varepsilon_r \cdot \ln \left[1 - \left(\frac{\sigma_{ss} - \sigma_y}{\sigma_s - \sigma_y} \right)^2 \right] \quad (5)$$

Once the saturation stress σ_s is determined for each condition studied, it remains to establish the relationship between σ_s and the experimental conditions: temperature T and strain rate $\dot{\varepsilon}$.

σ_s is expressed as a function of temperature and strain rate according to (Sellars & McTegart, 1966), given by equation (6):

$$\sigma_s(T, \dot{\varepsilon}) = \delta_s \cdot \sinh^{-1} \left[\left(\frac{Z}{B_s} \right)^{1/m_s} \right] \quad (6)$$

The parameters δ_s , B_s and m_s , are specific to the material.

The model includes the temperature T and strain rate $\dot{\varepsilon}$ dependence of saturation stress σ_s through the Zener-Hollomon parameter Z (equation 7).

$$Z = \dot{\varepsilon} \cdot \exp\left(\frac{Q}{R \cdot T}\right) \quad (7)$$

with Q, the value of the apparent activation energy for hot deformation, R is the gas constant. The parameters δ_s , B_s , m_s and Q are determined through least square nonlinear regression using the previously computed saturation stresses (equations 6 and 7).

After identification of these parameters, the equations 8 and 9 are obtained:

$$Z = \dot{\varepsilon} \exp\left(\frac{369210 \text{ J} \cdot \text{mol}^{-1}}{R \cdot T}\right) \quad (8)$$

$$\sigma_s = 68.2 \sinh^{-1} \left[\left(\frac{Z}{2 \cdot 10^{12}} \right)^{1/4} \right] \quad (9)$$

Figure 33 presents the evolution of the saturation stress σ_s as a function of the Zener-Hollomon parameter (Z). The slight deviation shown in Figure 33 between the experimental data (points in blue) and the fitted equation (9) (red curve) signifies a robust correlation between effective saturation stress σ_s and the Zener-Hollomon parameter, Z .

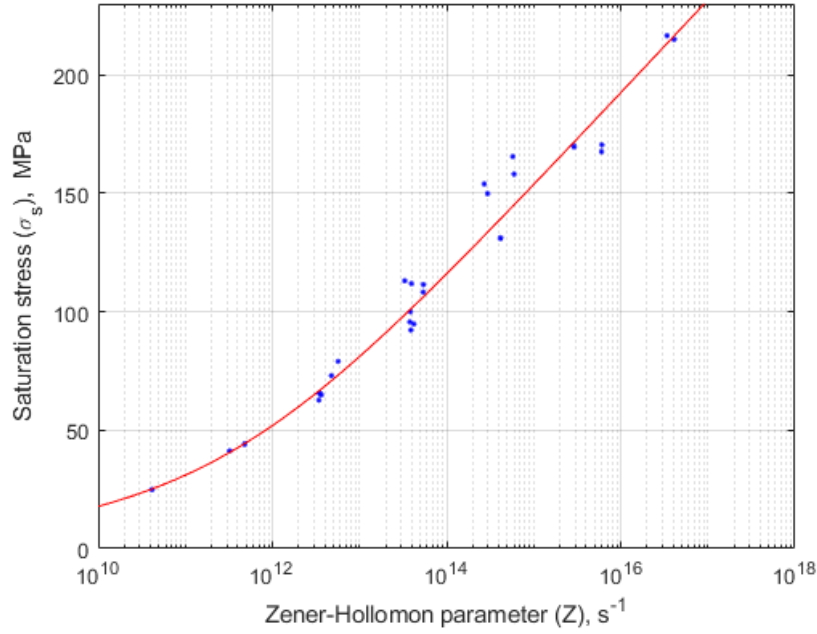


Figure 33: Evolution of the saturation stress as a function of the Zener-Hollomon parameter.

From equations (8) and (9), the strain rate and temperature corrections can then be estimated using:

$$\frac{d\sigma}{d\dot{\epsilon}} = \frac{d\sigma}{d\sigma_s} \cdot \frac{d\sigma_s}{d\dot{\epsilon}} = \frac{d\sigma_s}{d\dot{\epsilon}} \cdot \left[1 - \exp\left(-\frac{\epsilon}{\epsilon_r}\right) \right]^{1/2} \quad (10)$$

$$\sigma_{\text{corrected}} = \sigma_{\text{uncorrected}} + \frac{d\sigma_s}{d\dot{\epsilon}} \cdot (\bar{\epsilon} - \dot{\epsilon}) \quad (11)$$

$$\frac{d\sigma}{dT} = \frac{d\sigma}{d\sigma_s} \cdot \frac{d\sigma_s}{dT} = \frac{d\sigma_s}{dT} \cdot \left[1 - \exp\left(-\frac{\epsilon}{\epsilon_r}\right) \right]^{1/2} \quad (12)$$

$$\sigma_{\text{corrected}} = \sigma_{\text{uncorrected}} - \frac{d\sigma_s}{dT} \cdot (T - \bar{T}) \quad (13)$$

These equations are used to correct our stress-strain curves already corrected for friction. The positive sign in equation (11) signifies that an elevation in strain rate corresponds to an increase in flow stress. Conversely, the negative term in equation (13) shows that an increase in deformation temperature corresponds to a decrease in flow stress.

Figure 34 presents stress-strain curves after all corrections. Tables of data after correction are presented in Appendix 1.

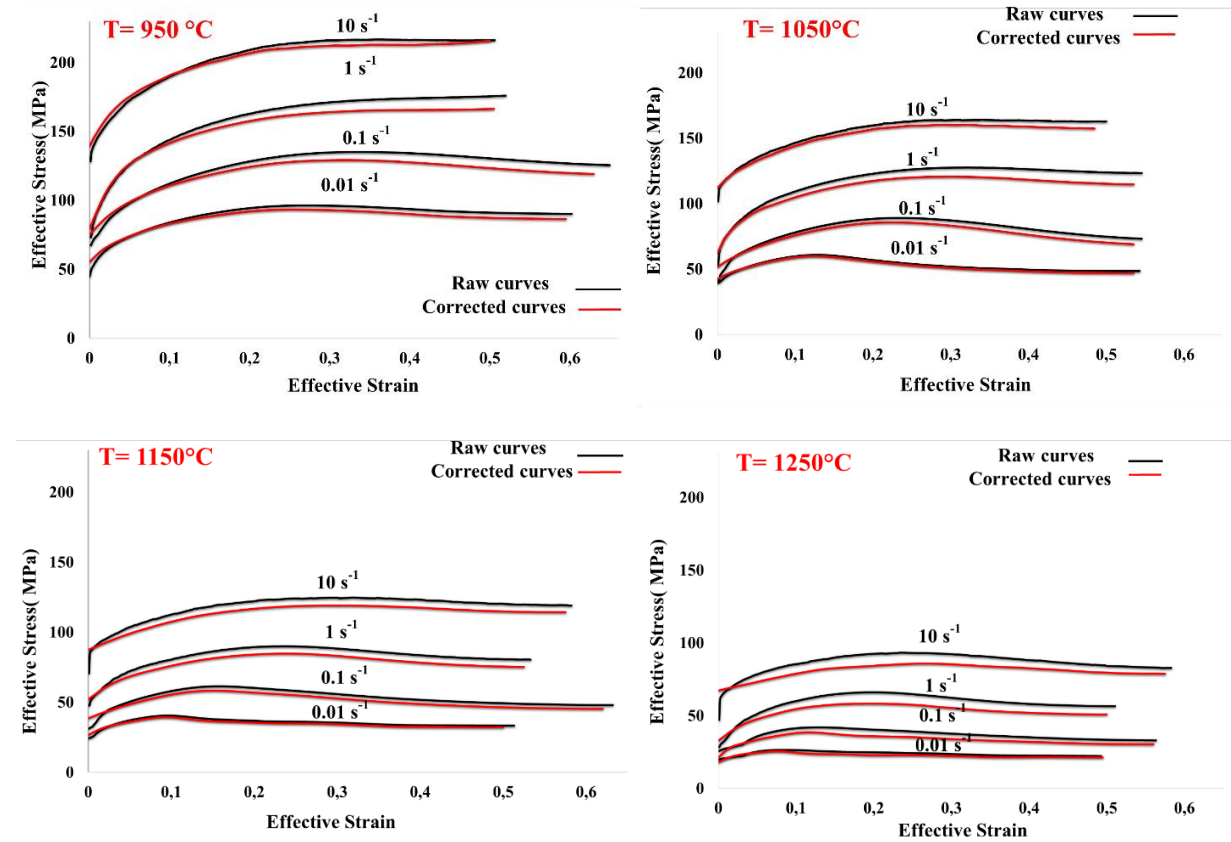


Figure 34 : Stress-strain curves of the 38MnSiV5 for the temperatures (950 °C, 1050 °C, 1150 °C and 1250 °C) and strain rates (0.01 s⁻¹, 0.1 s⁻¹, 1 s⁻¹ and 10 s⁻¹), raw curves and curves after all corrections.

2.3. Conclusion

Compression tests are carried out on the Gleeble 3500 to determine the rheological behavior of 38MnSiV5 over temperature ranges from 950 °C to 1250°C and strain rates from 0.01 s⁻¹ to 10 s⁻¹.

In order to reproduce the austenitic grain size distribution found at the industrial scale at the laboratory scale, a series of thermal cycles were carried out using the thermal etching technique to reveal the prior austenitic grain boundaries and determine their distribution.

The experimental results confirm the thermo-viscoelastic behavior of the material and also show the activation of the DRV and DRX phenomena under the temperature and strain rate conditions investigated.

After testing, the flow stress curves versus (ϵ , $\dot{\epsilon}$, T) are corrected to consider the friction that occurs during the test between the sample and the dies, but also to consider the heating of the sample during the deformation and the variations in strain rates. The analytical procedure for making these corrections was detailed.

The curves obtained after all the corrections will be used in the next chapters, in their tabulated form (Appendix 1) for the finite element numerical simulations of the crankshaft hot forming process to consider the rheological behavior of the 38MnSiV5 steel correctly.

**Chapter 3. Influence of hot forging
cycles on the topography and
mechanical properties of the tool**

During the three steps of crankshaft forging, the heated billet moves between the two preheated dies: upper and lower dies. The study of the influence of forging cycles on the topography and mechanical properties is only conducted on the rough forging die. This choice is justified by its wide range of local geometries and the intensity of defects after 20,000 cycles. This die is in direct contact with the billet before and during forging (the time for positioning the billet on the die before forging is 4 seconds).

The tool geometry (weight of 250 kg and dimensions of $L 700\text{ cm} \times l 270\text{ mm} \times H 170\text{ mm}$) is problematic for its analysis in its whole. So, an approach considering variations in tool geometry was developed. The tool was divided into distinct zones, classified according to geometry, comprising concave, convex, flat and bottom of the engraving zones. Local observations were then carried out on the critical tool zones to monitor the tool performance at different stages: new (0 cycle), intermediate (11,800 cycles) and end of life (20,000 cycles) according to the production expertise. Three aspects were considered, including evolution of topography, measurements of mechanical properties (Young's modulus and hardness) and evolution of microstructure. A total of 15 zones of the crankshaft surface were analyzed. In this chapter only a distinct main zone will be presented: the concave, convex, flat and the bottom of engraving. The unmentioned zones, with identical geometry, exhibited identical behavior.

Concerning topographical measurements, they were conducted prior to the cutting of the dies at different life cycles (0; 11,800 and 20,000 cycles). This approach is chosen to avoid damaging the surface topography post-cutting, considering the complex geometry of specific zones and the difficulty associated with accessing deep areas. Due to the substantial weight and dimensions of the dies, a replication method has been employed to capture surface topography.

Subsequently, a study was conducted to examine the influence of forging cycles on mechanical properties (Young's modulus and hardness) using nano-indentation tests. The aim is to track the evolution of these two parameters as a function of the lower die lifecycle.

3.1. Identification of the analysed zones

Four types of zones are geometrically identified: concave, convex, flat and bottom of the engraving (Figure 35). In the concave zone, at 11,800 cycles, a network of cracks (referred to as "heat checking") begins to settle due to thermal fatigue (Table 10). After 20,000 cycles, this network of cracks has significantly propagated, resulting in the formation of deeper crack (Table 10). In the convex zone, for both 11,800 and 20,000 cycles, wear and cracks in various directions are observed, with a more pronounced occurrence towards the end of the tool service life (Table 10). Concerning the flat zone, the heat checking induced by thermal fatigue becomes apparent at 11800 cycles, intensifying at 20,000 cycles. Regarding the engraving bottom, visually, the area is significantly less affected across the three studied life cycles (Table 10).



Figure 35: The selected zones: concave (1), convex (2), flat (3) and bottom of the engraving (4).

Table 10: Pictures of the concave, convex, flat, and engraving bottom zones during the lifespan cycles.

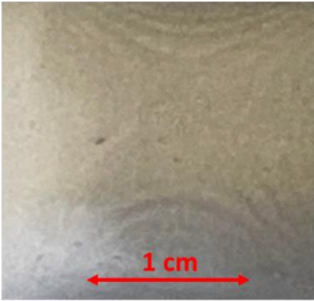
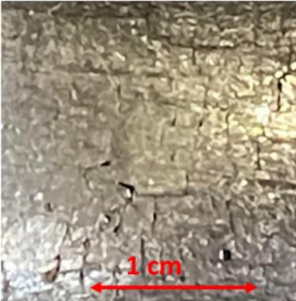




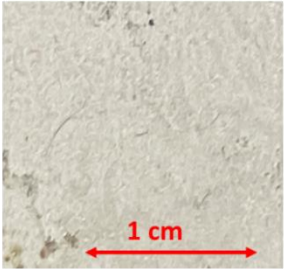
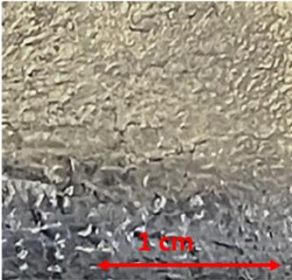
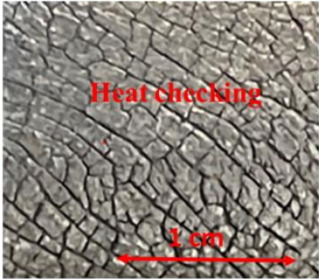


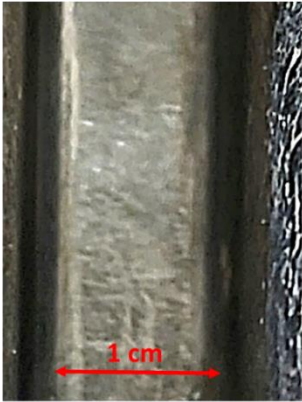
	0 cycle	11,800 cycles	20,000 cycles
Concave zone	 A smooth, light-colored concave surface. A red double-headed arrow at the bottom indicates a 1 cm scale.	 The surface is heavily textured and shows signs of wear. A red double-headed arrow at the bottom indicates a 1 cm scale.	 The surface is dark and shows significant cracking. Red text labels 'Heat checking' and 'Crack' point to specific features. A red double-headed arrow at the bottom indicates a 1 cm scale.
Convex zone	 A smooth, light-colored convex surface. A red double-headed arrow at the bottom indicates a 1 cm scale.	 The surface is heavily textured and shows signs of wear. A red double-headed arrow at the bottom indicates a 1 cm scale.	 The surface is dark and shows significant wear and fatigue. Red text labels 'Wear and fatigue' point to specific features. A red double-headed arrow at the bottom indicates a 1 cm scale.
Flat zone	 A smooth, light-colored flat surface. A red double-headed arrow at the bottom indicates a 1 cm scale.	 The surface is heavily textured and shows signs of wear. A red double-headed arrow at the bottom indicates a 1 cm scale.	 The surface is dark and shows significant cracking. Red text labels 'Heat checking' point to specific features. A red double-headed arrow at the bottom indicates a 1 cm scale.
Bottom of the engraving zone	 A smooth, light-colored surface. A red double-headed arrow at the bottom indicates a 1 cm scale.	 The surface is heavily textured and shows signs of wear. A red double-headed arrow at the bottom indicates a 1 cm scale.	 The surface is dark and shows significant wear. A red double-headed arrow at the bottom indicates a 1 cm scale.

Table 11 shows the maximum temperatures and contact pressures encountered in these 4 zones. These results are based on Stellantis' numerical model of the hot-forged crankshaft, which will be detailed in Chapter 4.

Table 11 : Maximum temperature T_{\max} and maximum contact pressure P_{\max} from numerical simulation of the hot forging of the crankshaft.

Zones	T max (°C)	P max (MPa)
Concave	650	100
Convex: Bossing	936	220
Flat	719	130
Bottom of the engraving	285	30

According to numerical simulations (Table 11), the convex zone experiences the highest levels of temperature and contact pressure. This elucidates why this zone undergoes the highest degree of damage detectable by the naked eye. The Stellantis forging production team mentions that this zone is particularly problematic due to its elevated temperatures during forging. Figure 36 presents the results of temperature measurements using a thermal camera after lubrication. Despite the cooling effect, the temperature still reaches 300 °C. The concave and flat zone are also exposed to high temperatures (650 °C for the concave zone and 710 °C for the flat zone), coupled with contact pressure, this may explain the formation of surface cracks. The contact conditions in the engraving bottom are less severe compared to the other zones, which is why this zone does not show any visual defects.

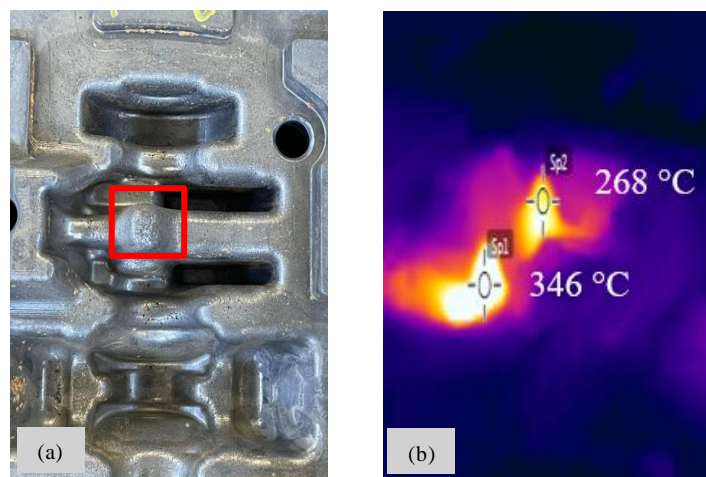


Figure 36: Temperature measurement results of the convex zone after forging and after lubrication: (a) target area, (b) thermal picture

3.2. Influence of hot forging cycles on the topography

The topography of forging dies is a crucial factor in hot forging. Over the forming cycles, this surface condition will change; each modification, however small, can have a significant impact. By closely monitoring these modifications, it becomes possible to identify early signals of degradation, wear, or other forms of damage.

This section is dedicated to analyzing the evolution of the topography of hot forging dies throughout their lifecycle. Through this investigation, a database for developing predictive models will be established. It will facilitate proactive interventions to reduce the risks of damage and optimize maintenance strategies for hot forging dies.

3.2.1. Methodology for topography analysis

Topographical measurements are carried out using the interferometric tools prior to the cutting of the dies. A replication method has been employed to capture surface topography, enabling the acquisition of samples with a flat base of 1 cm² for each measurement.

After a selection of the measurement zone (Figure 37a) the procedure begins with computer-aided design (CAD) modeling of this area. Identical zones were considered. A CAD model of the negative of the previously modeled zone is then created (Figure 37b). All that remains from this negative is a mold which geometry is a 1 cm square base. The thickness of this mold is matched to the area to be measured (about few millimeters). This mold has a cavity (Figure 37c) which will allow the injection of a fine resin. After cooling, the resin will have the topography of the measured zone. Additive manufacturing is used to 3D print the mold, ensuring faithful reproduction (Figure 37c). This methodology results in the successful production of topographical replicas (1 cm²) of the targeted zone (Figure 37d), preserving the topography of the surface for future analysis (Ersen & Güngör, 2013; Chang *et al.*, 2019).

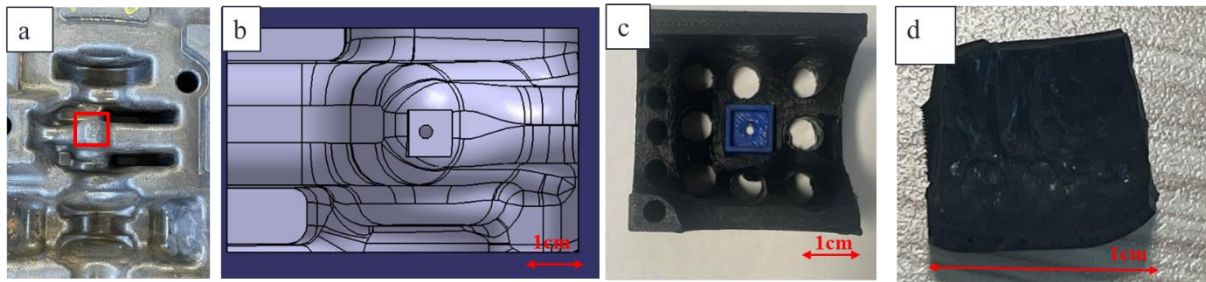


Figure 37: Convex zone: a) Measurement zone on the lower die, b) CAD model, c) 3D printed mold, d) replica of the area.

After retrieving the replicas, topographic measurements are conducted using the interferometer ZYGO NewView. The measurement objective of an interferometer is to precisely quantify the topographical characteristics of a surface. Grounded in the principle of interference between two optical wavefronts, one reflected from the object surface and the other from a

reference mirror, this instrument aims to capture minute variations in surface geometry, down to the nanoscale. The obtained measurements allow for a detailed assessment of roughness, shape, and other properties (Petzing, 2010). The measurement device and measurement parameters are given in (Figure 38).

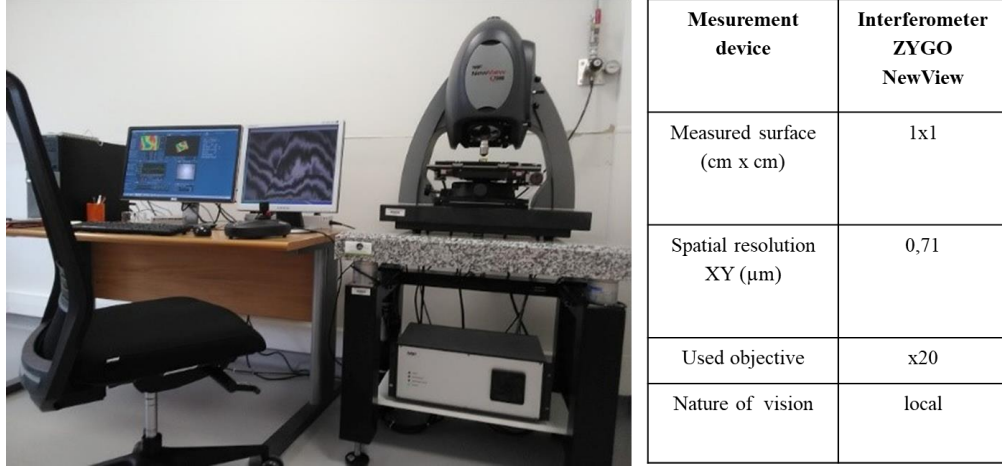


Figure 38: Interferometer and measurement parameters.

3. 2.2. Results and Discussion

Measurement results can be divided into two categories: qualitative results, which include 3D images illustrating the evolution of the surface state, and quantitative data, which involve roughness parameters extracted from the 3D images using topographical analysis software (Mountains®, Digital Surf). Considering roughness parameters, representative of the phenomena observed (cracks, material deposits, surface irregularities) are selected. These parameters include arithmetical mean height (S_a), maximum peak height (S_p), and valley depth (S_v). Table 12 summarizes the used parameters, their definitions, and their links with the observed phenomena.

Table 12: Roughness parameters and their relationships with damage phenomena (Jaber. A, 2022).

Results		Significance of each result in our case
Arithmetical mean height (Sa)	It provides the arithmetic mean, in absolute value, of the height difference of each point.	It is used to compare the rough surfaces of tooling. A higher Sa indicates greater roughness, which may be associated with phenomena such as wear and cracks.
Maximum peak Height (Sp)	It is the height of the highest peak in the defined area.	A higher Sp can indicate specific features related to deposits on the surface, such as oxides, lubricant residues, and irregularities resulting from material friction
Valley Depth (Sv)	It is the absolute value of the height of the tallest pit in the defined area.	The increase in this parameter suggests more pronounced variations in depth. A higher Sv can indicate a greater maximum depth of pits, often associated with features such as cavities, cracks, or other irregularities on the surface of the dies.

The results of the evolution of roughness parameters in relation to the tooling life cycles for all zones (concave, convex, flat, and engraving bottom) are presented in the Figure 39 and Figure 40. 15 measurements were taken for each area. The roughness of the other zones not shown (9 zones not presented (annex 2)), also measured (15 measurements for each zone), exhibits the same behavior.

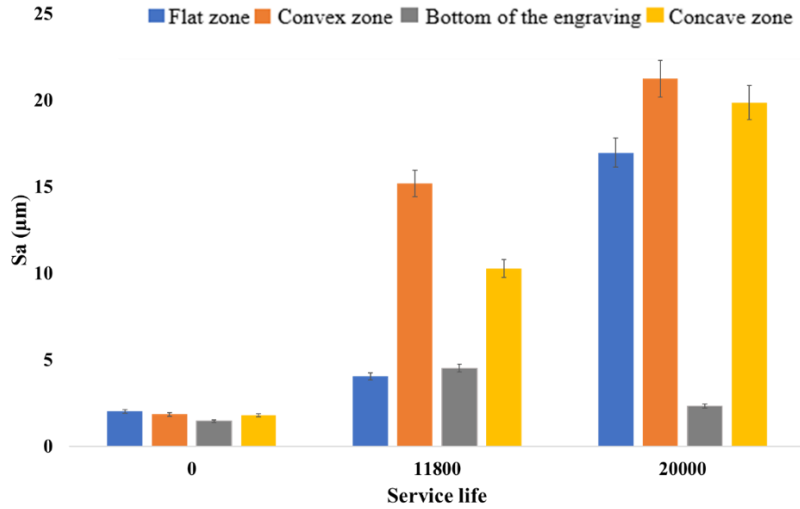


Figure 39: Arithmetical mean height (Sa) evolution as a function of the die's life cycle.

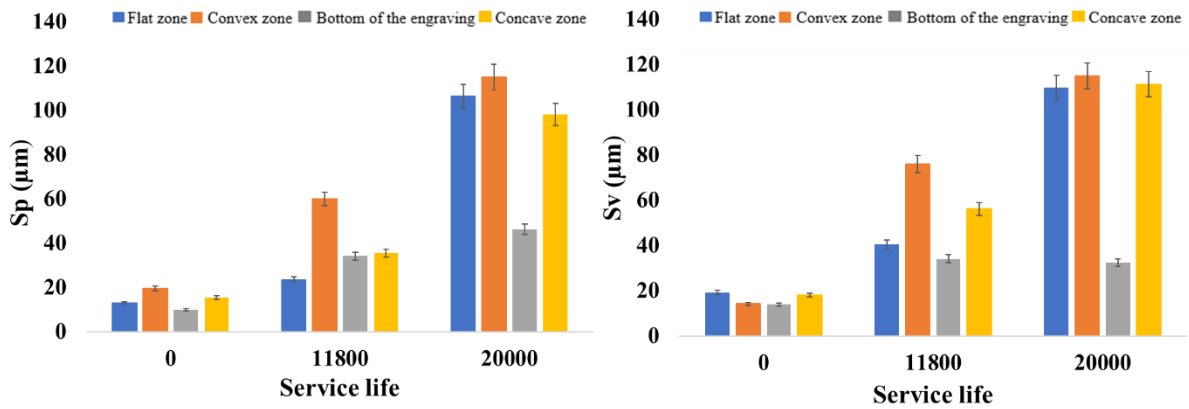


Figure 40: The evolutions of Sp and Sv parameters as a function of the die's life cycle.

Regardless of the nature of the defects or the studied geometry, surface roughness demonstrates an increasing trend throughout the tool life cycle. The increase in these roughness parameters over the tool lifecycle generally indicates a deterioration of the tool surface due to continuous wear and damage processes during hot forging.

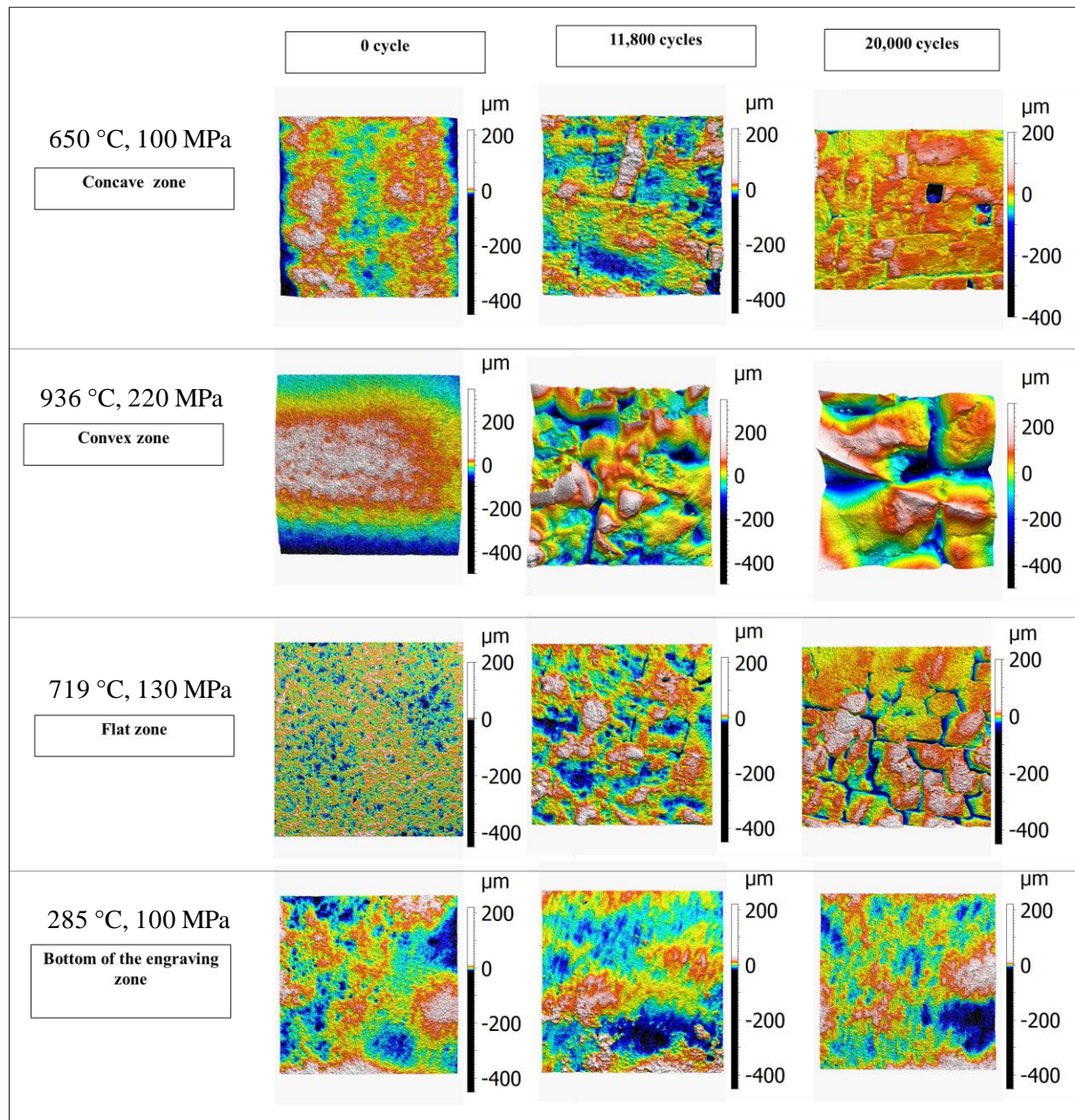
During hot forging, the concave, convex, and flat zones are subjected to significant thermo-mechanical stresses and repeated loads (Table 11). When interacting with the billet, micro-defects may form due to the intense conditions, resulting in surface irregularities. Furthermore, the constant contact and friction between the tool and the billet contribute to wear, further altering the surface topography. The cumulative effect of these phenomena over multiple forging cycles leads to an increase in average roughness (Sa), causing local variations in surface height, such as material deposits, oxides, and scaling. These variations manifest as more pronounced peaks in the roughness

profile, which can account for the rise in S_p . The formation of cracks contributes to the increase in S_v .

The topography of the concave, convex, and flat zones become increasingly rough with the progression of the lifecycle (Table 13). This increase in roughness is due to the severe working conditions (Table 11) and to the geometry of the zones (except for $N = 0$). Upon examining the convex zone, its surface appears to be rougher compared to the other zones. This is linked to higher contact conditions, such as temperature, contact pressure, and contact time with the billet ($T_{\text{tool}} = 936 \text{ }^\circ\text{C}$, $P = 220\text{MPa}$, $t_{\text{contact}} \sim 4.2\text{s}$). Additionally, the geometry of the convex zone makes it more prone to stress concentration. The network of cracks at 20,000 cycles is more pronounced in the flat zone compared to the concave zone, and this phenomenon appears to be linked to higher temperature and contact time in the flat zone compared to the concave zone. The bottom of the engraving zone exhibits the lowest level of roughness, no significant topography changes are observed. This is likely due to the absence of significant wear, as it is subjected to less severe working conditions ($T_{\text{tool}} = 285 \text{ }^\circ\text{C}$, $P = 30 \text{ MPa}$ (Table 11)).

Chapter 3. Influence of hot forging cycles on the topography and mechanical properties of the tool

Table 13: The evolution of the topography of the different zone as a function of the lifecycle.



3.2.3. Conclusion

The gradual increase of the roughness parameters over cycles suggests a gradual degradation of the tool surface, due to complex phenomena such as wear, and fatigue induced by thermal and mechanical stresses during the forging process. The monitoring of these changes throughout the process will allow for the anticipation of wear by specifically identifying areas prone to increased deterioration. Targeted intervention where necessary will significantly reducing maintenance costs by avoiding premature tool replacements.

3.3. Influence of hot forming cycles on the mechanical properties of hot forging tool

In the hot forging of crankshafts, the temperature of the heated billet is approximately 1290 °C. Upon contact, the temperature of the tool (preheated at 140 °C) increases. This temperature increases, accompanied by applied load, initiates a series of significant changes in the material behavior. These changes involve a decrease in hardness and the initiation of damage mechanisms such as wear and fatigue (Emamverdian *et al.*, 2021).

In this section, an examination of the influence of hot forging cycles on the hardness and Young's modulus of matrices at different stages of the lifecycle (new, 0 cycles; mid-life, 11,800 cycles; end of life, 20,000 cycles) is being conducted. This approach is justified by the major influence of these mechanical properties on the structural integrity and performance of forging tools. This analysis relies on data derived from nano-indentation tests, as well as results obtained from scanning electron microscopy (SEM) and energy-dispersive X-ray spectroscopy (EDS). We are focusing on three different zones: concave (1), convex (2), and flat (3). For technical reasons we have not been able to examine the bottom of the engraving zone (This restricted zone does not allow the capture instrument to be positioned correctly).

3.3.1. Experimental Procedures

Nanoindentation tests are conducted using the Hysitron TI 980 TriboIndenter nanoindenter (Figure 41). The platform is equipped with a nano-indentation module, an optical microscope, and a scanning probe microscope (APM) module. The indenter employed is a Berkovich tip. Nano indentation is performed on the 3 zones (concave, convex and flat) of 3 crankshaft forging dies at stages: 0 cycles, 11,800 cycles, and 20,000 cycles. The initial matrix at 0 cycle is nitrided

Chapter 3. Influence of hot forging cycles on the topography and mechanical properties of the tool

X38CrMoV5 with a nitriding thickness of $160 \pm 10 \mu\text{m}$. The samples are cut cross-sectionally (1 cm^3) then prepared using conventional metallography techniques, including embedding in epoxy resin and mechanical polishing with increasingly fine abrasive papers up to P1200. Mirror polishing is conducted until achieving a surface finish of $1 \mu\text{m}$, using a Nap polishing cloth.

Indentations are performed under load control with an applied force of 10 mN for 0.3 seconds loading and unloading on a $270 \mu\text{m}$ length, extending from the surface to the core of the samples. This length comprised successive grids, each measuring $20 \mu\text{m} \times 20 \mu\text{m}$, with 100 indentations conducted on each grid. The image of the nano-indentation imprint on a zone from a new tool is presented in Figure 42.

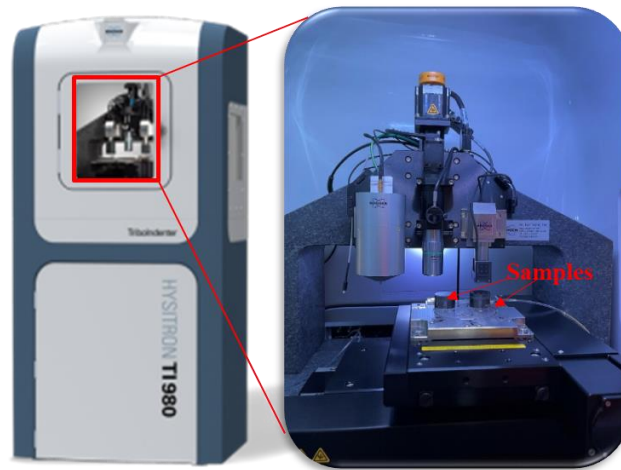


Figure 41: Hysitron TI 980 TriboIndenter nanoindenter.

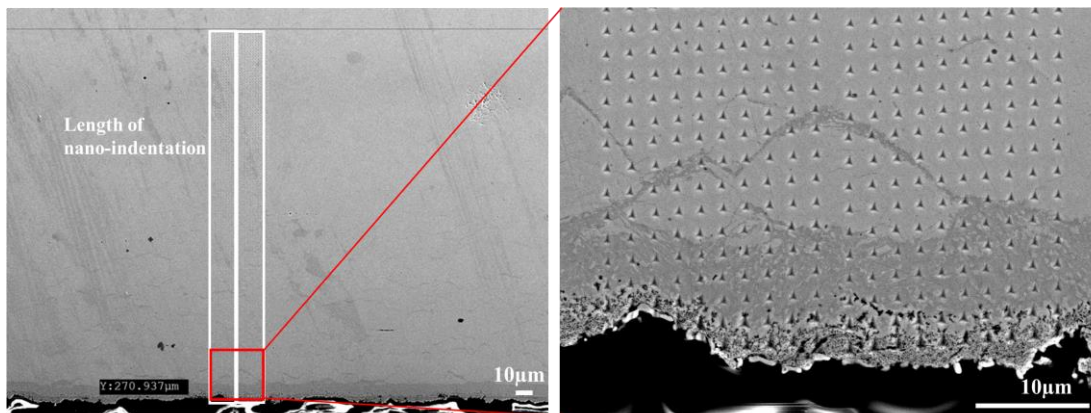


Figure 42: Nano-indentation test sample (0 cycle convex zone).

3.3.2. Results and Discussion

- **Nano-indentations tests results**

The results of the evolution of hardness and Young's modulus in different zones (concave, convex, and flat) as function as the depth (Y), from the surface to the core of the samples, in relation to the matrix lifecycle are presented in this section.

The hardness evolution (Figure 43) of the convex sample shows significant differences between the three life stages (0, 11800, 20000). When the die is new, the nitrided surface mean hardness is approximately 9 GPa. The hardness shows a slight downwards trend as the indenter goes deeper until it reaches 158 μm depth. The trend then drastically decreases until reaching a minimum hardness of 6 GPa at a depth of 181 μm , which is similar to the tool hardness at 11800 cycles. This means that at mid-life, the hardness of the tool has undergone a reduction of 40%. Furthermore, the samples corresponding to 11,800 and 20,000 cycles both exhibits nearly constant hardness over the indentation range. However, it is evident that hardness decreases as the tool undergoes more cycles, as shown in the (Figure 43). The hardness of the 20000-cycle sample is 50% smaller compared to the hardness value at 11800 cycles. Comparing between both of the new and end-of-life tool, there is a drastic reduction of 60% in hardness throughout the 20000 cycles.

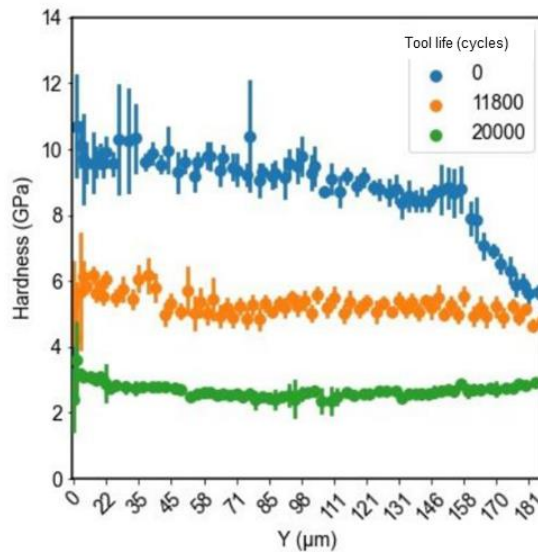


Figure 43: Evolution of Hardness versus position in the tool depth and tool life (convex zone).

Further nano-indentation tests (Figure 44) are carried out on the cross-section to determine the change in hardness along a greater depth (Y) of the sample extracted from the new convex zone. The tests demonstrate the decrease of the hardness measured near the surface.

The nano-indentation tests also indicated that the core hardness is approximately 5 GPa. To confirm this results, Vickers hardness tests were conducted at depths of 200 and 300 μm . The

results of these tests confirm a core hardness of about 5 GPa. The hardness of the sample extracted from the convex zone at 20000 cycles is lower than the initial hardness of the core of the sample extracted from the new tool.

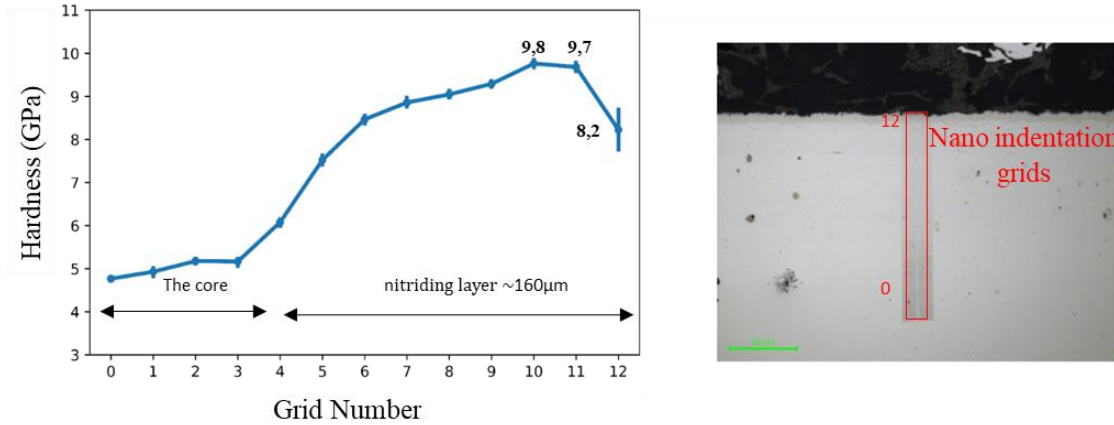


Figure 44: Evolution of Hardness versus grid number in the tool depth (convex zone 0 cycle).

The results for the concave and flat zones are presented in Figure 45. They differ from those of the convex zone.

While both the concave and flat zones exhibit a decrease in hardness between the new and mid-life samples (11,800 cycles) with a 40% decline for the concave zone (hardness of 6 GPa at the mid of life) and a decline of 50% for the flat zone (5 GPa at the mid of life), the hardness remains stable between the mid-life and end-of-life cases for both zones.

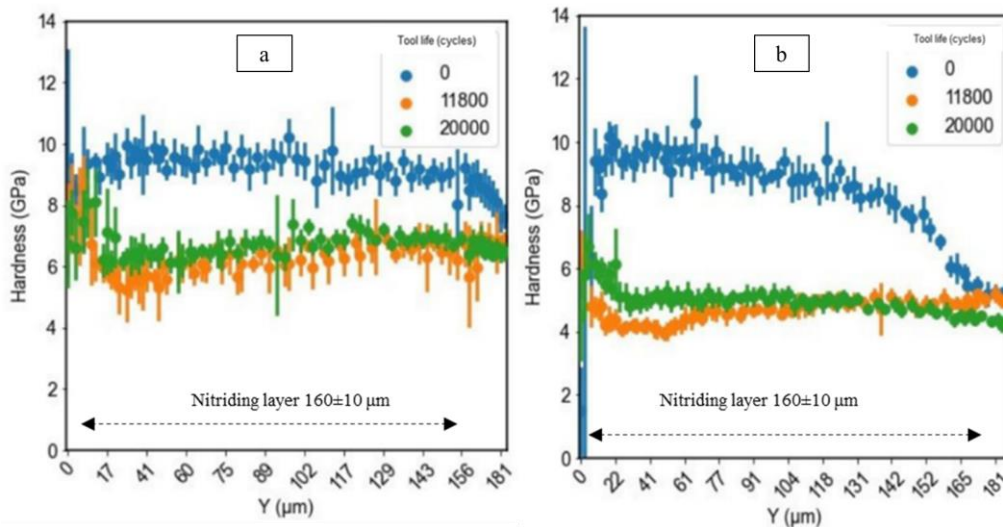


Figure 45: Evolution of Hardness versus position in the tool depth and tool life: (a) concave zone, (b) flat zones.

The results of the elastic modulus, determined from the reduced modulus (S. Kossman, 2017) are presented in Figure 46 and Figure 47.

E_R is related to the Young's moduli and Poisson's ratios of the indenter (E_i , ν_i) and the material (E , ν) by the relation:

$$\frac{1}{E_R} = \frac{1 - \nu_i^2}{E_i} + \frac{1 - \nu^2}{E}$$

At 0 cycle, the three zones (convex, concave and flat) exhibit the same value of Young's modulus in the nitride layer (230 MPa). Regarding the convex zone (Figure 46), there is a notable decrease of approximately 30 GPa (representing a 15% difference) in the elastic modulus between the new tool (230 GPa) and the mid-life and end-of-life tools (200 GPa). However, there is no discernible difference in behavior between the 11800-cycle sample and the 20000-cycle sample.

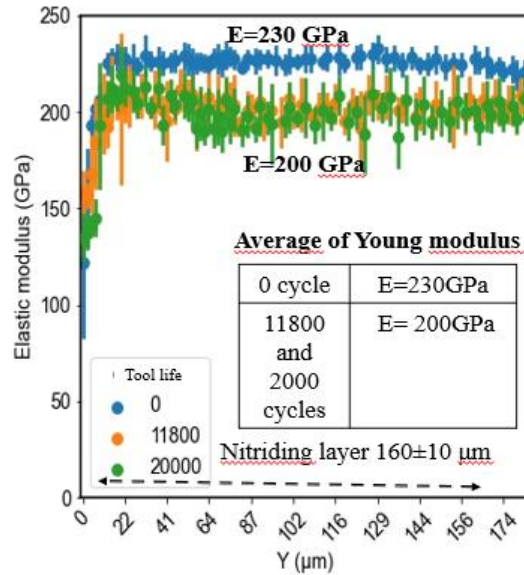


Figure 46: Evolution of Young’s modulus versus position in the tool depth and tool life (convex zone).

The results for the concave zone show no significant difference between the three different cases (0, 11800, 20000 cycles). The tests for the flat zone yield almost identical results, with no significant change in the elastic modulus (230 GPa) between the three tested samples at 3 different life cycles (Figure 47).

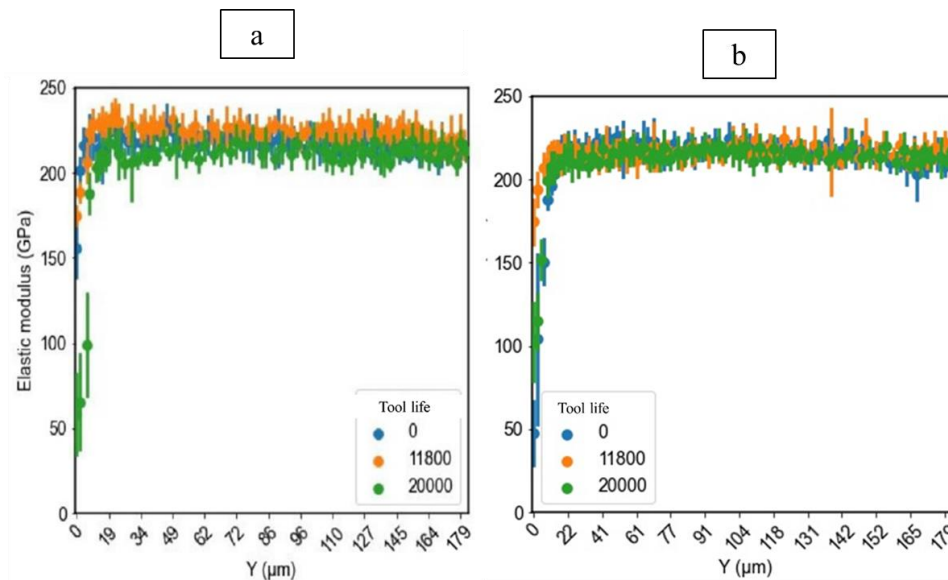


Figure 47: Evolution of Young modulus versus position in the tool depth and tool life: (a) concave zone. (b) flat zones.

- **Microstructural analysis**

In order to understand the reasons why the mechanical properties (Young's modulus and hardness) evolve in this way throughout the life cycle in different study zones, a microstructural analysis using optical microscopy (OM) and Scanning Electron Microscopy (SEM) is conducted. The samples are prepared using conventional metallography techniques, including embedding and mirror polishing. Then, a chemical etching is performed with a 3% nital solution for precisely 15 seconds.

- **Convex zone:**

The optical microscopy and SEM images of the microstructure subjected to nital etching of the sample from the convex zone in the new matrix are presented in Figure 48. The microstructure appears martensitic in the nitrided zone and in the core. The presence of pores (Figure 49) provides a possible explanation for the low values at the start of the indentation test. These observations confirm that the combination zone is a brittle area susceptible to cracking during forging cycles.

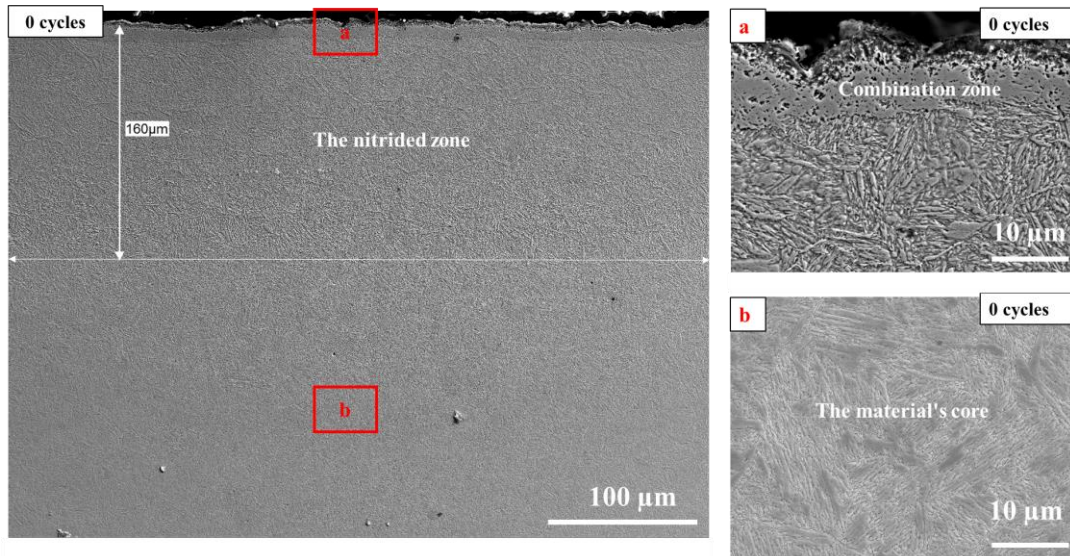


Figure 48: SEM images of the microstructure of a new nitrided tool (3 % nital etching).

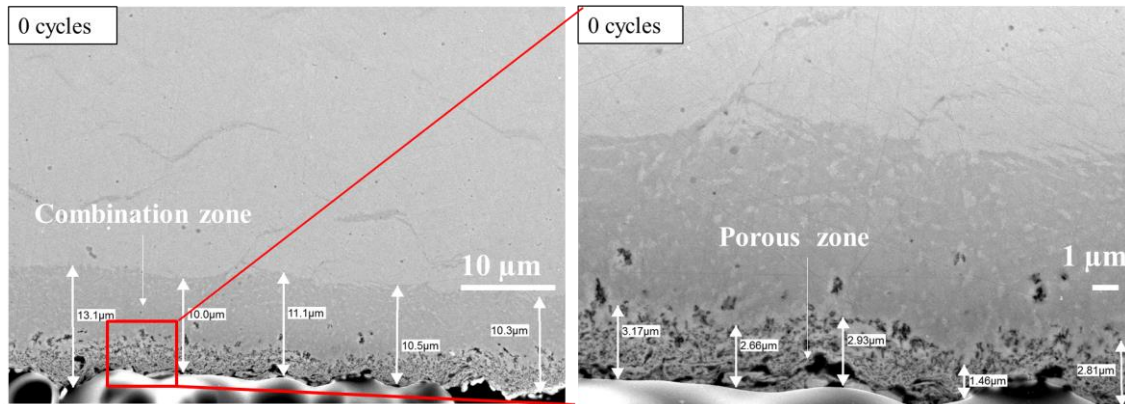


Figure 49: SEM images of the microstructure of a new nitrided tool (no etching).

Figure 50 shows SEM images of convex zone samples at 11800 cycles and 20000 cycles. Several notable macrocracks of different lengths and directions are visible in both samples, propagating deeper. Macro-cracks initiate from micro-cracks initiated on the oxide layer and propagate into the material surface, thus constituting the network of cracks. These cracks result from the thermomechanical stresses concentration, and reduced material strength. Consequently, pre-existing micro-cracks propagate gradually, leading to a decrease in hardness and substantial deterioration of other local mechanical properties.

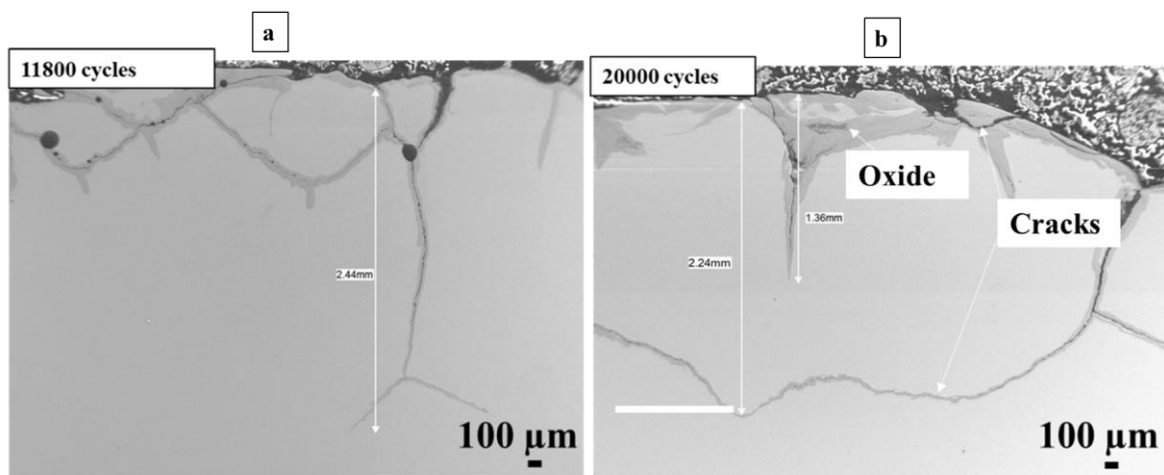


Figure 50: SEM images of the microstructure of convex zone at: (a) 11800 cycles, (b) 20000 cycles.

Figure 51 presents the evolution of the microstructure of samples at 11800 and 20000 cycles as a function of depth. Both samples show the change of the microstructure from the initial martensitic microstructure to a microstructure of globular cementite (or metal carbides) as a consequence of exposure to a temperature gradient along the forging cycle. During their lifecycle, the dies are exposed to heating and cooling cycles as they come into contact with the billet at a temperature of 1200°C, as well as frictional heating. With a high production rate of 250 pieces per hour. The die subjected to 11,800 cycles experiences temperature variations for 47.2 hours, while the one subjected to 20,000 cycles experiences them for 80 hours. At a depth of 2 mm, martensite begins to reappear, and the laths progressively refine further with increasing depth.

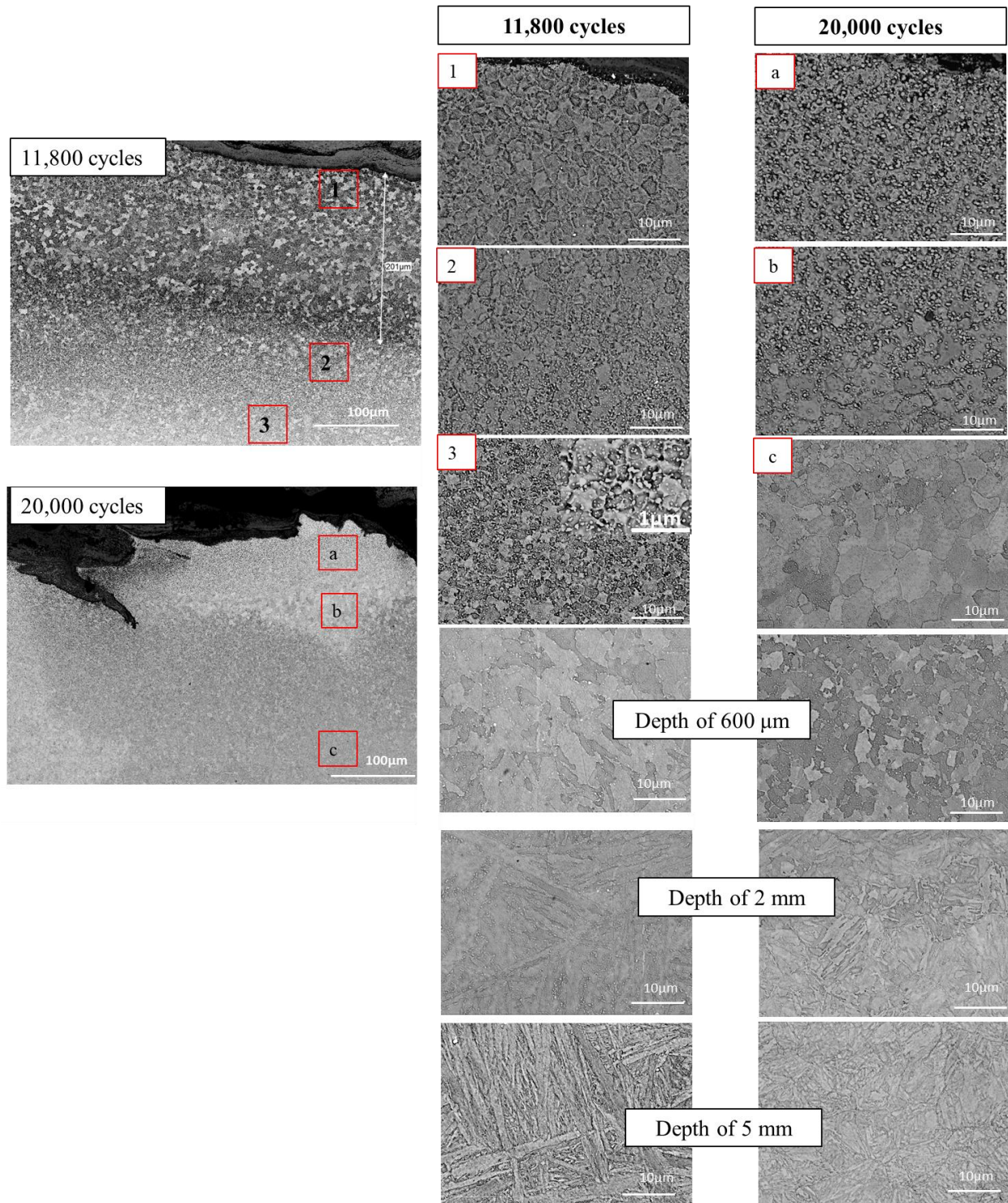


Figure 51: SEM images of samples from the convex zone at 11800 and 20000 cycles.

Microstructure changes of X38CrMoV5 steel grade related to exposure to elevated temperatures for an extended time have been reported in the literature (Hubicki *et al.*, 2021; Michaud, 2006; Salem, 2009). Figure 52 shows the effect of the temperature and exposure time on the microstructure and on the hardness of X38CrMoV5 steel. It shows that exposure to elevated temperatures for a long enough period would result in the growth of carbide precipitates.

The decrease in hardness can be explained by cyclic thermal softening associated with microstructural changes that can influence the material behavior under mechanical stresses. High pressure might also affect such decrease. When the secondary tempering temperature of the steel is exceeded, microstructural changes related to diffusion phenomena occur, resulting in the coalescence of carbides and a transformation of martensite into globular cementite. Globular cementite is generally less hard than martensite and may be more prone to deformation and wear (Michaud, 2007; Salem, 2009).

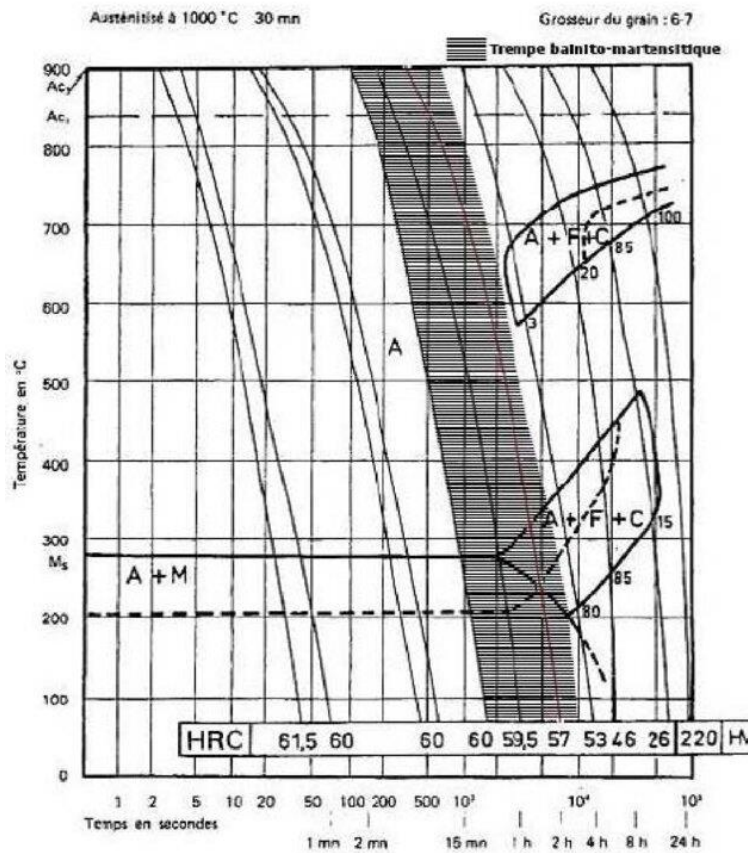


Figure 52: TRC Diagram of X38CrMoV5 Steel (Salem, 2009).

Moreover, microstructural analysis reveals the disappearance of the nitrated layer in the convex zone at 11800 and 20000 cycles. Since nitriding imparts nitrogen on the surface of the material, its presence can serve as an indicator of the existence of the nitrated layer. The detection of nitrogen is made possible through Energy Dispersive Spectroscopy (EDS) analysis.

Given that the nitrogen energy peak appears around 0.4 keV, the EDS analysis results are presented up to 5 keV (Figure 53). The results indicate the presence of nitrogen in the samples at 0 and 11,800 cycles. However, the nitrogen peak is absent in the sample at 20,000 cycles. The quantification of nitrogen is not dependable with this analysis, which is why it is not presented; it merely allows for comparison between the samples. Analyzing the nitrogen contents reveals that the quantity of nitrogen decreases as a function of the lifecycle until reaching zero at 20,000 cycles.

It is not known whether this reduction and/or disappearance of nitrogen is due to diffusion (often approximated to values between 10^{-11} m/s and 10^{-9} m/s at temperatures around 1000 °C.), wear (loss of the nitrated layer during forging cycles), or both phenomena. However, this explains the decrease in hardness and, notably, the drop in Young's modulus. The disappearance of the nitrated layer significantly contributes to this decrease, leading to a decrease in Young's modulus until reaching intrinsic material values (204 GPa).

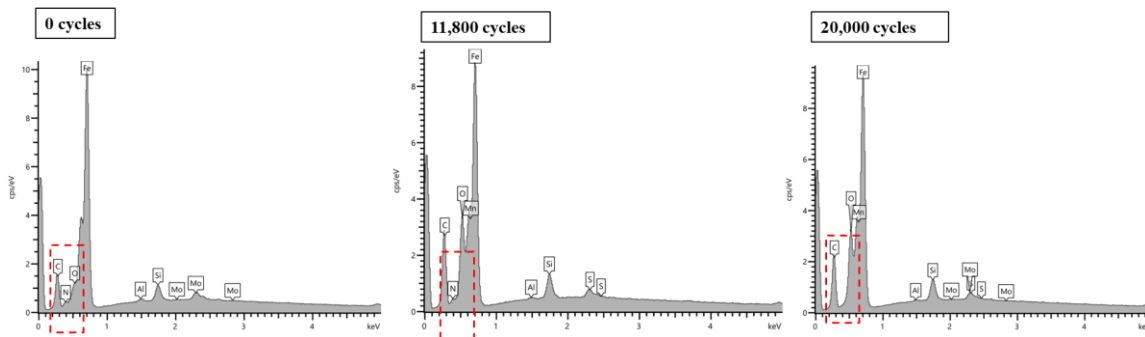


Figure 53 : The EDS spectra extend up to 5 keV for the convex zone at different lifecycle stages (0; 11,800; 20,000 cycles).

- **Concave zone:**

Figure 54 presents the microstructure of samples at 11800 and 20000 cycles for the concave zones. For both samples, the microstructure remains martensitic. The EDS analysis shows the presence of nitrogen in these samples (Figure 55). The presence of decarburization zones is observed at the interface between the oxide and the martensite laths. Decarburization is defined by the depletion of carbon content on the material surface (Jegou, 2009). Due to exposure to elevated temperatures in the presence of oxygen, oxide can form on the surface of the tool. This oxide may vary in thickness and homogeneity, and it can act as a protective barrier. After cycling, this layer is often fragmented by gas emissions, allowing oxygen from the air to penetrate more easily into the metal structure. The oxygen present in the air reacts with the carbon in the steel, resulting in the removal of carbon from the steel surface. Additionally, the presence of oxides can modify the surface properties of the tool, such as roughness. (P. Arnaud *et al.*, 2017) (P.Hairy, 2023)

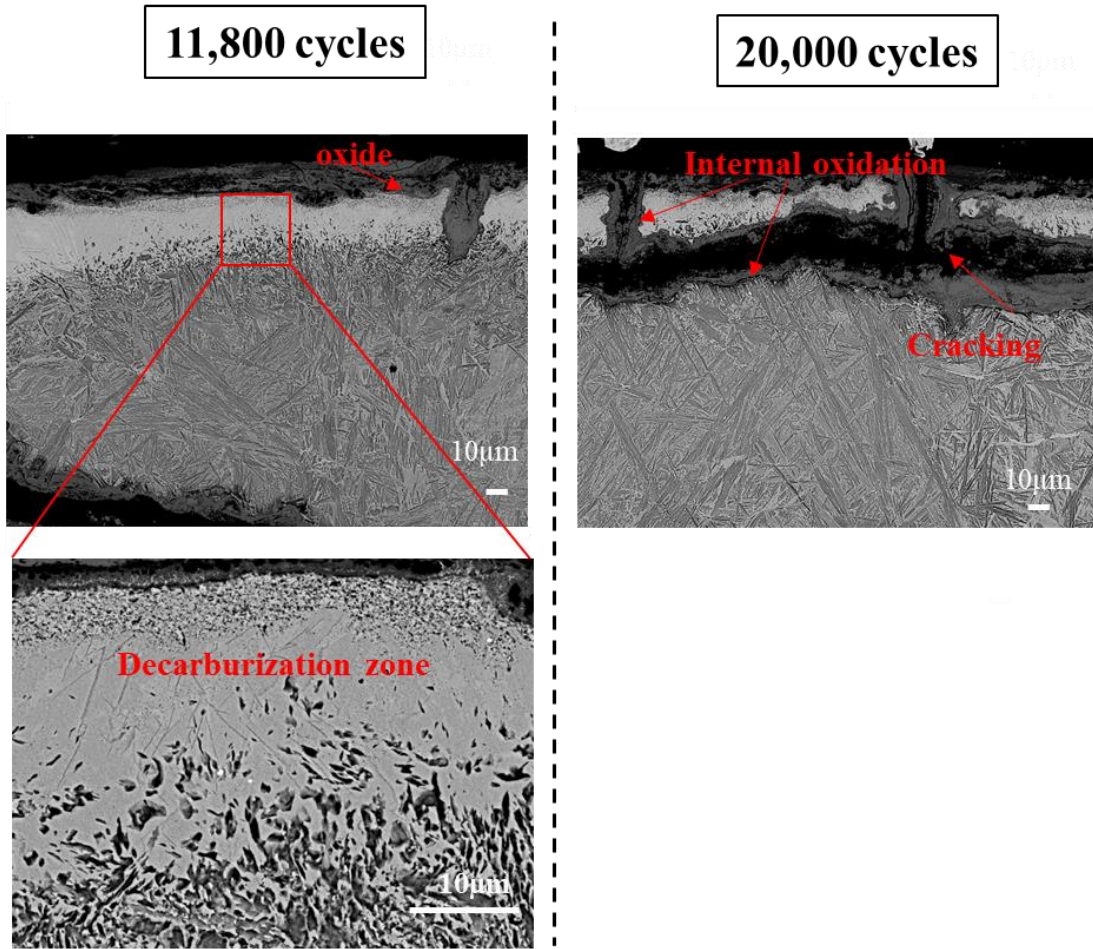


Figure 54: SEM images of samples from the concave zone at 11800 and 20000 cycles.

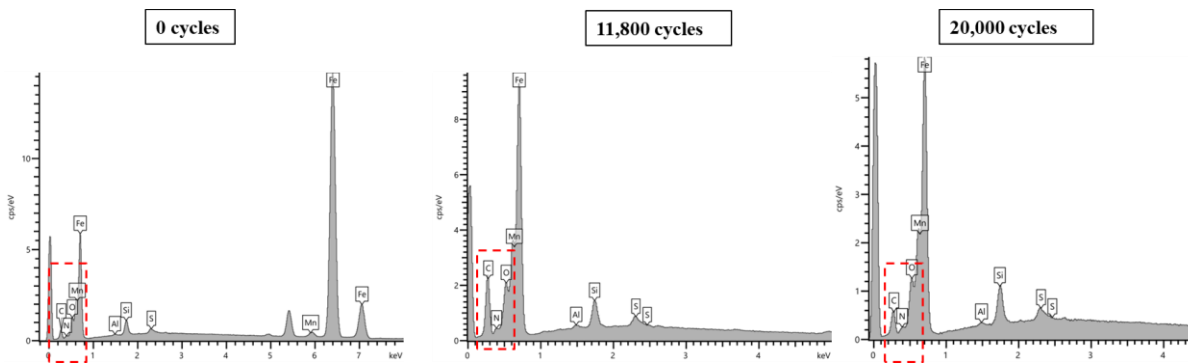


Figure 55: The EDS spectra extend up to 5 keV for the concave zone at different lifecycle stages (0; 11,800; 20,000 cycles).

- **Flat zone:**

The microstructures of the samples derived from the lower dies at 11800 and 20000 cycles in flat zones are presented Figure 56. The presence of decarburization zones is evident in both samples. However, in some regions of the interface, decarburization is not observed. Instead, a heterogeneous transformation phase emerges that is not easily identifiable. The presence of globular carbides in this phase may be explained by the initial microstructural change from the martensitic structure to globular cementite. Decarburization and microstructural changes lead to changes in mechanical properties, and the presence of these phenomena can explain the decrease in hardness (Figure 45 b). The EDS analysis shows the presence of nitrogen in these samples (Figure 57)

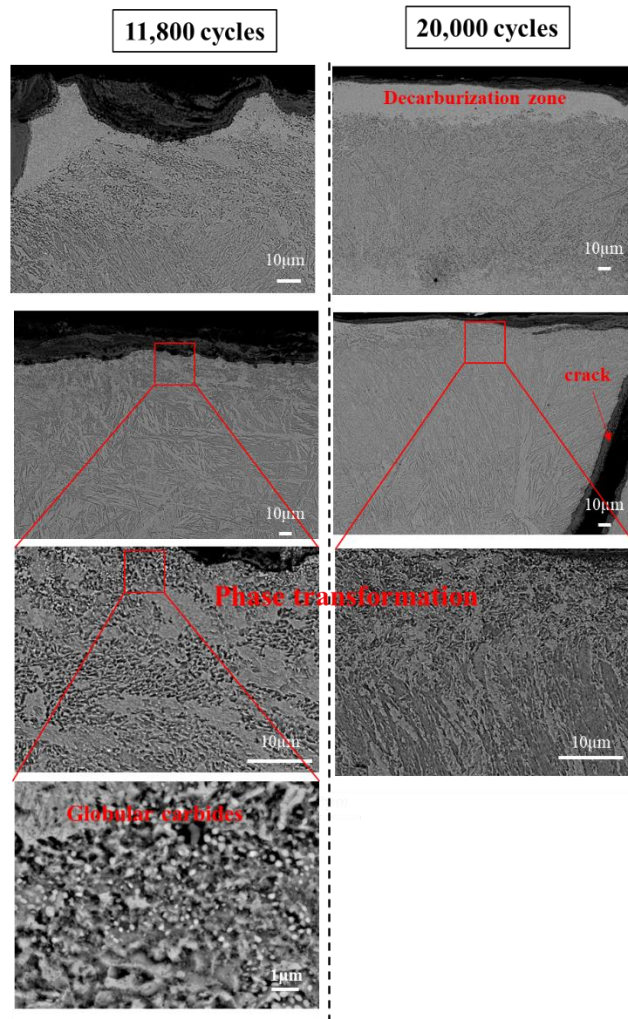


Figure 56: SEM images of samples from the flat zone at 11800 and 20000 cycles.

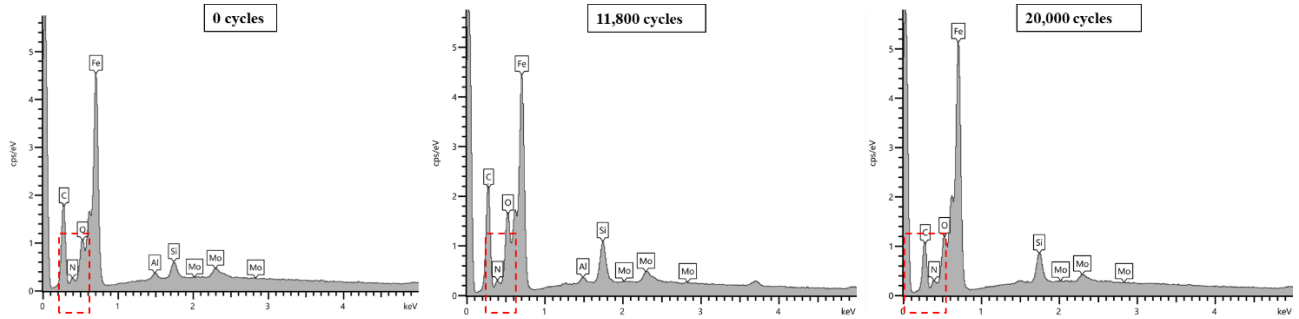


Figure 57: The EDS spectra extend up to 5 keV for the flat zone at different lifecycle stages (0; 11,800; 20,000 cycles).

3.3. Conclusion

The study on the influence of hot forging cycles on the mechanical properties of different geometric zones : concave, convex, and flat, derived from hot forging lower dies of crankshafts at various stages of life cycles (0, 11800, and 20000 cycles) reveals a correlation between the evolution of mechanical properties (hardness and Young's modulus measured by nano-indentation), the evolution of microstructure of the three zones over the life cycle, and the contact conditions to which the dies are subjected (temperature and contact pressure (Table 11)).

The results of nano-indentation tests show a significant decrease in hardness with increasing life cycles for all three zones (a decrease of 60% between 0 and 20000 cycles for the concave zone and 40% for the concave and flat zones). Microstructural observations using SEM have explained this decrease. Initially, cracks are observed on the oxide layer and along depths exceeding 1 mm in all three zones (appendix 3). These cracks, observed during and at the end of the life cycles of the dies, are mainly caused by thermomechanical stresses and a decrease in material strength. The analysis also revealed the transition from martensite to less hard phase, globular cementite, in the convex zone, with a similar transition begins in the flat zone. This transition is attributed to cyclic thermal softening induced by exposure to high temperatures (Table 11).

Microstructural analysis of the concave and flat zones confirms the presence of decarburization zones and a non-homogeneous oxide layer. Decarburization leads to a reduction in carbon content at the surface, contributing to a decrease in hardness and potentially affecting surface roughness. The formation of oxides acts as a protective barrier, but the heterogeneity of the layer can make it a zone for initiating deep cracks on the material surface.

Moreover, SEM/EDS analysis showed the disappearance of nitrogen in the convex zone at 20000 cycles and its trace presence at 11800 cycles, accompanied by a change in microstructure to less hard globular cementite. This appears to be accompanied by the disappearance of the nitriding layer due to wear or diffusion or both phenomena. This may explain the decrease in Young's modulus until reaching the intrinsic value of the material (204 GPa).



Chapter 4. Influence of hot forging cycles on the tribological behavior of the die

Tribological behavior, encompassing friction conditions, wear, and lubrication phenomena, plays a crucial role in determining the performance of tool steels in hot forging processes. This chapter focuses on the study of the influence of forging cycles on the tribological behavior of hot-forging tools. The main objective is to understand the impact of forging cycles on the evolution of friction, wear of the die, the role of oxides and consequently geometrical modifications during the tool life cycle. To achieve this, an experimental and numerical approach is adopted, combining numerical modeling of the forming of the crankshaft and experimental tests on the WHUST tribometer reproducing contact conditions encountered in industrial forging processes. Finally, specific numerical studies are conducted on the thermal and mechanical influence of oxides and geometric modifications resulting from wear on contact conditions.

4.1. Parameters affecting friction.

In hot forging process, the interaction between the tool and billet, particularly friction, plays a crucial role in shaping material flow, determining surface roughness, and influencing the longevity of the tools involved (Nielsen et al., 2017). Friction in hot metal forging is influenced by a multitude of parameters, many of which are challenging to precisely estimate or calculate. (Klocke, 2013) (Figure 58) illustrates various influencing factors that impact friction conditions within a dynamically changing contact surface on a microscopic scale. (Klocke, 2013).

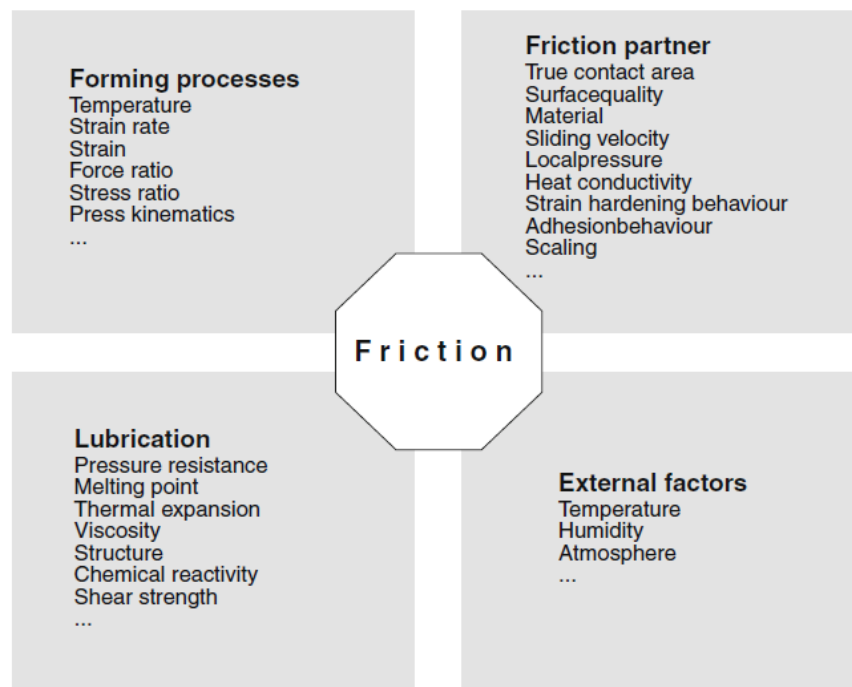


Figure 58 : Parameters affecting friction (Klocke, 2013).

4.2. Methodology of tribological tests

A numerical and experimental approach has been defined to study the different geometric zones of the lower crankshaft forming die over the life cycles (Figure 59). Firstly, the numerical approach involves finite element modelling of the crankshaft roughing stage, which is the most severe in tribological terms (Chapters 2 and 3). The numerical analysis will enable us to estimate contact pressure levels, sliding velocities and contact temperatures at key locations (the geometric zones selected in Chapter 3) in the forging die. Subsequently, these contact conditions are replicated, using the Warm and Hot Upsetting Sliding Test device (WHUST), for each geometric zone type and for the 3 service lives (new, mid-life and end-of-life). The final stages are the determination of indicators of friction I_F , and the observation and analysis of the traces resulting from contact between the contactors and the specimen.

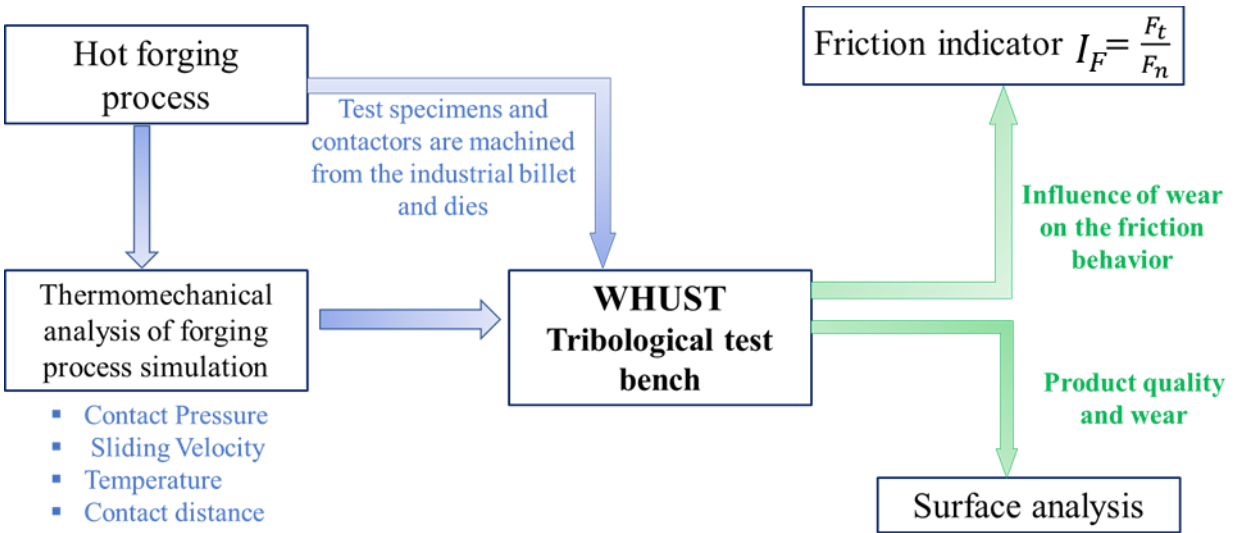


Figure 59: The methodology used to replicate the contact conditions on the WHUST test bench.

The WHUST platform is a test device that is used to replicate the contact conditions of industrial hot forming processes in order to determine and identify constitutive friction laws (Dubois *et al.*, 2015). The WHUST is composed of a contactor representing the tool and a specimen with a cylindrical geometry machined from billet material. The contactor can be heated up to 200°C using a heating cartridge inserted into the core of the material; the specimen can be induction-heated to 1300°C (Figure 60). Contactors with standard geometries (for example: cylindrical geometry) or with unconventional geometries (geometries from industrial tools) can be integrated into the experimental device. In our case, the contactors have non-conventional geometries, as they are extracted from three different zones (concave, convex, and flat) at different life cycle stages (0; 11,800; and 20,000 cycles) of the lower dies.

In the WHUST test, the contactor comes into contact with the specimen surface and generates plastic deformation by sliding on the specimen surface with constant penetration (*Figure 60*). Penetration is numerically determined to achieve the required contact pressure levels. Either deposit lubrication or spray lubrication using a nozzle on the contactor is possible. In our case, this will be spraying lubrication as in industrial practice. Sliding velocities can be set up to 500 mm/s and will be adjusted according to the studied test conditions. During the test, the normal force (F_n) and tangential force (F_t) are recorded. The friction coefficient evolution can be determined as a function of F_t , F_n and the contact area. The analysis of material transfers and surface damage phenomena occurring during the test involves further examination of the sliding track and tool surfaces using optical or interferometric methods.

As a first step, the contact parameters (contact pressure, sliding velocity, and contact temperature) are determined through finite element (FE) simulations of the industrial process and then replicated on the test bench. The desired contact pressure can be achieved by adjusting the tool penetration into the specimen.

Figure 60 illustrates the WHUST bench (Dubois *et al.*, 2014) and its working principle. Prior to the test, a cylindrical specimen is fixed in the support. The contactor is also fixed perpendicular to the specimen, and its position is precisely adjusted to locate the area of plastic deformation.

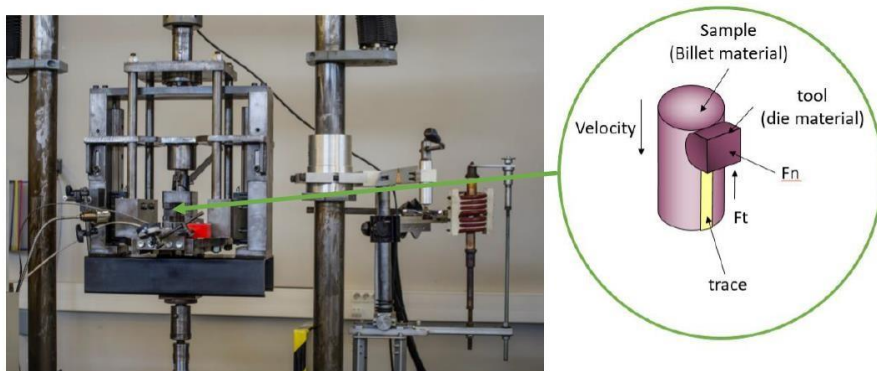


Figure 60: Photograph of the WHUST test bench and its operating principle.

4.3. Numerical Determination of the tribological conditions

To determine the tribological test parameters (contact pressures, sliding velocities and contact temperatures), a thermomechanical numerical modelling of the crankshaft forging process (*Figure 61*) is carried out. This modelling was performed by engineers at Stellantis using FORGE Nxt software. The billet is a 316×85 mm cylinder. In this first study, and with reference to chapter 1,

Chapter 4. Influence of hot forging cycles on the tribological behavior of the die

the numerical simulation is carried out with new tool geometries and therefore does not take into account tool wear and the presence of oxides. The initial billet and tool temperatures were chosen to be homogeneous and set at 1290°C and 140°C respectively. The heat exchange between the billet and the tools is set at $20,000 \text{ W/m}^2/\text{k}^{-1}$ and the coefficient of friction is chosen to be constant and equal to 0.3. Forming takes place in 0.17s. Analysis of the simulation enabled to determine the changes in contact parameters: contact pressure, sliding velocity, contact distance, and billet temperature.

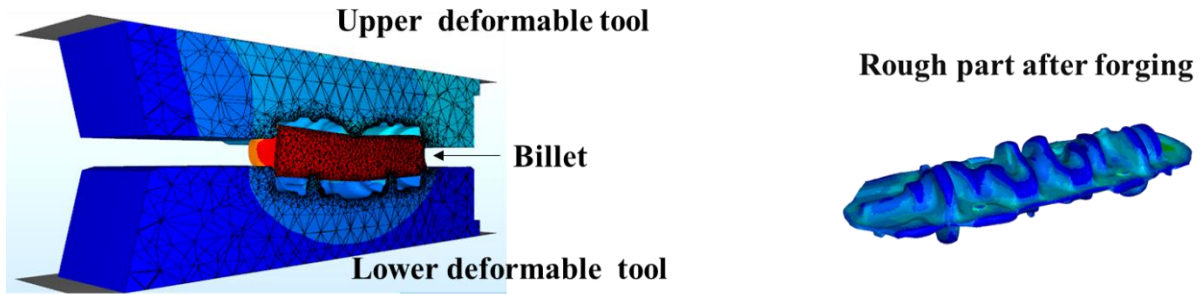


Figure 61: The numerical model used for the forging process simulation (Stellantis).

According to the evolutions of contact pressure P as a function of temperature T (Figure 62a) and sliding velocity V (Figure 62b), two triplets (P , V , T) have been retained for each type of zone geometry (concave, convex and flat): one where the contact pressure is maximum; one where the sliding velocity is maximum. The maximum values are defined based on the calculations from the sensors of the point group over time (0.17s). As the temperature during the 0.17 s of forming remains quasi constant, this parameter has not been segregated. For each zone, either concave, convex or flat, the most critical contact parameters have been selected (Table 14). According to the results of the numerical simulation, the convex zone is exposed to the maximum contact pressure and temperature, as well as lower velocities, compared to the concave and flat zones.

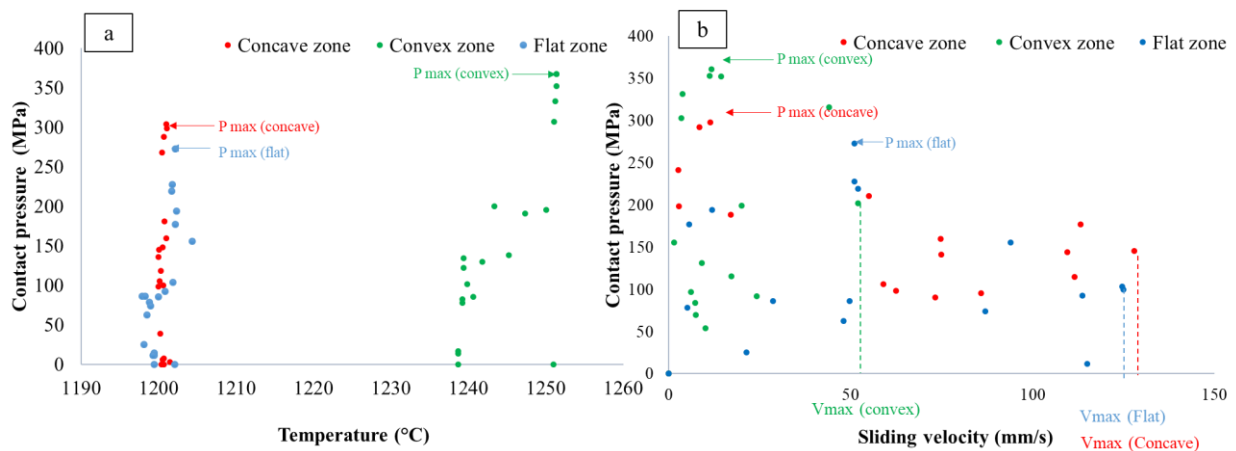


Figure 62: Contact pressure evolutions for the concave, convex, and flat zones: a) as a function of temperature, b) as a function of sliding velocity.

Table 14: Local contact conditions for each geometric zone.

Zones	(P_{\max} , V, T)	(P, V_{\max} , T)
Concave	300MPa-10mm/s-1200°C	150MPa-125mm/s-1200°C
Convex	350MPa-10mm/s-1250°C	200MPa-50mm/s-1250°C
Flat	270MPa-50mm/s-1200°C	100MPa-125mm/s-1200°C

4.4. Oxides Analysis

Before conducting the WHUST tests, it was important to compare and to analyse the oxides obtained from the billet to those obtained from the test specimens.

- **Comparison of oxides from the billet and the WHUST specimen**

During the heating of the billet or the specimen, by induction in an open-air atmosphere, oxides appear which affect the contact conditions between the billet and the tool or between the specimen and the contactor. The aim of this part is to compare the oxides from the industrial billet to those present after heating the specimens used on the WHUST. To achieve this, cylindrical specimens measuring 30 mm in diameter and 48 mm in length were machined from industrial billets of 38MnSiV5 steel grade.

SEM observations were conducted on two kinds of samples: the first one derived from the billet heated at 1290°C for 320 seconds by induction at Stellantis and cooled in open air, and the second one obtained from a WHUST specimen heated by induction at 1290°C for 320 seconds on the WHUST test bench and then cooled in open air. The oxide layers have grown in a non-uniform manner on the surface of the samples in both cases. Moreover, cracks are observed in the oxide layers (Figure 64). The average thickness of the oxide layer is determined for both samples $17 \pm 4\mu\text{m}$ for those from the billet and $15 \pm 9\mu\text{m}$ for those from the WHUST specimens. This small deviation can be explained by differences in geometry and the resulting thermal inertia.

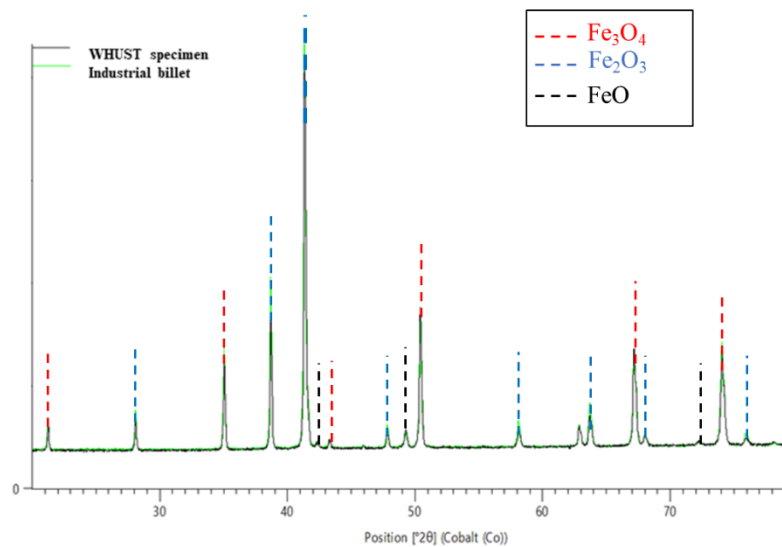


Figure 63: X-ray diffraction (XRD) analysis – Comparison WHUST specimen and Industrial billet.

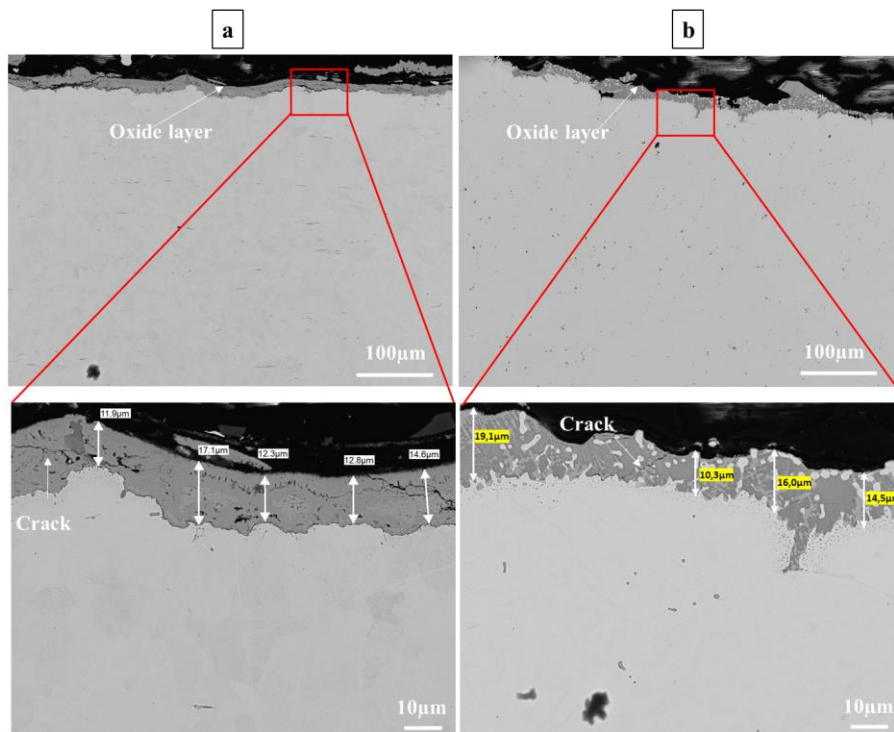


Figure 64: SEM Images: a) Sample from the billet, b) Sample from the WHUST specimen.

X-ray diffraction (XRD) analysis was carried out on oxide coming from the industrial billet heated by induction on-site in Stellantis Mulhouse and cooled in open air, and on oxide coming from the specimen heated by induction on the WHUST test bench and also cooled in open air. The aim of this analysis is to determine and compare the oxide phases formed between the billet and the WHUST specimen. XRD Analysis (Figure 63) shows that the billet and the WHUST specimen exhibit the same oxide phases: hematite (Fe_2O_3), magnetite (Fe_3O_4), and wustite (FeO) in what appears to be equivalent proportions.

- **Oxides from the lower die**

The EDS analysis on the samples extracted from the convex zone from the lower die at 11800 and 20000 cycles revealed the presence of non-uniform oxide layer in Figure 65.

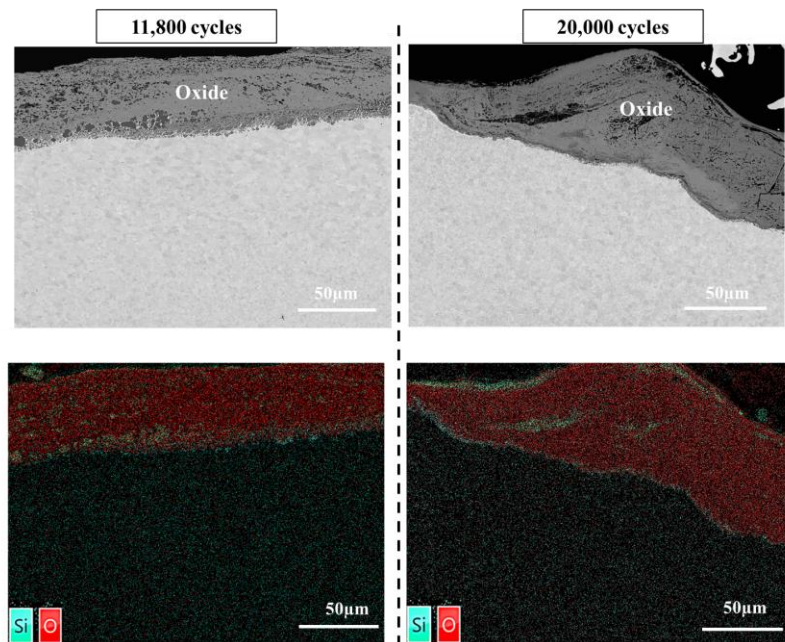


Figure 65: Energy dispersive spectroscopy (EDS) analysis on the oxides originating from the industrial billet and the WHUST specimen.

To characterize the composition of oxide layer, XRD tests were performed. Figure 66 shows that the contactors at 11,800 and 20,000 cycles exhibit the same oxide phases: magnetite (Fe_3O_4), wüstite (FeO) and silicon dioxide (SiO_2). The presence of magnetite and wüstite on the tool surface may originate from both the tool and the billet. However, it is important to note that the presence of SiO_2 comes from tool oxidation.

An increased diffraction intensity is observed for the samples at 20,000 cycles compared to those at 11,800 cycles, particularly for diffraction angles greater than 2θ of 67 degrees. This increase in diffraction intensity may be attributed to a greater quantity or density of oxide phases present on the surface of the sample subjected to a higher number of forging cycles. It seems that there is more wüstite at the end of the life and more magnetite in the mid-life. As the interface temperatures are between 650 and 900°C (Table 11), Figure 21 would suggest that the interface temperature would be higher at the end of life. This could be explained by a more significant oxide layer which would retain more heat from the billet.

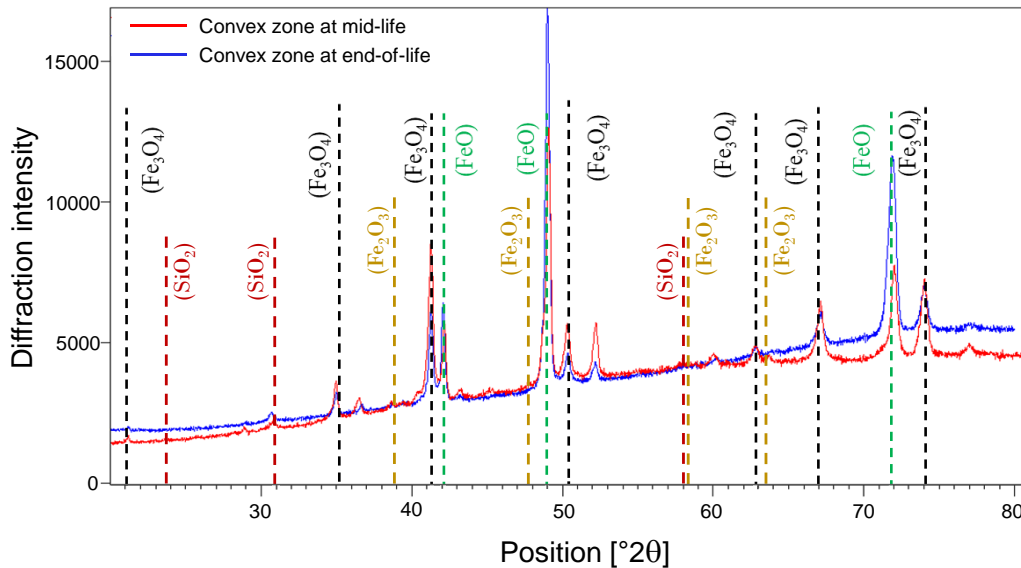


Figure 66: X-ray diffraction (XRD) analysis on the convex zone at lifecycles 11,800 and 20,000 cycles.

The mean thickness of the oxides is measured for samples extracted from concave, convex and flat zone (Table 15: The average thicknesses of the oxides for the concave, convex, and flat zones at 11,800 and 20,000 cycles.). For all three zones, the average thickness of the oxide layer at 20,000 cycles is greater than that at 11,800 cycles. The increase is 40%, 75% and 90% respectively for the convex, flat and concave zones at 20,000 cycles. However, at 11800 cycles, it was 4 to 7 times lower in the flat and concave zones than in the convex zone.

Table 15: The average thicknesses of the oxides for the concave, convex, and flat zones at 11,800 and 20,000 cycles.

	Zone					
	Convex		Flat		Concave	
Cycles	11,800	20,000	11,800	20,000	11,800	20,000
Oxide thickness (μm)	80 ±18	112±14	20±5	35±8	12±4	23±5

4.5. Tribological tests

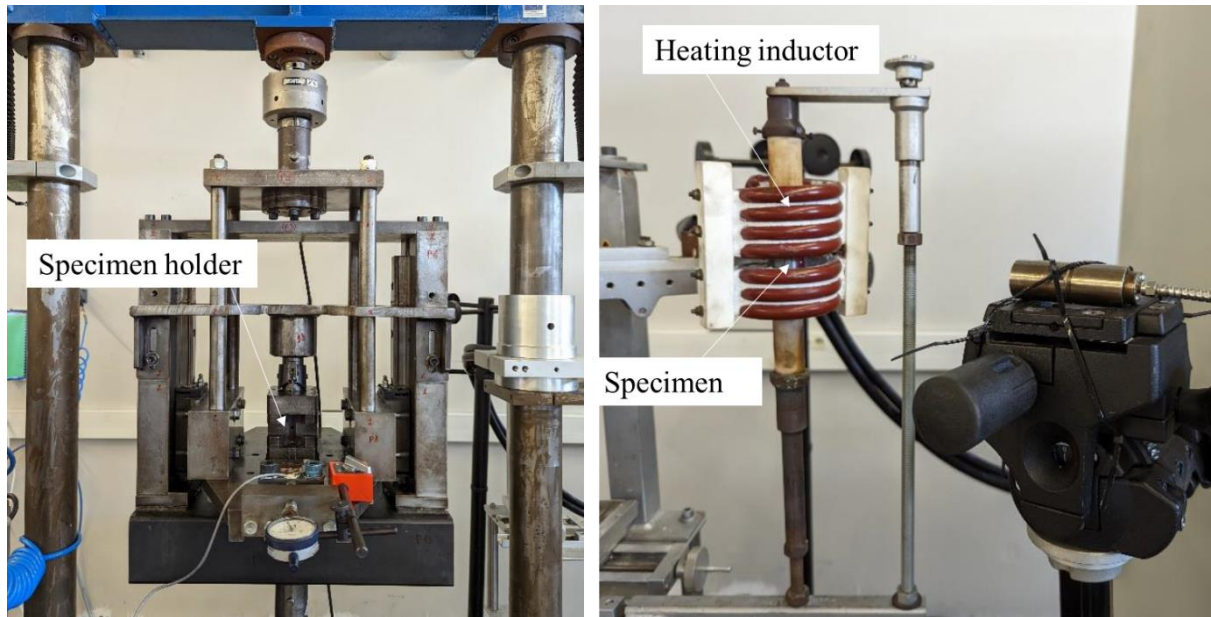


Figure 67: (a) tribometer set-up (b) heating induction system for the specimen.

In order to experimentally reproduce the numerically determined conditions presented in Table 1 for each geometric zones, tribological tests are conducted using the WHUST tribometer (Figure 67 a). In this procedure, the preheated contactor at 140°C penetrates the specimen, which is initially heated to 1290°C using the heating inductor (Figure 67 b). Then, the lubricated contactor moves along the specimen surface while maintaining constant values for penetration and sliding velocity. Lubrication is achieved by spraying the lubricant through a nozzle just before testing. For the concave and convex zones, with the geometries, the contact between the specimen and contactor is close to a cylinder-cylinder contact. Contactors are directly extracted by electro-

erosion from different zones: concave, convex, and flat (Figure 68) of hot forging dies of crankshaft at different lifecycles (0; 11,800; and 20,000 cycles).

The friction and surface contact analysis are conducted after the tests on the WHUST device for the specimens and the contactors at 0, 11800, and 20000 cycles for each geometry of contactor and each test condition (Table 14: Local contact conditions for each geometric zone). As a reminder, the test conditions correspond to the values of contact pressure, sliding velocity and temperature of the billet numerically determined during the 0.17s of forming when contact pressure and sliding velocity are maximum.

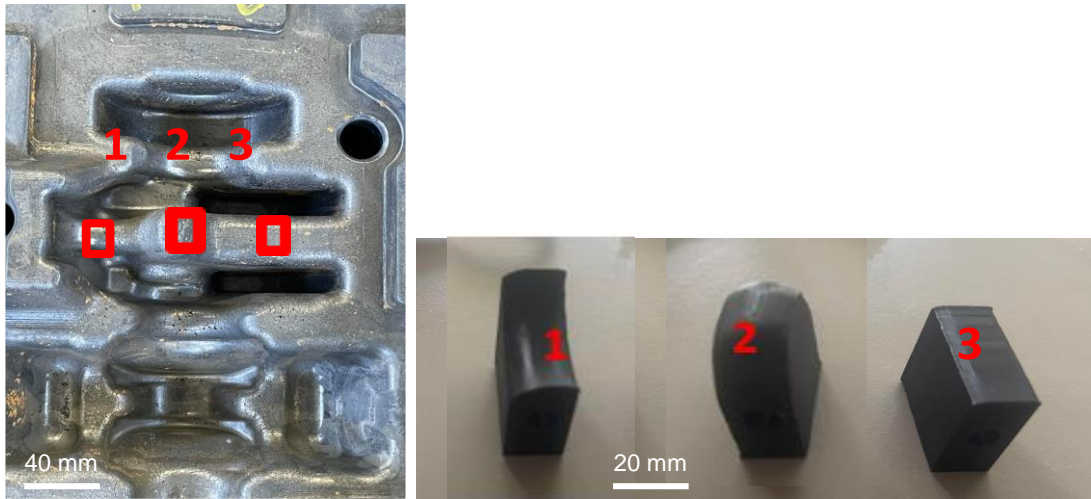


Figure 68: Example of the geometry of the contact surface: 1) concave, 2) convex, 3) flat.

4.6. Results and discussion

A specific case is first presented to highlight the adopted methodology, the nature of the collected data during and after the tests and their processing. The selected case concerns the convex contactor where the test conditions are contact pressure P_{\max} 350 MPa, relative sliding velocity 10 mm/s, and temperature of the specimen 1250 °C. The contact pressure of 350 MPa is obtained on the WHUST device with a penetration depth of 0.7 mm between the specimen and the contactor; this depth was numerically determined.

4.6.1. Friction analysis

As for all conditions, a minimum of 3 tests on the WHUST device are carried out. For each test, the evolutions of normal (F_n) and tangential (F_t) forces are recorded throughout the displacement of the contactor along the specimen (Figure 69). Determining the coefficient of friction should make it possible to assess the impact of wear on the tribological properties of the

materials in contact. In our case, the use of following friction indicator ($I_F = \frac{F_t}{F_n}$) seems preferable to friction coefficients due to the inherent complexity of the contactors geometry and the accurate determination of contact surfaces. To avoid edge effects, the friction indicators are thus determined from the ratio F_t/F_n for the region of interest which excluded the specimen chamfer and the end of

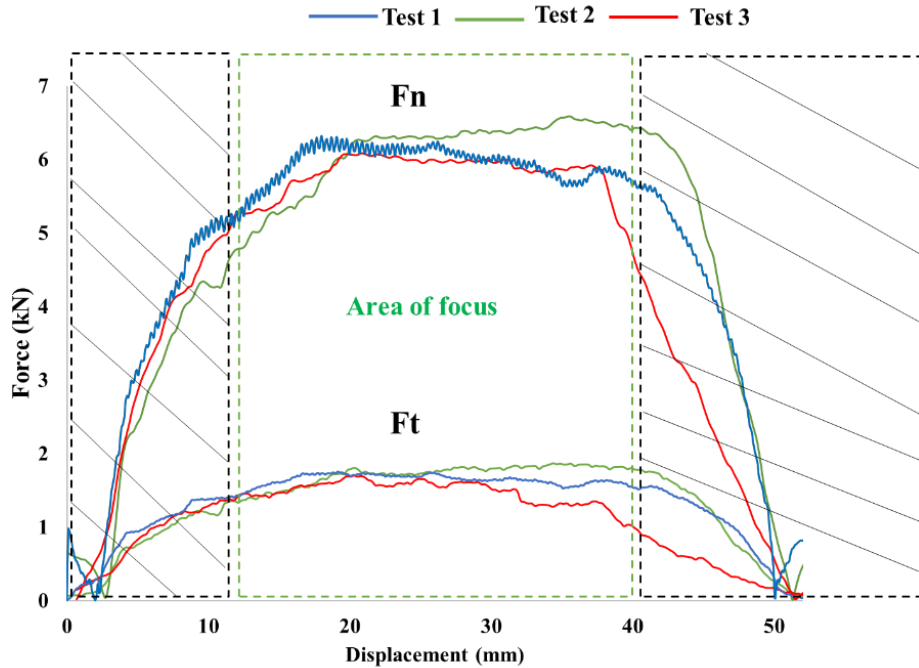


Figure 69: Example of the evolution of normal (F_n) and tangential (F_t) forces as a function of displacement (WHUST with convex contactor at 11,800 cycles.)

the specimen where the contactor exits contact zone (Figure 69). Finally, due to the low variations of this indicator along the zone of interest, an average of the friction indicator is calculated for each test, and the average of the indicator is computed for each lifecycle (Table 16).

Table 16: Evolution of the friction indicator I_F as a function of lifecycle for the convex zone at the condition (350 MPa-10 mm/s-1250 °C)

Lifecycle	Friction indicator I_F
0 cycles	0.30 (+0.03; -0.05)
11800	0.29 (+0.01; -0.03)
20000	0.28 (+0.01; -0.02)

In this case, the friction indicator varies by a maximum of 6% for the three lifecycles (0; 11,800 and 20,000 cycles). The stable friction indicator observed over the life cycles may be attributed to several factors. Firstly, the formation of oxide layers on the contacting surfaces due to high temperatures can act as a lubricant (Serebriakov, 2022), contributing to the reduction of the friction indicator. Analysis of Figure 66 had shown a greater amount of wustite for tools at the end of their life, indicating favourable sliding conditions (Behrens, 2018). Additionally, variations in geometry within the contact zones may reduce the stress distribution, consequently impacting the frictional indicator.

4.6.2. Surface contact analysis

Figure 70 shows the contact surfaces of the specimen and convex contactors after WHUST tests. The contact surface of the specimen can be divided into three regions, labelled I, II, and III. The first and third regions have been excluded from the surface analysis. The first region was excluded due to the presence of the specimen chamfer. The third region was also excluded due to partial contact between contactor and specimen at test exit and no longer has the required contact pressure.

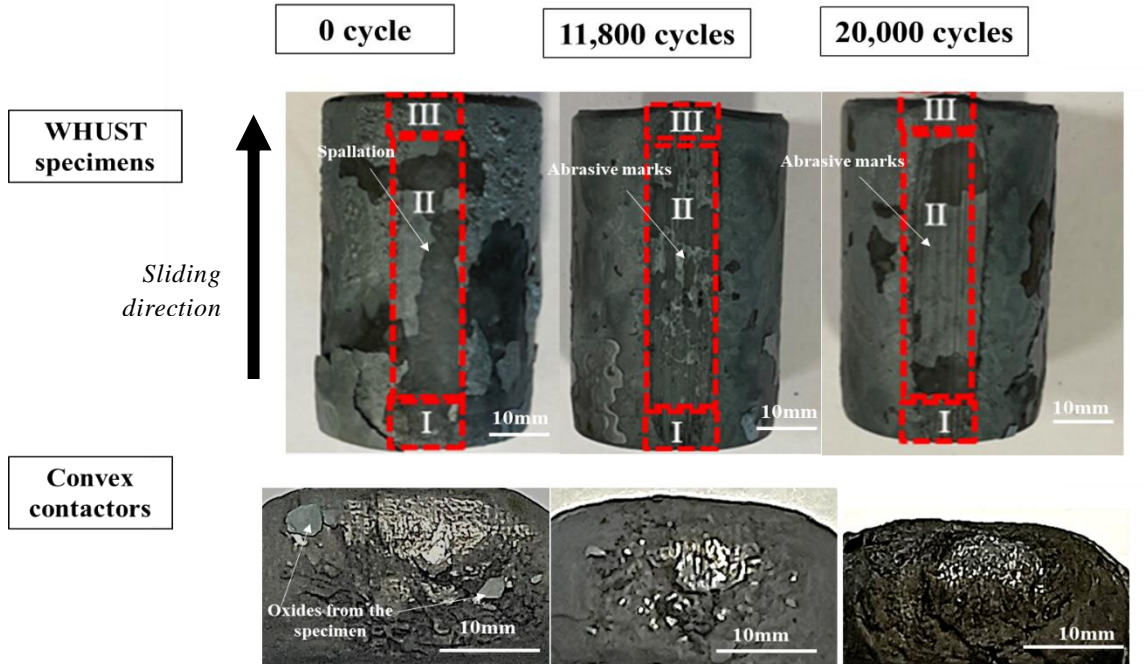


Figure 70: Images of WHUST specimens after the WHUST test and the top view of convex contactors (condition 350MPa-10mm/s-1250°C) at different lifecycles (0;11,800 and 20,000 cycles)

Spallation of oxides is observed on the specimens in contact with the contactors at 0; 11,800 and 20,000 cycles. However, contrary to the specimen at 0 cycles, which obviously shows no signs of abrasion, the specimens in contact with the contactors at 11,800 and 20,000 cycles exhibit abrasive marks. These marks follow the sliding direction and visually appear more pronounced on the specimen at 20,000 cycles. A transfer of oxides from the specimens to the surface of the contactors and reciprocally can occur, facilitated by adhesion mechanisms.

The topography of the contact trace (region II) on the specimens is analyzed using focus variation technique (Alicona Infinite Focus SL). In Figure 71, the profilometry of the trace of the specimens in contact with contactors at 0; 11,800 and 20,000 cycles are shown. An increase in surface roughness as a function of the lifecycle is observed, with the presence of abrasion marks on the specimens in contact with the contactors at 11,800 and 20,000 cycles.

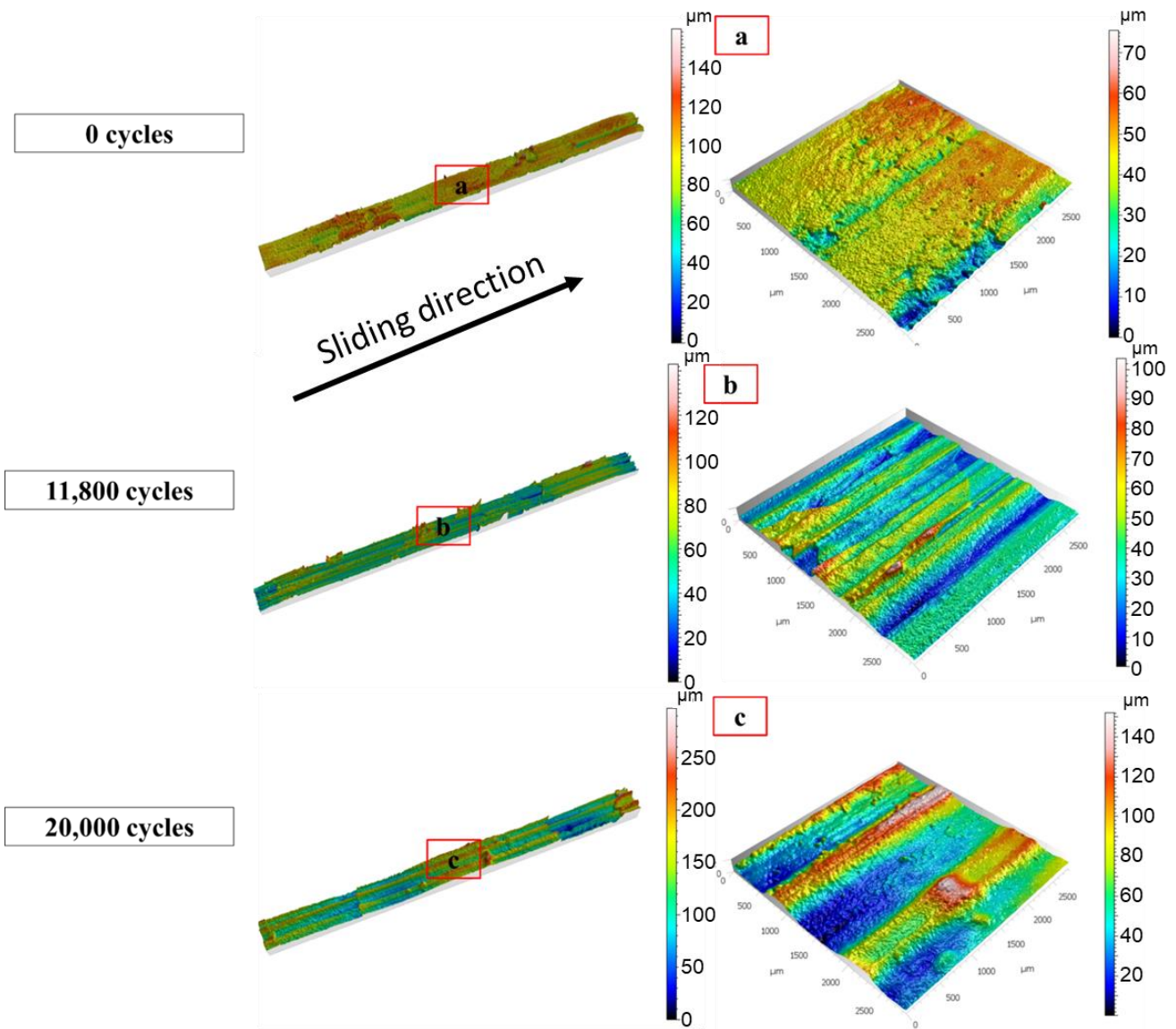


Figure 71: Topography of convex contactors at the condition (350 MPa-10 mm/s-1250 °C) and at different lifecycles (0; 11,800 and 20,000 cycles).

The results of the roughness parameters (S_a , S_v and S_p) for WHUST specimens in contact with the three contactors at different lifecycle stages are presented Figure 72 and Figure 73. The topography of the specimens becomes increasingly rough with the progression of the lifecycle. This increase in roughness is due to the contact process, during which the worn tools leave abrasive tracks on the specimens. Compared to Figure 39 (roughness of industrial tools over their lifetime), the roughness of contactors shows a similar evolution.

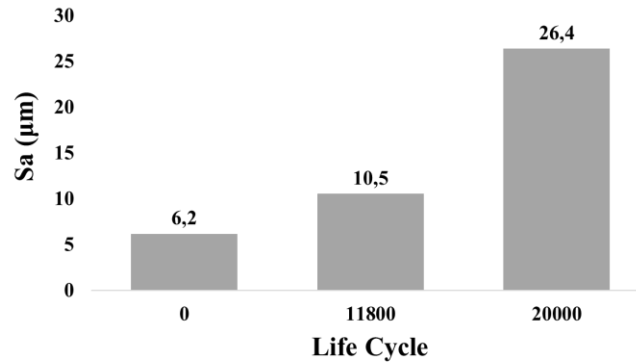


Figure 72: The evolutions of S_a (Arithmetical mean height) parameter as a function of the die life cycle of convex contactors at the condition: 350 MPa-10 mm/s-1250 °C.

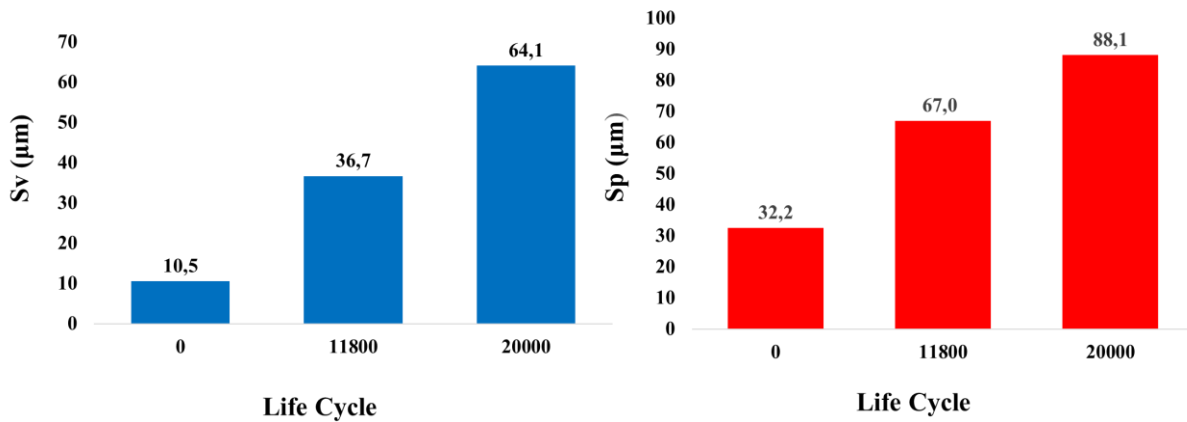


Figure 73: The evolutions of S_v (Valley Depth) and S_p (Maximum peak Height) parameters as a function of the die's life cycle of convex contactors at the condition (350MPa - 10mm/s-1250°C)

4.6.3. Summary of friction results

The friction indicator is calculated for all tests and the averages are determined for each lifecycle (Table 17)

Table 17: Evolution of the friction indicator as a function of lifecycle for each condition considered (first condition Pmax, second condition Vmax) (Table 1).

		ZONE					
		CONVEX		CONCAVE		FLAT	
Test Conditions		350 MPa	200 MPa	300 MPa	150 MPa	270 MPa	100 MPa
		10 mm/s	50 mm/s	10 mm/s	125 mm/s	50 mm/s	125 mm/s
		1250 °C	1250 °C	1200 °C	1200 °C	1200 °C	1200 °C
CYCLE	0	0.30 (+0.03;-0.05)	0.24 (+0.02;-0.02)	0.32 (+0.03;-0.03)	0.26 (+0.02;-0.03)	0.61 (+0.09;-0.11)	0.63 (+0.09;-0.08)
	11800	0.29 (+0.01;-0.03)	0.24 (+0.02;-0.02)	0.27 (+0.04;-0.02)	0.25 (+0.01;-0.02)	0.59 (+0.05;-0.07)	0.54 (+0.06;-0.11)
	20000	0.28 (+0.01;-0.02)	0.24 (+0.01;-0.005)	0.28 (+0.01;-0.01)	0.25 (+0.03;-0.01)	0.45 (+0.05;-0.03)	0.43 (+0.02;-0.02)

Even if the test conditions are different for each type of the contactor geometries and cannot be directly compared, (Table 17) shows, however, different tribological behaviors between the flat contactor and the concave and convex contactors. For convex and concave contactors, friction indicator values, range from 0.24 to 0.32 for all cycles studied, with a ratio of 7.5% to 20% greater when contact pressure is higher and sliding velocity is lower. For the flat contactor, ratio values range from 0.43 to 0.63.

For the tests conducted with convex and concave contactors, the friction indicator I_F does not vary significantly with the lifecycle of the different contactors derived from tools subjected to varying numbers of cycles (0, 11800, and 20000 cycles). For the lowest contact pressures and highest velocities, I_F is stable around 0.24 for the convex geometry and 0.25 for the concave geometry, respectively. For the highest pressures and lowest velocities, the difference between a new contactor and one after 20,000 cycles is 6.5% and 15.5% respectively for convex and concave contactors. For flat geometry contactor, friction indicator decreases significantly with the lifecycle of the contactors. Indeed, while the friction indicator deviation between cycle 0 and 11800 is

between 3% and 11%, it rises to between 25% and over 30% at cycle 20000, depending on the studied test conditions. The friction indicator values for the tests with flat contactors appear then to be approximately twice as high as those for tests with convex and concave contactors. A higher friction indicator with a flat contactor may be explained by the fact that with an initially larger contact area, the contactor promotes greater material removal. This leads to a significant increase in shear force compared with concave and convex contactors, where the contact area is smaller.

A stabilization or decrease in the friction indicator is observed during tests conducted with contactors of various geometries and lifecycles. Several factors can influence this indicator, including the presence of oxides on the surfaces of worn tools and geometry changes due to the contactors wear. Oxides generally function as solid lubrication agents by forming a protective layer between the contacting surfaces. This oxide layer reduces direct contact between the test specimen and the contactors (Serebriakov, 2022), thereby stabilizing or decreasing the friction indicator (the part of the oxidized surface acting as an otherwise lubricated surface). Additionally, oxides can function as fillers, filling surface roughness and reducing contact points, which also leads to a reduction in friction (here, the contact surface is enlarged). The changes in geometry due to tool wear can also significantly impact the friction indicator. These changes lead to variations in surface topography and the contact area, thereby modifying the contact surface between the test specimen and the contactor. Furthermore, variations in tool geometry can influence the stability of lubricant film at the interface, locally affecting tribology.

4.6.4. Summary of topography results

The topography of the contact trace (region II) on the specimens at different conditions is analysed. Abrasion marks are present on the WHUST specimens in contact with the contactor after 11,800 and 20,000 cycles, as illustrated in the previously provided example. Table 18 presents the evolution of roughness parameters as a function of the life cycle for each condition. The topography of the specimens becomes progressively rougher as their lifecycle advances. This increase in roughness is due to the contact process, where the worn tools leave abrasive marks on the specimens.

Table 18: The evolutions of Sa, Sp and Sv parameters as a function of the die life cycle of all conditions.

	Condition	Lifecycle	Sa	Sp	Sv
	WHUST specimens	Flat 100MPa-125mm/s-1200°C	0	6,4	38,7
11800			12,4	50,0	45,3
20000			15,1	66,3	53,3
Flat 270MPa-50mm/s-1200°C		0	4,0	16,2	25,8
		11800	11,4	64,7	40,6
		20000	12,7	69,7	45,91
Concave 150MPa-125mm/s-1200°C		0	12,8	60,5	41,6
		11800	16,4	64,1	43,7
		20000	20,0	79,9	69,8
Concave 300MPa-10mm/s-1200°C		0	5,3	25,3	32,4
		11800	6,9	78,9	58,9
		20000	19,3	93,4	65,9
Convex 200MPa-50mm/s-1250°C		0	11,8	34,3	38,3
		11800	21,9	99,4	43,6
		20000	32,6	133,7	83,7
Convex 350MPa-10mm/s-1250°C		0	6,2	32,2	10,5
		11800	10,5	67,0	36,7
		20000	26,4	88,1	64,1
WHUST contactors	Flat	0	1,31	34,8	7,6
		11800	7,2	52,2	44,1
		20000	8,71	39,1	60,7
	Concave	0	2,1	21,6	15,6
		11800	13,2	49,5	59,3
		20000	18,5	76,6	95,4
	Convex	0	3,5	35,8	28,5
		11800	12,3	54,7	73,9
		20000	12,9	71,5	84,3

4.7. Influence of oxides and geometry changes on contact conditions

The previous analyses conducted on the different concave, convex, and flat zones at various lifecycles (0, 11,800, and 20,000 cycles) revealed that, in addition to structural modifications (decrease in hardness for all zones as a function of lifecycles, microstructural transformations, and

decrease in Young's modulus (Chapter 3), there was also the existence of an oxide layer on the surfaces of the worn tools. Furthermore, the billet heated to 1290 °C also develops oxide on its surface. The oxides present at the workpiece/tool interface may influence forging conditions, affecting parameters such as contact pressure, material flow, and thermal conditions at the interface (Serebriakov, 2020). Consequently, the geometry of the tool can be impacted not only by wear phenomena but also by the accumulation of oxides on the surface of the tool and by the incrustation of oxide from the billet.

To analyse and understand the impact and role of oxides on thermomechanical contact conditions, a numerical approach based on an academic case was chosen. A 3D finite element model using ABAQUS/Explicit software is developed for the 3 life states of the tool. Numerical simulations are carried out using convex tools geometries with 3 different radii 8 mm, 9 mm and 10 mm (Figure 74a) to simulate a presumed state of wear. The tool with an 8 mm radius is considered to be new; the tool with a 10 mm radius is considered to be the most worn tool. This academic case comprises two distinct stages. Initially, the tool is pushed into a part until it achieves a penetration depth of 400 µm to obtain a representative contact pressure between 150 and 300 MPa. Then, once the penetration phase is complete, the tool switches to a sliding motion along the surface of the part, maintaining a constant velocity of 50 mm/s (Figure 74b). This velocity is an average velocity encountered on the crankshaft forging process. The part is made of the same material as the billet 38MnSiV5; its initial temperature is 1250 °C and a 40 µm oxide layer is modelled on the surface. The tool is considered nitrided and is made of X38CrMoV5. Its initial temperature is 140 °C. It has a 50 µm oxide layer. The mechanical and thermal properties of the oxides (Table 19) analysed through microscopy and DRX (thickness and nature) are implemented in the numerical model using the works developed by I. Serebriakov, 2022. The flowstress curves of the oxides have been extracted from the work of Behrens (Behrens, 2017 and 2018). With a contact temperature close to 700°C, the oxide will be composed of 95% wüstite, 4% magnetite and 1% haematite (Table 21). Tool wear is taken into account through three parameters: Young's modulus evolution, geometry changes and the presence of oxide. Throughout the simulation, parameters including contact pressure and temperature are continuously monitored and recorded for both the tool and the part.

The nitrided tool is represented in 2 distinct parts: on core and on surface layer with a nitrided depth of 160 µm. The elastic modulus of the tool core is set at 204 GPa, while the nitrided surface layer possesses an elastic modulus of 230 GPa. These values align with those obtained from nano indentation tests, ensuring consistency between the simulation model and experimental data. The thermal exchange coefficient is set at 20000 W/m²/°C and the friction coefficient at 0.3 (Boualem et al., 2023).

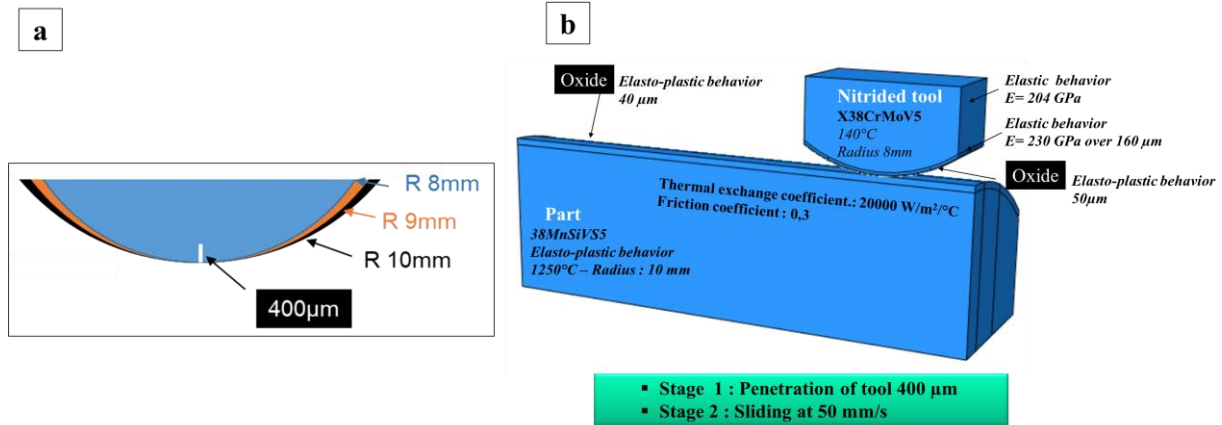


Figure 74: a) Tool radii (new tool: 8mm, mid-life: 9mm; end of life: 10mm, b) Primary input parameters for numerical simulation.

Table 19: Mechanical and thermal properties of the oxides and carbon steel (Angelo *et al.*,2016).

Material	k (W/m*K)	ρ (kg/ m ³)	Cp (J/Kg*K)	Hardness (GPa)	Elastic modulus (GPa)
FeO	3.2	7750	725	5.5 ± 1.1	125.0 ± 10.3
Fe ₃ O ₄	1.5	5600	800	6.5 ± 0.9	159 ± 4.1
Fe ₂ O ₃	1.2	4900	980	12.0 ± 2.5	220 ± 14.8
Carbon steel	35.5	7850	669		

4.7.1. The influence of oxides on thermal and mechanical contact

a) Thermal analysis

The thermal results for the part and the tool (radius 8 mm) from numerical simulations, with and without oxides, are firstly presented (Figure 75). The surface temperature analysis underscores the significant influence of oxide presence on the thermal behavior of both the tool and the part. In the absence of the oxide layer, the part exhibited a minimal temperature of 1000 °C, while the tool maintained a minimum temperature of 600 °C. Conversely, the introduction of the oxide layer led to a notable reduction in the temperatures, with the minimum temperatures recorded for the part and tool decreasing to 760 °C and 400 °C, respectively (difference of 240 °C in the part and 200 °C in the tool). It is also notable that the thermal distribution along the path of the tool on the billet without an oxide layer is more homogenous than the distribution of the temperature in the part with oxide layer. The depth of the part thermally impacted is much greater when oxide is absent (a few millimetres versus a few hundred microns). Because of its thermal properties (Table 19) oxide acts as a thermal barrier.

The part subjected to the presence of the oxide layer exhibited higher material flow at the end of tool traversal on the billet, registering a displacement of 720 μm, as opposed to the 420 μm observed in the simulation without oxide layer. As the oxide acts as a thermal barrier, the part retains its heat in its core and on its surface and remains hotter and therefore more ductile. By acting thermally in this way, the oxide has a strong influence on material flow.

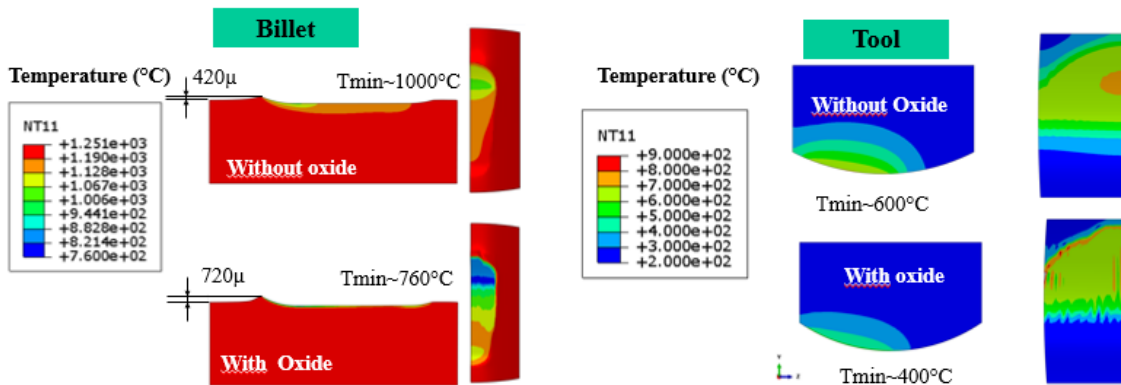


Figure 75: Numerical results of the surface temperature for the billet and the tool, with and without oxides.

b) Mechanical analysis

The contact pressure results (Figure 76) show that the presence of an oxide layer has significant effects on the contact pressure experienced by the part and the tool. The presence of an oxide layer reduced the contact pressure encountered by the part by 100 MPa (from 250 MPa to 150 MPa) representing a 40% reduction. On the tool side, the results were similar, with a drop in contact pressure of 90 MPa from 250 MPa to 160 MPa, representing a 36% reduction. The presence of an oxide layer modifies the distribution of contact pressures on both the part and the tool during hot forging, promoting a more uniform distribution and reducing stress concentration points. Conversely, in the absence of oxide, contact pressures may be more localized, leading to higher stress zones on the surface of both the part and the tool.

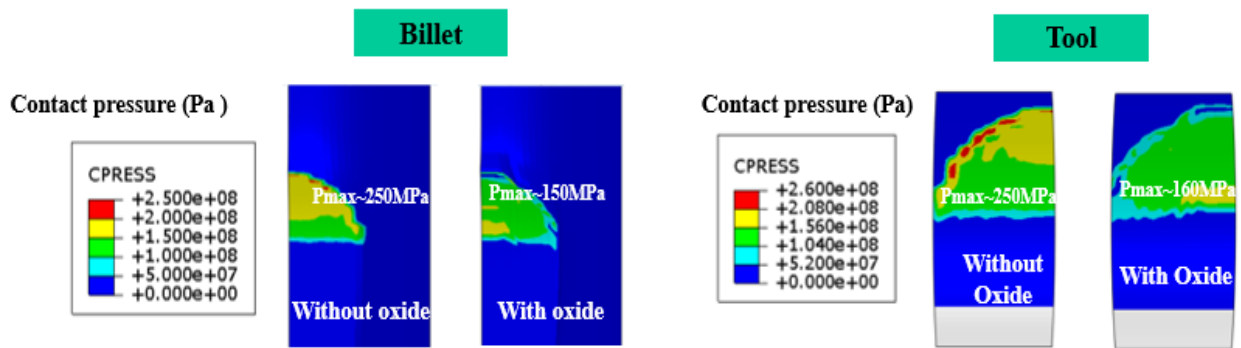


Figure 76: Numerical results of the contact pressure experienced by the billet and the tool: (a) with oxides, (b) without oxides.

4.7.2. The influence of the geometry—on thermal and mechanical contact

• a) Thermal analysis

The numerical results of the temperature for the surface contact of the parts in contact with three different tool geometries (radius 8, 9, and 10 mm) representing the three different stages of tool life (new, mid-life, and end-of-life) are presented (Figure 77). The analysis of the contact temperature at the part surface shows that the change in tool geometry influences the maximum temperature of the tool surface and its distribution. With a new tool (radius 8 mm), the maximum temperature of the part is close to 1150 °C, while the maximum temperature of the part in contact with an end-of-life tool (larger radius 10 mm) is around 1100 °C.

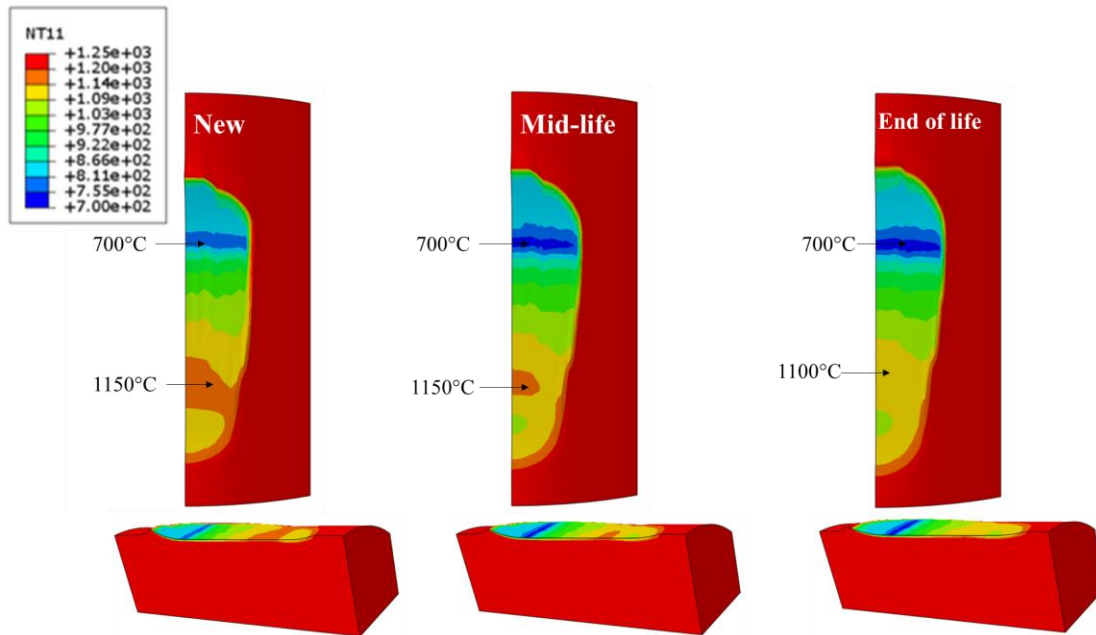


Figure 77: The numerical results of the temperature experienced by the billet in contact with three different tool geometries (radius 8, 9, and 10 mm) representing three different stages of tool life.

b) Mechanical analysis

Figure 78 presents numerical results for the contact pressure of the parts in contact with the 3 tools. The numerical results show that there is also an influence of geometry changes on the contact pressure due to wear (in this case, with low-pressure range, a difference of 40 MPa (25%) between the new tool and the tool at the end of life. There is an increase in contact area as tool life increases, linked to changes in tool contact radii. Naturally, a larger tool radius leads to a larger contact surface area. This expanded contact surface observed with worn tools allows for a more even distribution of contact pressure and eases billet penetration, requiring less pressure compared to a new tool.

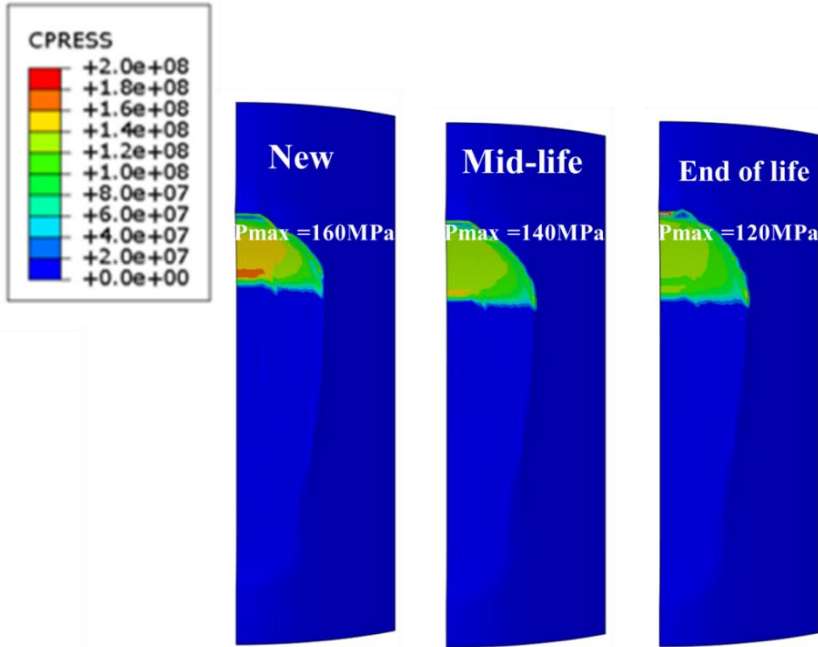


Figure 78: The numerical results of the contact pressure experienced by in contact with three different nitrided tool geometries (radius 8, 9, and 10 mm) representing three different stages of tool life (new, mid-life, and end-of-life).

4.8. Numerical analysis of the influence of geometric variations on contact pressure: Approach with the assembly of real geometries

With the objective of studying the effect of geometric variations on contact pressure for all geometries (concave, convex and flat), a 2D plane strain modelling using ABAQUS is conducted (Figure 79). The three zones (concave, convex, and flat) have been combined together to build a tool representing a portion of the industrial hot forging die (Figure 80). The simulation parameters in terms of material, friction and heat exchange are similar to those described in section 4.6. The dimensions for the different contact zones were determined at different lifecycles. A 3D scanning process was firstly undertaken to capture the geometries of the concave, convex, and flat contactors at different lifecycles. However, the complex topography and geometry of the contact surfaces posed challenges for precise scanning. For this reason, an average radius for the convex and concave tools was finally determined to capture these geometries (Table 20).

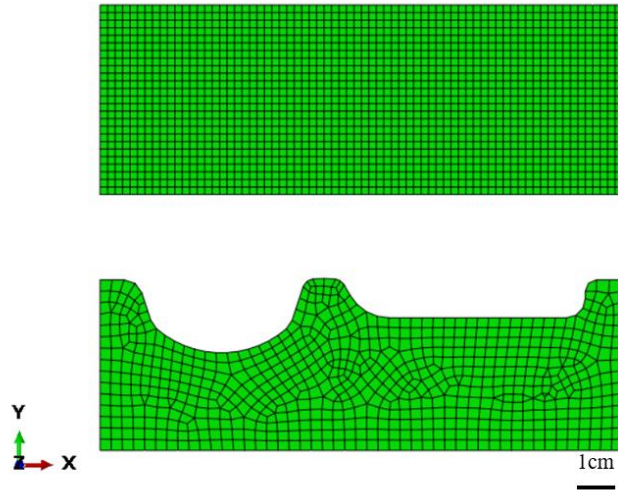


Figure 79: The 2D model of the numerical simulation using ABAQUS.

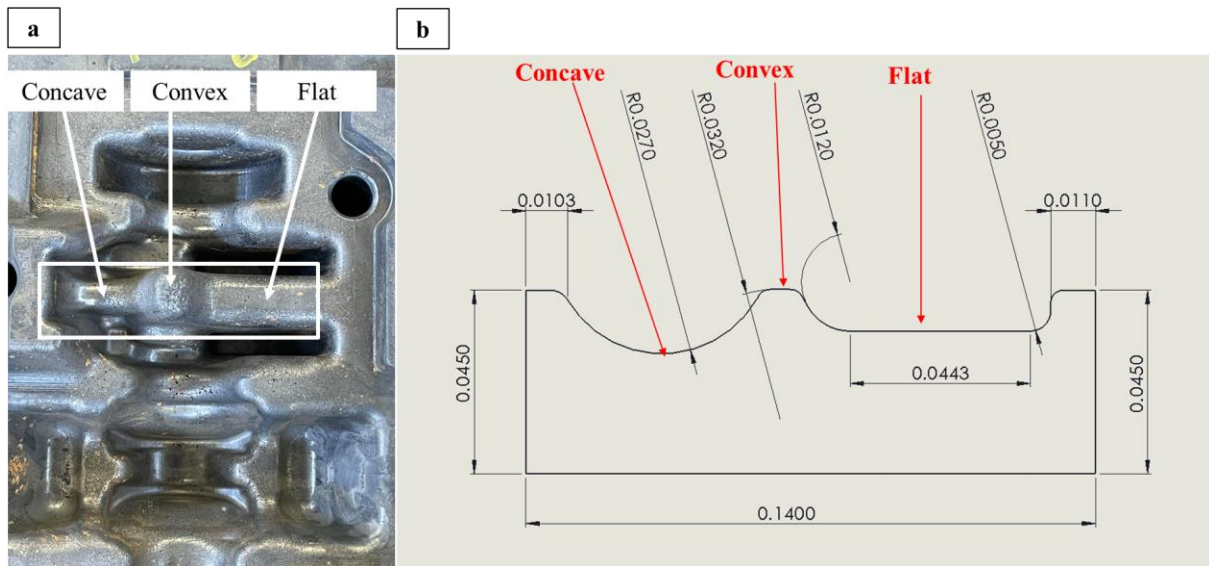


Figure 80: a) Three zones: convex, concave, and flat on the surface of the hot forging die, b) schematic of the tool geometry showing the assembly of the three zones.

Table 20: The average radii determined for the concave and convex zones at different lifecycles.

Cycles	R (mm)	
	Convex	Concave
0	21	22
11,800	32	27
20,000	35	28

Figure 81 illustrates the changes in contact pressure across different positions on the surface of concave, convex, and flat zones of new, mid-life, and end-of-life tools for initial tightening. The contact pressure required for the new tool to shape the billet is higher than the worn tools at 11800 and 20000 cycles with a difference of approximately 25% in maximum contact pressure between a new tool and an end-of-life tool for all zones. We also note a decrease in mean contact pressure of approximately 30% for the flat zone between the new and the end-of-life tool, 23% for the convex zone, and 10% for the concave zone (Figure 82).

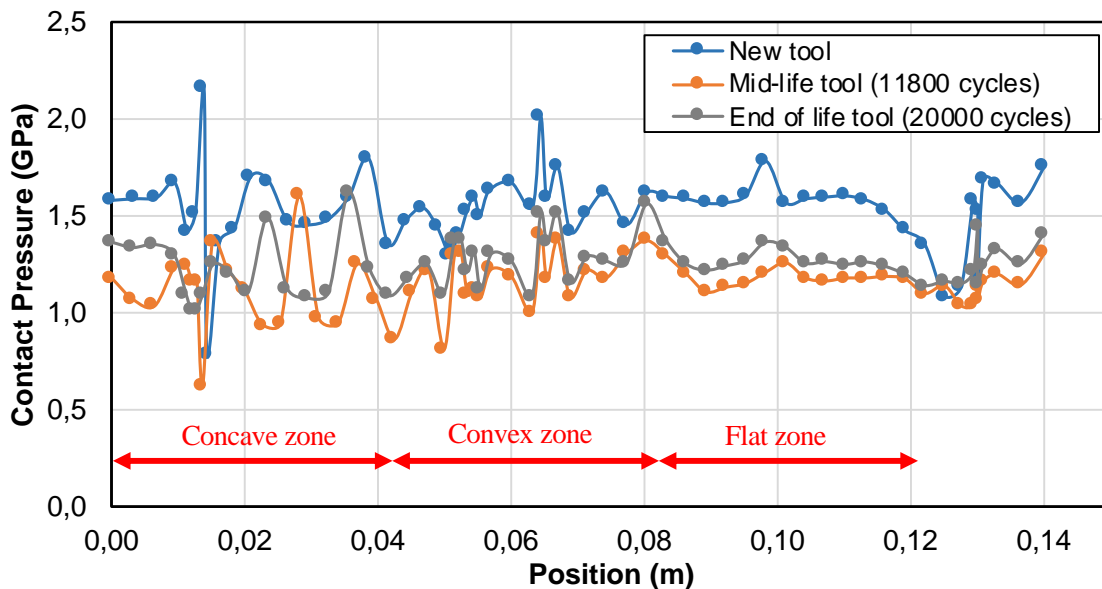


Figure 81: Evolution of contact pressure versus position for the 3 die zones (concave, convex, and flat) at different lifecycle stages for initial tightening.

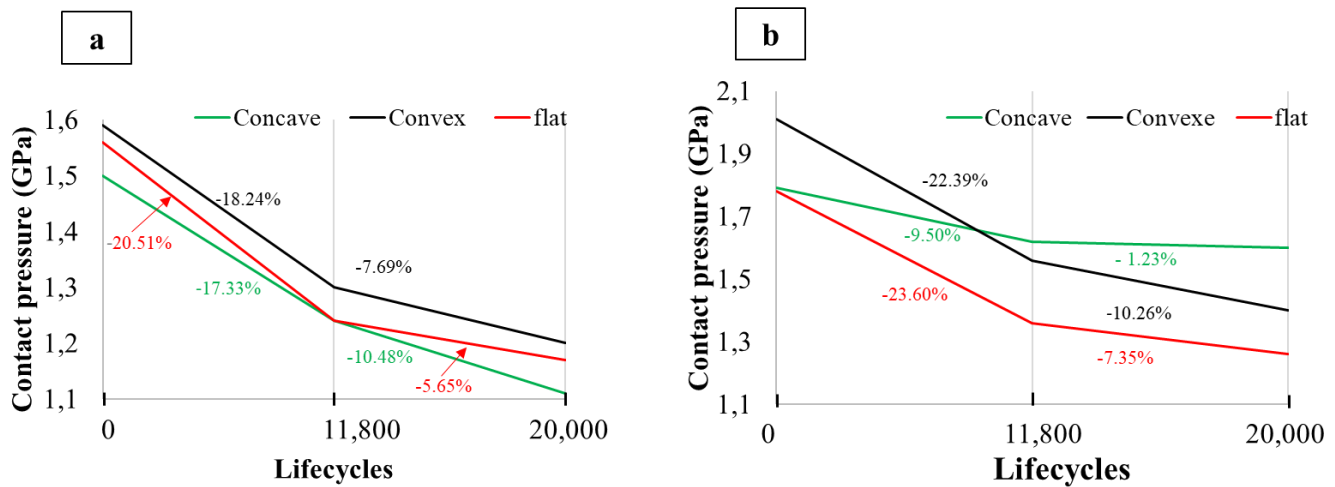


Figure 82: a) Mean contact pressure, b) Maximum contact pressure.

Figure 83 shows that the volume to be filled is greater when the zones are worn (presence of additional red zones for the two worn steps). Contact pressures will then logically be higher with new tools, as the material will be more quickly in contact with the tool.

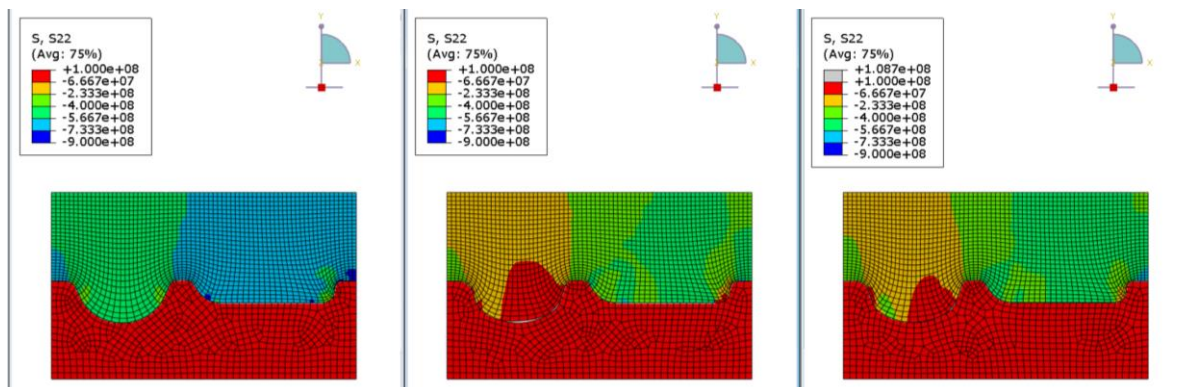


Figure 83: Results of the 2D model of the numerical simulation using ABAQUS.

To complete this work, it is important to mention the works of Davoudi et al. (Davoudi, 2021) which studied the geometric parameters affecting the wear of hot forging dies (with no oxides). In particular, they carried out a numerical study of the geometrical effects of the angle of inclination of the contact surface and the radius of the fillet between 6 and 10 mm. A 2D finite element model was implemented in ABAQUS with a velocity field distribution over the die surface and considering the effect of contact temperature and contact pressure on the wear coefficient to obtain the final wear depth. It was shown that increasing the angle of inclination of the surface from 0° to 45° generally moderates the level of wear. A critical value of 30° was observed; the wear depth increases from 0° to 30° and then decreases in the same proportion from 30° to 45° .

While concave, convex and flat geometries are important for the tribology of the forming process, changes in surface angle over time also have a significant effect on die wear.

Finally, Solgi et al. in their work on ‘heat checking’ (Solgi, 2023), which occurs as a result of thermal fatigue, showed that this phenomenon was one of the main mechanisms for reducing the life of dies that undergo sequential temperature cycles. According to these authors, the type of die design can affect the die's resistance to "heat checking" by introducing tensile stresses at sharp and angular edges. To avoid this thermal fatigue phenomenon, controlling heat transfer on the die should significantly improve thermal fatigue life. Determining the appropriate cooling location when possible, will help ensure efficient heat transfer, reduce the occurrence of surface thermal microcracking and extend tool life.

4.9. Conclusion

To study the influence of hot forging cycles on the tribological behavior of hot forging tools, a combined numerical and experimental approach is used. First, a thermomechanical analysis of the numerical simulation of the forging process is carried out to determine the interfacial contact conditions, such as contact pressure, sliding velocities, and contact temperatures. Two configurations have been determined for each type of geometric zone: one where the contact pressure is maximum and another where the sliding velocity is maximum. These industrial forging conditions are replicated using the WHUST test.

The results of the WHUST tests allow the determination of friction indicators as a function of the tool life cycle and provide information on the evolution of the contact surface topography throughout the tool life cycle. A stabilization or decrease of the friction indicator is observed during WHUST tests conducted with contactors of various geometries and life cycles.

The analysis of the surface state of the trace reveals the presence of abrasion marks on the WHUST specimens in contact with the worn contactors. An increase in roughness parameters is observed on the WHUST specimens and contactors as a function of the life cycle. Several factors may influence friction and surface topography, including the presence of oxides on the surfaces of worn tools and changes in geometry due to wear of the contactors.

XRD analysis reveals that the WHUST specimens exhibit different oxide phases: hematite (Fe_2O_3), magnetite (Fe_3O_4), and wustite (FeO). SEM analysis shows that the contactors at 11,800 and 20,000 cycles exhibit oxide layers. XRD analysis has identified the present phases: magnetite (Fe_3O_4), wustite (FeO), and silicon dioxide (SiO_2). These oxides appear to originate from both the forged part and the oxidation of the tool itself. The measurement of the average thickness of the oxides for samples extracted from concave, convex, and flat zones shows that the thickness of the oxide layer significantly increases with the tool's life cycle (The increase is 40%, 75%, and 90%,

respectively, for the convex, flat, and concave zones). Due to their thermal properties, oxides may act as a thermal barrier.

Numerical simulations are conducted to study the influence of oxides and changes in geometry on interfacial contact conditions. Temperature and contact pressure analyses demonstrate the role of oxides in thermal exchange and stress distribution. According to simulation results, there is a decrease of approximately 25% in billet temperature and 33% in tool temperature in the presence of oxides, along with a reduction of around 40% in contact pressure. Additionally, modifications in tool geometry due to wear result in an enlargement of the contact surface and affect contact pressures and thermal behavior. Depending on the tool geometry, there is observed a decrease in the required contact pressure to achieve the same penetration depth, with the pressure reduction reaching up to 30% in some zones.

The numerical study of the influence of tool geometry variation reveals that the tool geometry also impacts the contact temperature. According to simulation results (academic case), a 5% decrease in contact temperature is observed between a new tool and an end-of-life tool. Despite appearing modest, this reduction remains significant and illustrates that geometric changes can indeed affect thermal exchange.

In summary, oxides and geometric changes due to wear interact in complex ways to influence the tribological behavior of hot forging tools. Oxides play a dual role, acting both as thermal barriers and lubricants. However, they can also serve as crack initiation sites, as discussed in Chapter 3. Concurrently, geometric modifications resulting from wear, such as the loss of dimensions and sharp edges, increase the effective contact area and decrease contact pressures. This increase in contact area leads to a more uniform pressure distribution, reducing local stresses and potentially extending the tool life cycle.

General conclusion

This research investigates the multifaceted impacts of repeated forging cycles on hot forging tools, encompassing changes in surface condition, mechanical properties, microstructure, and geometric modifications due to the tool wear. The goal is to enhance the understanding of the wear state of these tools.

The crankshaft forging process at STELLANTIS Mulhouse has been selected for this study. The analysis of the forging process highlighted the complexity of tool geometries and the challenges encountered during crankshaft forging. The identification of failures and defects observed in tools at different stages of their lifecycle revealed predominant degradation modes such as wear, thermal fatigue, and mechanical fatigue. Worn tools also exhibited surface oxides embedded within cracks.

Key findings from the study can be summarized as follows:

- **Thermomechanical Behavior of the 38MnSiV5 steel grade**

Crankshafts are constructed from the 38MnSiV5 grade. Determining the rheological behavior of this grade is necessary to support numerical simulations of the forging process. The hot compression test is the most appropriate test for establishing the flow laws of materials in the case of hot forging. To achieve this, compression tests were conducted on the Gleeble 3500 over a temperature range of 950 °C to 1250 °C and strain rates from 0.01 s⁻¹ to 10 s⁻¹. To replicate the austenitic grain size distribution observed at the industrial scale within the laboratory, a series of thermal cycles were performed. The thermal etching technique was utilized to reveal the prior austenitic grain boundaries and determine their distribution. The experimental results confirmed the thermo-viscoelastic behavior of the material, highlighting the activation of dynamic recovery (DRV) and dynamic recrystallization (DRX) phenomena. Post-testing, the flow stress curves as a function of strain, strain rate, and temperature were corrected to account for friction between the sample and the dies, heating of the sample during deformation, and variations in strain rates.

- **Evolution of the topography of hot forging tools:**

The study reveals that surface roughness increases throughout the tool's life cycle due to complex phenomena such as wear. Different zones of the tool concave, convex, and flat undergo significant thermo-mechanical stresses, resulting in the formation of micro-defects. The convex zone, in particular, experiences higher stress concentrations and rougher surfaces due to the higher contact conditions and to its geometry. Tracking these changes throughout the process will facilitate the anticipation of wear by precisely pinpointing areas susceptible to heightened deterioration.

- **Mechanical Properties and Microstructural Changes**

Concerning the investigation of the effect of forging cycles on mechanical properties, specifically Young modulus and hardness, the evolution of these parameters throughout the lower die lifecycle was tracked using nano-indentation tests. Three distinct geometries were examined: concave, convex, and flat. The test results were then correlated with microstructural analysis findings obtained through SEM/EDS. The results have shown that a significant decrease in hardness with increasing life cycles, linked to the formation of fissures in the oxide layer and a transition from martensite to globular cementite. This transition, particularly evident in the convex and flat zones, is attributed to cyclic thermal softening. Additionally, decarburized zones and non-homogeneous oxide layers further contribute to the decline in hardness and surface roughness.

- **Friction Analysis**

Friction studied through WHUST tests and numerical simulations, provides valuable insights into the tribological behavior of hot forging tools. The analysis accounts for variations in friction indicators across different geometries and life cycles, offering a nuanced understanding of the wear state. The presence of oxides and changes in tool geometry significantly affect friction and wear behavior: oxide layers, increase in thickness with the number of forging cycles. These oxides act as thermal barriers and lubricants, influencing the friction and wear behavior of the tools. However, they also serve as crack initiation sites, contributing to surface damage over time. Wear-induced geometric modifications affect the contact conditions and overall performance of the forging tools. Numerical simulations highlight that changes in tool geometry lead to variations in contact pressure and temperature.

- **Future Implications**

The study of friction has revealed a stabilization or decrease in the friction indicator at high temperatures, which could be linked to the role of oxides as a thermal barrier and their function as a lubricant. Geometric modifications due to wear, as well as the type of lubricant used, also appear to play a significant role in this dynamic. In hot forging, Graphite lubricant proves to be a suitable lubricant the intensive burnout of the graphite film only occurs above 800°C. Below this temperature, the lubricant remains on the surface for a longer duration (Figure 84). Below this temperature, the lubricant remains on the surface for a longer duration.

General conclusion

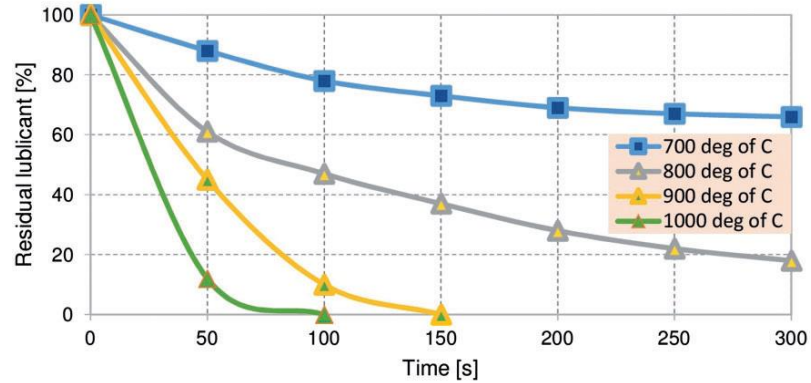


Figure 84 : Effect of surface temperature and holding time on the lubricant remaining on the surface (Sin´czak, 2007).

As perspectives, it would be judicious to consider conducting WHUST tests at lower temperatures to compare friction behavior and evaluate the effectiveness of lubricant under these conditions. WHUST tests performed without lubricant could also be contemplated to specifically study the influence of forging cycles on the system's behavior without the intervention of external lubricant.

Additional Perspectives :

- **In-depth study of oxidation phenomena:** It would be pertinent to conduct further research on the mechanisms of formation and growth of oxides on the surface of forging tools. This could include the analysis of the chemical compositions of oxides formed at different temperatures and forging conditions, as well as their impact on wear and the mechanical properties of the tools.
- **Optimization of tool materials and coatings:** Explore the use of new materials or surface treatments for the tools to reduce wear and improve durability.
- **Advanced numerical simulation:** Develop more sophisticated numerical models to simulate the behavior of forging tools under different working conditions. These models could integrate parameters such as thermal diffusion, residual stresses, and microstructure effects to provide more accurate predictions of tool wear and degradation.
- **Analysis of alternative lubricants:** Test alternative lubricants that could offer advantages in terms of wear reduction, improved friction conditions, and minimized environmental impacts. Comparative studies could help identify more effective and sustainable lubrication solutions.
- **Long-term studies on tool reliability:** Implement long-term monitoring programs to evaluate the topography, microstructure, and geometric evolution of the tools. This would

General conclusion

also include the analysis of production data, tool failures, and maintenance conditions to identify trends and opportunities for continuous improvement.

References

1. Abachi, S., Akkök, M., & Gökler, M. (2010). "Wear analysis of hot forging dies." *Tribology International*, 467-473.
2. Alimi, A. (2016). Analyse expérimentale et numérique multi-échelle du comportement mécanique de l'acier X40CrMoV5-1 : application au matriçage à chaud. Université de Nantes (PhD Thesis).
3. Altan, T., Ngaile, G., & Shen, G. (2005). "Cold and Hot Forging: Fundamentals and Applications." ASM International.
4. Armanet, F. (1984). "Influence comparée de la plasticité des couches d'oxydes sur la résistance à l'oxydation à haute température du nickel, du chrome et de certains de leurs alliages - rôle de la vapeur d'eau.", Thèse d'état à l'Université Technologique de Compiègnes (PhD Thesis).
5. Arnaud, P. (1981). "Oxydation et décarburation des aciers pour ressorts au cours du cycle de fabrication." *Metallurgical research & Technology*, pp. 539–547. Rev. Met. Paris.
6. Barrau, O. (2004). "Étude du frottement et de l'usure d'acier à outils de travail à chaud.", Institut National Polytechnique de Toulouse, (PhD Thesis).
7. Barrau, O., Boher, C., Gras, R., & Rezai-Aria, F. (2003). Analysis of the friction and wear behaviour of hot work tool steel for forging. *Wear*, 255(7–12), 1444–1454.
8. Bayer, R. G. (2004). *Mechanical wear fundamentals and testing*. CRC Press, Revised and Expanded (2nd Edition). p. 416.
9. Behrens, B.-A., Kawalla, R., Awiszus, B., Bouguecha, A., Ullmann, M., Graf, M., Bonk, C., Chugreev, A., Wester, H., 2017. Numerical Investigation of the Oxide Scale Deformation Behaviour with Consideration of Carbon Content during Hot Forging. *Procedia Engineering* 207, 526–531. <https://doi.org/10.1016/j.proeng.2017.10.816>
10. Behrens, B. A., Chugreev, A., Awiszus, B., Graf, M., Kawalla, R., Ullmann, M. & Wester, H. (2018). Sensitivity Analysis of Oxide Scale Influence on General Carbon Steels during Hot Forging. *Metals*, 140.
11. Boualem, N., Dubar, M., Moreau, P., Dubar, L., Bristiel, L., Influence of forming cycles on the mechanical properties and tribological behaviour of hot forging tools. *14th International Conference on the Technology of Plasticity*. September 2023 (Mandelieu-La Napoule, France)
12. Chalon, J. (2016, December). *Couplages matériaux procédés pour les alliages de cuivre du transport ferroviaire*, Université de Valenciennes et du Hainaut-Cambrésis, (PhD Thesis).
13. Chander, S., & Chawla, V. (2017). Failure of hot Forging Dies –An Updated perspective. *Materials Today: Proceedings*, 4 (2), Part A, 1147–1157.
14. Chang H, Borghesani P, Smith WA, et al. (2019). Application of Surface Replication Combined with Image Analysis to Investigate Wear Evolution on Gear Teeth – A Case Study. *Wear*, 430-431: 355–368.

15. Christiansen, P., Martins, P. a. F., & Bay, N. (2016). Friction compensation in the upsetting of cylindrical test specimens. *Experimental Mechanics*, 56(7), 1271–1279.
16. Daouben, E., Dubois, A., Dubar, M., Dubar, L., Deltombe, R., Truong Dinh, N.G., Lazzarotto, L. (2008). Effects of lubricant and lubrication parameters on friction during hot steel forging. *Int. J. Mater. Form*, 1, 1223–1226.
17. da Silva, R., Tonini, S. & Van Tyne, C. (2016). Processing maps for the analysis of hot workability of microalloyed steels 38MnSiVS5 and 0.39 C1.47Mn. *Journal of Materials Science*, 51:2512-2528.
18. Davoudi, M., Nejad, A. F., Rahimian Kolor, S. S. & Petru, M. (2021). Investigation of effective geometrical parameters on wear of hot forging die, *J. of Mat. Res. and Tech.* 15(1), 5221-5231.
19. Doege, E., Nägele, H., & Schliephake, U. (1994). Aspects of wear prediction in precision Forging. Part B: *Journal of Engineering Manufacture* (pp. 111-119).
20. Dubois, A., Dubar, M., & Dubar, L. (2014). Warm and hot Upsetting sliding Test: Tribology of metal processes at High temperature. *Procedia Engineering*, 81, 1964–1969.
21. Emamverdian, A. A., Sun, Y. & Chunping, C. (2021). Deformation and wear in a H21 (3Cr2W8V) steel die during hot forging: simulation, mechanical properties, and microstructural evolution. *Journal of Materials Research and Technology*, 15, 268-277.
22. Ersen A and Güngör E. Alternative Surface Roughness Measurement Technique for Inaccessible Surfaces of Jet Engine Parts Using the Rubber Silicon Replica Method. *Metallogr Microstruct Anal* 2013; 2(5): 337–342.
23. Graf, M., & Kawalla, R. (2014). Scale development on steel during hot strip rolling. *Acciaio, La metallurgia Italiana* n.2.
24. Grobaski, T. (2004b). Preliminary Research for the Development of a Hot Forging Die Life Prediction Model. (Master's thesis, Ohio University)..
25. Gronostajski, Z., & Hawryluk, M. (2008). The main aspects of precision forging. *Archives of Civil and Mechanical Engineering*, 8(2), 39–55.
26. Gronostajski, Z., Hawryluk, M., Jakubik, J., Kaszuba, M., Misiun, G., & Sadowski, P. (2015). Solution examples of selected issues related to die forging / Przykłady rozwiązań wybranych zagadnień związanych z kuciem matrycowym. *Archives of Metallurgy and Materials*, 60(4), 2773–2782.
27. Gronostajski, Z., Hawryluk, M., Kaszuba, M., Marciniak, M., Niechajowicz, A., Polak, S., Zwierzchowski, M., Adrian, A., Mrzygłód, B., & Durak, J. (2015). The expert system supporting the assessment of the durability of forging tools. *The International Journal of Advanced Manufacturing Technology/International Journal, Advanced Manufacturing Technology*, 82(9–12), 1973–1991.
28. Gronostajski, Z., Hawryluk, M., Kaszuba, M., & Ziemia, J. (2016). Application of a measuring arm with an integrated laser scanner in the analysis of the shape changes of forging instrumentation during production. *Eksploatacja I Niezawodność*, 18(2), 194–200.

29. Gronostajski, Z., Hawryluk, M., Widomski, P., Kaszuba, M., Nowak, B., Polak, S., Rychlik, M., Ziemba, J., & Zwierzchowski, M. (2019). Selected effective methods of increasing the durability of forging tools in hot forging processes. *Procedia Manufacturing*, 27, 124–129.
30. Gronostajski, Z., Kaszuba, M., Widomski, P., Smolik, J., Ziemba, J., & Hawryluk, M. (2019). Analysis of wear mechanisms of hot forging tools protected with hybrid layers performed by nitriding and PVD coatings deposition. *Wear*, 420–421, 269–280.
31. Gronostajski, Z., Widomski, P., Kaszuba, M., Zwierzchowski, M., & Hawryluk, M. (2018). Influence of both hardfaced and nitrided layers on the durability of hot forging tools. *Surface Innovations*, 6(4–5), 301–310.
32. Hairy, P. (2023, May 22). La dégradation des éléments de moule en acier X38CrMoV5 – MetalBlog (<https://metalblog.ctif.com/2023/05/22/x38crmov5-la-degradation-des-elements-de-moules-en-acier/>).
33. Hanson, M. (2008). On Adhesion and Galling in Metal Forming. Uppsala Universitet, PhD Thesis.
34. Hubicki R, Richert M and Wiewióra M. et al. (2020). “An Experimental Study of Temperature Effect on Properties of Nitride Layers on X37CrMoV51 Tool Steel Used in Extrusion Aluminium Industry.” *Materials*, 13(10): 2311.
35. Jaber, A. (2022). "Evaporation thermique d'une goutte de sang et analyse topographique des motifs induits." Thèse de doctorat, Université Polytechnique Hauts-de-France, Valenciennes.
36. Jacq, G., & Merklen, J. L. (1994). "Procédés de traitements de surface – fiches techniques." CETIM.
37. Jean, S. (1999). Méthodologie d'exploitation mécanique et microstructurale d'un essai de fatigue thermique : application à l'étude du façonnage d'un acier pour outil de forge à chaud. Université de Toulouse, (PhD Thesis).
38. Jonas, J. J., Queleñec, X., Jiang, L., & Martin, É. (2009). The Avrami kinetics of dynamic recrystallization. *Acta Materialia*, 57(9), 2748–2756.
39. Jöström, J. (2004). "Chromium martensitic hot-work tool steels – damage, performance and microstructure.", Karlstad University, Doctoral thesis.
40. Karamiş, M. (1993). Experimental study of the abrasive wear behaviour of plasma-nitrided gearing steel. *Wear*, 161(1–2), 199–206.
41. Kim, D., Lee, H., Kim, B., & Kim, K. (2005). Estimation of die service life against plastic deformation and wear during hot forging processes. *Journal of Materials Processing Technology*, 166(3), 372–380.
42. Kimura, K., Onogi, T., & Ozaki, F. (2023a). The effects of strain rate on the effective yield strength of high-strength steel at elevated temperatures. *Journal of Structural Fire Engineering*, 15(1), 24–49.

43. Kossman, S., Chicot, D., & Iost, A. (2017). Indentation instrumentée multi-échelles appliquée à l'étude des matériaux massifs métalliques. *Matériaux & Techniques*, 105(1), 104.
44. Kumar, U., Kumar, M. A., & Ohdar, R. (2014). "Hot forging lubricants." *Int J Mech Eng Rob Res*, 155-163.
45. Lange, K., Cser, L., Geiger, M., & Kals, J. (1992). Tool life and tool quality in bulk metal forming. *CIRP Annals*, 41(2), 667–675.
46. Lei, Q., Li, Z., Wang, J., Xie, J., Chen, X., Li, S., Gao, Y., & Li, L. (2013a). Hot working behavior of a super high strength Cu–Ni–Si alloy. *Materials in Engineering*, 51, 1104–1109.
47. Liitjhering, G., & Williams, J. (2007). *Titanium. Engineering Materials And Processes*, Springer.
48. Mazurkiewicz, A., & Smolik, J. (2011). Comparative analysis of wear mechanism of different types of forging dies. *Archives of Materials Science and Engineering*, 49(1), 40–45.
49. Mebarki, N., Delagnes, D., Lamesle, P., Delmas, F., & Levaillant, C. (2004). Relationship between microstructure and mechanical properties of a 5% Cr tempered martensitic tool steel. *Materials Science and Engineering. A, Structural Materials: Properties, Microstructures and Processing*. 387–389, 171–175.
50. Medjedoub, F. (2004). Détermination des paramètres influant sur le phénomène d'endommagement par fatigue thermique des moules en fonderie sous pression d'aluminium. *École Nationale Supérieure des Mines de Paris, (PhD Thesis)*.
51. Michaud P, Delagnes D, Lamesle P, et al. (2007). "The effect of the addition of alloying elements on carbide precipitation and mechanical properties in 5% chromium martensitic steels." *Acta Materialia*, 55: 4877–4889.
52. Petzing, J. N., Coupland, J. M., & Leach, R. K. (2010). The measurement of rough surface topography using coherence scanning interferometry. *Good Practice Guide No. 116*, Loughborough University.
53. Puchi-Cabrera, E., Guérin, J., Dubar, M., Dubar, L., & Dubois, A. (2016). A novel approach for modeling the flow stress curves of austenite under transient deformation conditions. *Materials Science and Engineering. A*, 673, 660–670.
54. Puchi-Cabrera, E., Guerin, J., Dubar, M., Staia, M., Lesage, J., & Chicot, D. (2015). Constitutive description of Fe–Mn23–C0.6 steel deformed under hot-working conditions. *International Journal of Mechanical Sciences*, 99, 143–153.
55. Puchi-Cabrera, E., Guérin, J., La Barbera-Sosa, J., Álvarez-Hostos, J., Moreau, P., Dubar, M., & Dubar, L. (2019). Friction Correction of Austenite Flow Stress Curves Determined under Axisymmetric Compression Conditions. *Experimental Mechanics*, 60(4), 445–458.
56. Puchi-Cabrera, E. S., Guérin, J., Dubar, M., Staia, M. H., Lesage, J., & Chicot, D. (2014). Constitutive description for the design of hot-working operations of a 20MnCr5 steel grade. *Materials in Engineering*, 62, 255–264.

57. Puchi-Cabrera, E. S., Guérin, J., La Barbera-Sosa, J. G., Dubar, M., & Dubar, L. (2021). Effect of initial grain size on the mechanical behaviour of austenite during deformation under hot-working conditions. *Materials Science and Engineering. A*, 799, 139553.
58. Sah, J. P., Richardson, G. J., & Sellars, C. M. (1974). Grain-Size Effects during Dynamic Recrystallization of Nickel. *Metal Science*, 8(1), 325–331.
59. Salem, M. (2009). Etude de l'endommagement par fatigue thermique des moules de fonderie sous pression d'aluminium: effet de l'interaction avec l'aluminisation et l'oxydation. Université de Toulouse, (PhD Thesis).
60. Sellars C.M. & McTegart W.J. (1966). On the mechanism of hot deformation. *Acta Metallurgica*, 14(9), 1136-1138.
61. Serebriakov, I. (2020). "Tribology at high temperature: experimental and numerical analysis of interfacial behavior taking into account the influence of thermomechanical contact conditions." Université Polytechnique Hauts-de-France, Valenciennes, (PhD Thesis).
62. Singh, A. K. (1973). Factors affecting die wear. *Wear*, 271-279.
63. Smerd, R., Winkler, S., Salisbury, C., Worswick, M., Lloyd, D. J., & Finn, M. (2005). "High strain rate tensile testing of automotive aluminum alloy sheet." *International Journal of Impact Engineering*, 32(1-4), 541–560.
64. Soady, K. A., & Allwood, J. M. (2016). "Prediction of tool wear in hot forging: a review." *International Journal of Material Forming*, 9(4), 523–534.
65. Solgi, P., Chenarani, M., Eivani, A. R., Ghosh, M., Kumar, V. & Jafarian, H. R. (2023). Heat checking as a failure mechanism of dies exposed to thermal cycles: A review, *J. of Mat. Res. and Tech.* 26 865-895.
66. Sommitsch, C. (2011). "Microstructure development and mechanical properties during hot forging of a novel gamma-TiAl alloy." *Intermetallics*, 19(5), 700–707.
67. Widomski P, Kaszuba M, Dobras D, (2021). "Development of a method of increasing the wear resistance of forging dies in the aspect of tool material, thermo-chemical treatment and PVD coatings applied in a selected hot forging process." *Wear*, 477: 203828.

Appendix

Appendix 1: Data for all curves after corrections and fitting

950°C	Effective strain rate (s ⁻¹)				1050°C	Effective strain rate (s ⁻¹)			
Effective strain	0,01	0,1	1	10	Effective strain	0,01	0,1	1	10
0	50.2	67.4	69.3	126.5	0	37.8	43.9	56.4	101.6
0.005	58.4	78.0	89.0	143.3	0.005	43.5	52.0	69.5	113.5
0.01	61.7	82.4	96.9	150.0	0.01	45.8	55.4	74.7	118.0
0.015	64.2	85.6	102.7	155.1	0.015	47.5	57.9	78.5	121.3
0.02	66.3	88.4	107.5	159.3	0.02	48.9	59.9	81.7	124.0
0.025	68.1	90.7	111.6	162.8	0.025	50.0	61.7	84.4	126.3
0.03	69.6	92.8	115.2	166.0	0.03	51.1	63.3	86.8	128.3
0.035	71.1	94.7	118.4	168.8	0.035	52.0	64.7	88.9	130.1
0.04	72.4	96.5	121.3	171.3	0.04	52.8	66.0	90.8	131.7
0.045	73.6	98.1	123.9	173.7	0.045	53.5	67.2	92.5	133.2
0.05	74.7	99.6	126.3	175.8	0.05	54.2	68.3	94.2	134.6
0.055	75.8	101.0	128.5	177.8	0.055	54.8	69.3	95.6	135.8
0.06	76.8	102.3	130.5	179.6	0.06	55.4	70.3	97.0	137.0
0.065	77.7	103.6	132.4	181.4	0.065	55.9	71.2	98.3	138.1
0.07	78.6	104.8	134.2	183.0	0.07	56.3	72.0	99.5	139.2
0.075	79.4	105.9	135.9	184.5	0.075	56.7	72.9	100.7	140.2
0.08	80.2	107.0	137.4	185.9	0.08	57.1	73.6	101.8	141.1
0.085	81.0	108.0	138.9	187.3	0.085	57.4	74.4	102.8	142.0
0.09	81.7	109.0	140.2	188.5	0.09	57.7	75.0	103.7	142.9
0.095	82.4	110.0	141.5	189.7	0.095	57.9	75.7	104.7	143.7
0.1	83.0	110.9	142.8	190.9	0.1	58.1	76.3	105.5	144.4
0.105	83.7	111.8	143.9	192.0	0.105	58.3	76.9	106.4	145.2
0.11	84.3	112.6	145.0	193.0	0.11	58.4	77.5	107.1	145.9
0.115	84.8	113.5	146.0	194.0	0.115	58.5	78.1	107.9	146.6
0.12	85.4	114.2	147.0	194.9	0.12	58.6	78.6	108.6	147.3
0.125	85.9	115.0	147.9	195.8	0.125	58.6	79.1	109.3	147.9
0.13	86.5	115.8	148.8	196.6	0.13	58.6	79.6	110.0	148.5
0.135	86.9	116.5	149.6	197.4	0.135	58.6	80.0	110.6	149.1
0.14	87.4	117.2	150.4	198.2	0.14	58.6	80.5	111.2	149.7
0.145	87.9	117.8	151.2	198.9	0.145	58.5	80.9	111.8	150.2
0.15	88.3	118.5	151.9	199.6	0.15	58.4	81.3	112.3	150.8
0.155	88.7	119.1	152.6	200.3	0.155	58.3	81.7	112.8	151.3
0.16	89.1	119.7	153.2	200.9	0.16	58.2	82.0	113.4	151.8
0.165	89.5	120.3	153.9	201.5	0.165	58.0	82.4	113.8	152.2
0.17	89.8	120.9	154.5	202.1	0.17	57.8	82.7	114.3	152.7
0.175	90.2	121.4	155.0	202.7	0.175	57.6	83.0	114.8	153.2
0.18	90.5	122.0	155.6	203.2	0.18	57.4	83.3	115.2	153.6
0.185	90.8	122.5	156.1	203.7	0.185	57.2	83.5	115.6	154.0

0.19	91.1	123.0	156.6	204.2	0.19	56.9	83.8	116.0	154.4
0.195	91.3	123.4	157.0	204.7	0.195	56.7	84.0	116.3	154.8
0.2	91.6	123.9	157.5	205.2	0.2	56.4	84.2	116.7	155.2
0.205	91.8	124.3	157.9	205.6	0.205	56.1	84.4	117.0	155.6
0.21	92.0	124.7	158.3	206.0	0.21	55.8	84.6	117.3	155.9
0.215	92.2	125.1	158.7	206.4	0.215	55.5	84.7	117.6	156.3
0.22	92.4	125.5	159.1	206.8	0.22	55.2	84.8	117.9	156.6
0.225	92.5	125.8	159.4	207.2	0.225	54.9	85.0	118.2	156.9
0.23	92.6	126.1	159.8	207.5	0.23	54.6	85.0	118.4	157.2
0.235	92.8	126.5	160.1	207.9	0.235	54.3	85.1	118.7	157.5
0.24	92.9	126.7	160.4	208.2	0.24	53.9	85.2	118.9	157.8
0.245	93.0	127.0	160.7	208.5	0.245	53.6	85.2	119.1	158.0
0.25	93.0	127.3	161.0	208.8	0.25	53.3	85.2	119.2	158.3
0.255	93.1	127.5	161.3	209.1	0.255	53.0	85.2	119.4	158.5
0.26	93.1	127.7	161.5	209.4	0.26	52.7	85.1	119.6	158.7
0.265	93.1	127.9	161.8	209.6	0.265	52.4	85.1	119.7	158.9
0.27	93.2	128.1	162.0	209.9	0.27	52.1	85.0	119.8	159.1
0.275	93.1	128.3	162.2	210.1	0.275	51.8	84.9	119.9	159.3
0.28	93.1	128.4	162.5	210.4	0.28	51.5	84.8	120.0	159.5
0.285	93.1	128.6	162.7	210.6	0.285	51.2	84.6	120.1	159.6
0.29	93.1	128.7	162.9	210.8	0.29	50.9	84.4	120.1	159.8
0.295	93.0	128.8	163.1	211.0	0.295	50.7	84.2	120.2	159.9
0.3	92.9	128.9	163.3	211.2	0.3	50.4	84.0	120.2	160.0
0.305	92.9	129.0	163.4	211.4	0.305	50.2	83.8	120.2	160.1
0.31	92.8	129.0	163.6	211.6	0.31	50.0	83.5	120.2	160.2
0.315	92.7	129.0	163.8	211.8	0.315	49.7	83.3	120.2	160.3
0.32	92.6	129.1	163.9	212.0	0.32	49.5	83.0	120.2	160.3
0.325	92.5	129.1	164.1	212.2	0.325	49.4	82.6	120.2	160.4
0.33	92.3	129.1	164.2	212.3	0.33	49.2	82.3	120.1	160.4
0.335	92.2	129.0	164.4	212.5	0.335	49.0	81.9	120.1	160.4
0.34	92.1	129.0	164.5	212.6	0.34	48.9	81.6	120.0	160.4
0.345	91.9	129.0	164.6	212.8	0.345	48.7	81.2	119.9	160.4
0.35	91.8	128.9	164.8	212.9	0.35	48.6	80.8	119.9	160.4
0.355	91.6	128.8	164.9	213.0	0.355	48.4	80.4	119.8	160.4
0.36	91.5	128.7	165.0	213.2	0.36	48.3	79.9	119.7	160.3
0.365	91.3	128.7	165.1	213.3	0.365	48.2	79.5	119.6	160.3
0.37	91.1	128.5	165.2	213.4	0.37	48.1	79.1	119.4	160.2
0.375	91.0	128.4	165.3	213.5	0.375	48.1	78.6	119.3	160.1
0.38	90.8	128.3	165.4	213.6	0.38	48.0	78.1	119.2	160.0
0.385	90.6	128.2	165.5	213.8	0.385	47.9	77.7	119.0	159.9
0.39	90.5	128.0	165.6	213.9	0.39	47.9	77.2	118.9	159.8
0.395	90.3	127.9	165.7	214.0	0.395	47.8	76.8	118.7	159.7
0.4	90.1	127.7	165.7	214.0	0.4	47.8	76.3	118.6	159.6
0.405	90.0	127.5	165.8	214.1	0.405	47.7	75.8	118.4	159.5
0.41	89.8	127.3	165.9	214.2	0.41	47.7	75.4	118.3	159.3
0.415	89.6	127.1	166.0	214.3	0.415	47.7	74.9	118.1	159.2
0.42	89.5	127.0	166.0	214.4	0.42	47.6	74.5	117.9	159.0
0.425	89.3	126.8	166.1	214.5	0.425	47.6	74.1	117.8	158.9

0.43	89.1	126.6	166.2	214.6	0.43	47.6	73.6	117.6	158.7
0.435	89.0	126.3	166.2	214.6	0.435	47.6	73.2	117.4	158.5
0.44	88.8	126.1	166.3	214.7	0.44	47.6	72.8	117.2	158.4
0.445	88.7	125.9	166.3	214.8	0.445	47.6	72.4	117.1	158.2
0.45	88.5	125.7	166.4	214.8	0.45	47.6	72.1	116.9	158.0
0.455	88.4	125.5	166.5	214.9	0.455	47.6	71.7	116.7	157.8
0.46	88.3	125.2	166.5	215.0	0.46	47.6	71.4	116.6	157.7
0.465	88.1	125.0	166.6	215.0	0.465	47.6	71.1	116.4	157.5
0.47	88.0	124.8	166.6	215.1	0.47	47.6	70.8	116.2	157.3
0.475	87.9	124.6	166.6	215.1	0.475	47.6	70.5	116.1	157.1
0.48	87.8	124.3	166.7	215.2	0.48	47.6	70.3	115.9	156.9
0.485	87.6	124.1	166.7	215.2	0.485	47.6	70.0	115.7	156.8
0.49	87.5	123.9	166.8	215.3	0.49	47.6	69.8	115.6	156.6
0.495	87.4	123.6	166.8	215.3	0.495	47.6	69.6	115.4	156.4
0.5	87.3	123.4	166.8	215.4	0.5	47.6	69.4	115.3	156.3
0.505	87.2	123.2	166.9	215.4	0.505	47.6	69.2	115.1	156.1
0.51	87.1	123.0	166.9	215.5	0.51	47.6	69.1	115.0	156.0
0.515	87.1	122.7	166.9	215.5	0.515	47.6	69.0	114.9	155.8
0.52	87.0	122.5	167.0	215.5	0.52	47.6	68.8	114.7	155.7
0.525	86.9	122.3	167.0	215.6	0.525	47.7	68.7	114.6	155.5
0.53	86.8	122.1	167.0	215.6	0.53	47.7	68.6	114.5	155.4
0.535	86.8	121.9	167.1	215.6	0.535	47.7	68.6	114.4	155.3
0.54	86.7	121.7	167.1	215.7	0.54	47.7	68.5	114.3	155.1
0.545	86.7	121.5	167.1	215.7	0.545	47.7	68.4	114.2	155.0
0.55	86.6	121.3	167.1	215.7	0.55	47.7	68.4	114.1	154.9
0.555	86.6	121.1	167.2	215.8	0.555	47.7	68.4	114.0	154.8
0.56	86.5	120.9	167.2	215.8	0.56	47.7	68.3	113.9	154.7
0.565	86.5	120.7	167.2	215.8	0.565	47.7	68.3	113.8	154.6
0.57	86.5	120.5	167.2	215.9	0.57	47.7	68.3	113.7	154.5
0.575	86.4	120.4	167.2	215.9	0.575	47.7	68.3	113.7	154.5
0.58	86.4	120.2	167.3	215.9	0.58	47.7	68.3	113.6	154.4
0.585	86.4	120.0	167.3	215.9	0.585	47.7	68.3	113.5	154.3
0.59	86.3	119.9	167.3	216.0	0.59	47.8	68.3	113.5	154.3
0.595	86.3	119.7	167.3	216.0	0.595	47.8	68.3	113.4	154.2
0.6	86.3	119.6	167.3	216.0	0.6	47.8	68.3	113.4	154.2
0.605	86.3	119.4	167.3	216.0	0.605	47.8	68.4	113.3	154.1
0.61	86.3	119.3	167.4	216.0	0.61	47.8	68.4	113.3	154.1
0.615	86.3	119.2	167.4	216.1	0.615	47.8	68.4	113.3	154.1
0.62	86.3	119.1	167.4	216.1	0.62	47.8	68.4	113.2	154.0
0.625	86.3	118.9	167.4	216.1	0.625	47.8	68.4	113.2	154.0
0.63	86.3	118.8	167.4	216.1	0.63	47.8	68.5	113.2	154.0
0.635	86.3	118.7	167.4	216.1	0.635	47.8	68.5	113.1	154.0
0.64	86.3	118.6	167.4	216.2	0.64	47.8	68.5	113.1	153.9
0.645	86.3	118.5	167.4	216.2	0.645	47.8	68.5	113.1	153.9
0.65	86.3	118.4	167.5	216.2	0.65	47.8	68.5	113.1	153.9
0.655	86.3	118.3	167.5	216.2	0.655	47.8	68.6	113.1	153.9
0.66	86.3	118.3	167.5	216.2	0.66	47.8	68.6	113.0	153.9
0.665	86.3	118.2	167.5	216.2	0.665	47.8	68.6	113.0	153.9

0.67	86.3	118.1	167.5	216.2	0.67	47.8	68.6	113.0	153.9
0.675	86.3	118.1	167.5	216.3	0.675	47.8	68.6	113.0	153.9
0.68	86.3	118.0	167.5	216.3	0.68	47.8	68.7	113.0	153.9
0.685	86.3	117.9	167.5	216.3	0.685	47.8	68.7	113.0	153.9
0.69	86.3	117.9	167.5	216.3	0.69	47.8	68.7	113.0	153.9
0.695	86.4	117.8	167.5	216.3	0.695	47.8	68.7	113.0	153.9
0.7	86.4	117.8	167.5	216.3	0.7	47.8	68.7	113.0	153.9
0.705	86.4	117.8	167.5	216.3	0.705	47.8	68.8	113.0	153.9
0.71	86.4	117.7	167.5	216.4	0.71	47.8	68.8	113.0	153.9
0.715	86.4	117.7	167.5	216.4	0.715	47.9	68.8	113.0	153.9
0.72	86.4	117.7	167.5	216.4	0.72	47.9	68.8	113.0	153.9
0.725	86.4	117.6	167.6	216.4	0.725	47.9	68.8	113.0	154.0
0.73	86.5	117.6	167.6	216.4	0.73	47.9	68.8	113.0	154.0
0.735	86.5	117.6	167.6	216.4	0.735	47.9	68.9	113.0	154.0
0.74	86.5	117.6	167.6	216.4	0.74	47.9	68.9	113.0	154.0
0.745	86.5	117.6	167.6	216.4	0.745	47.9	68.9	113.0	154.0
0.75	86.5	117.6	167.6	216.4	0.75	47.9	68.9	113.0	154.0
0.755	86.5	117.6	167.6	216.5	0.755	47.9	68.9	113.0	154.0
0.76	86.5	117.6	167.6	216.5	0.76	47.9	68.9	113.0	154.0
0.765	86.6	117.6	167.6	216.5	0.765	47.9	68.9	113.0	154.0
0.77	86.6	117.6	167.6	216.5	0.77	47.9	68.9	113.0	154.0
0.775	86.6	117.6	167.6	216.5	0.775	47.9	69.0	113.0	154.0
0.78	86.6	117.6	167.6	216.5	0.78	47.9	69.0	113.0	154.1
0.785	86.6	117.6	167.6	216.5	0.785	47.9	69.0	113.0	154.1
0.79	86.6	117.6	167.6	216.5	0.79	47.9	69.0	113.0	154.1
0.795	86.6	117.6	167.6	216.5	0.795	47.9	69.0	113.0	154.1
0.8	86.7	117.6	167.6	216.6	0.8	47.9	69.0	113.0	154.1
0.805	86.7	117.6	167.6	216.6	0.805	47.9	69.0	113.0	154.1
0.81	86.7	117.6	167.6	216.6	0.81	47.9	69.0	113.0	154.1
0.815	86.7	117.6	167.6	216.6	0.815	47.9	69.0	113.0	154.1
0.82	86.7	117.6	167.6	216.6	0.82	47.9	69.1	113.1	154.1
0.825	86.7	117.7	167.6	216.6	0.825	47.9	69.1	113.1	154.1
0.83	86.7	117.7	167.6	216.6	0.83	47.9	69.1	113.1	154.1
0.835	86.7	117.7	167.6	216.6	0.835	47.9	69.1	113.1	154.1
0.84	86.8	117.7	167.6	216.6	0.84	47.9	69.1	113.1	154.1
0.845	86.8	117.7	167.6	216.6	0.845	47.9	69.1	113.1	154.1
0.85	86.8	117.8	167.6	216.7	0.85	47.9	69.1	113.1	154.1
0.855	86.8	117.8	167.5	216.7	0.855	47.9	69.1	113.1	154.1
0.86	86.8	117.8	167.5	216.7	0.86	47.9	69.1	113.1	154.2
0.865	86.8	117.8	167.5	216.7	0.865	47.9	69.1	113.1	154.2
0.87	86.8	117.8	167.5	216.7	0.87	47.9	69.1	113.1	154.2
0.875	86.8	117.9	167.5	216.7	0.875	47.9	69.1	113.1	154.2
0.88	86.8	117.9	167.5	216.7	0.88	47.9	69.2	113.1	154.2
0.885	86.9	117.9	167.5	216.7	0.885	47.9	69.2	113.1	154.2
0.89	86.9	117.9	167.5	216.7	0.89	47.9	69.2	113.1	154.2
0.895	86.9	117.9	167.5	216.7	0.895	47.9	69.2	113.1	154.2
0.9	86.9	118.0	167.5	216.8	0.9	47.9	69.2	113.1	154.2
0.905	86.9	118.0	167.5	216.8	0.905	47.9	69.2	113.1	154.2

0.91	86.9	118.0	167.5	216.8	0.91	47.9	69.2	113.1	154.2
0.915	86.9	118.0	167.5	216.8	0.915	47.9	69.2	113.1	154.2
0.92	86.9	118.1	167.5	216.8	0.92	47.9	69.2	113.1	154.2
0.925	86.9	118.1	167.5	216.8	0.925	47.9	69.2	113.1	154.2
0.93	86.9	118.1	167.5	216.8	0.93	47.9	69.2	113.1	154.2
0.935	86.9	118.1	167.5	216.8	0.935	47.9	69.2	113.1	154.2
0.94	87.0	118.1	167.5	216.8	0.94	47.9	69.2	113.1	154.2
0.945	87.0	118.2	167.5	216.9	0.945	47.9	69.2	113.1	154.2
0.95	87.0	118.2	167.5	216.9	0.95	47.9	69.2	113.1	154.2
0.955	87.0	118.2	167.5	216.9	0.955	47.9	69.2	113.1	154.2
0.96	87.0	118.2	167.5	216.9	0.96	47.9	69.2	113.1	154.2
0.965	87.0	118.2	167.5	216.9	0.965	47.9	69.3	113.1	154.2
0.97	87.0	118.3	167.4	216.9	0.97	47.9	69.3	113.1	154.2
0.975	87.0	118.3	167.4	216.9	0.975	47.9	69.3	113.1	154.2
0.98	87.0	118.3	167.4	216.9	0.98	47.9	69.3	113.1	154.2
0.985	87.0	118.3	167.4	216.9	0.985	47.9	69.3	113.1	154.2
0.99	87.0	118.3	167.4	216.9	0.99	47.9	69.3	113.1	154.2
0.995	87.0	118.4	167.4	217.0	0.995	47.9	69.3	113.1	154.2
1	87.0	118.4	167.4	217.0	1	47.9	69.3	113.1	154.2

1150°C	Effective strain rate (s ⁻¹)				1250°C	Effective strain rate (s ⁻¹)			
Effective strain	0,01	0,1	1	10	Effective strain	0,01	0,1	1	10
0	23.7	32.8	45.5	78.6	0	15.9	18.9	28.5	60.2
0.005	28.6	38.6	53.5	86.4	0.005	19.8	24.4	35.1	65.0
0.01	30.5	40.9	56.7	89.4	0.01	21.1	26.5	37.7	66.9
0.015	31.9	42.6	59.1	91.7	0.015	22.1	28.1	39.7	68.4
0.02	33.0	44.0	61.1	93.6	0.02	22.7	29.4	41.3	69.6
0.025	33.8	45.2	62.8	95.2	0.025	23.2	30.5	42.7	70.6
0.03	34.5	46.3	64.3	96.6	0.03	23.6	31.4	44.0	71.6
0.035	35.2	47.3	65.6	97.8	0.035	23.9	32.2	45.1	72.4
0.04	35.7	48.2	66.8	99.0	0.04	24.1	32.9	46.1	73.2
0.045	36.1	49.0	68.0	100.0	0.045	24.3	33.5	47.0	73.9
0.05	36.5	49.8	69.0	101.0	0.05	24.4	34.0	47.9	74.5
0.055	36.8	50.5	70.0	101.9	0.055	24.5	34.5	48.7	75.1
0.06	37.1	51.1	70.9	102.7	0.06	24.6	34.9	49.5	75.7
0.065	37.3	51.7	71.8	103.5	0.065	24.6	35.3	50.2	76.3
0.07	37.5	52.3	72.6	104.3	0.07	24.7	35.7	50.9	76.8
0.075	37.6	52.8	73.4	105.0	0.075	24.7	36.0	51.5	77.3
0.08	37.8	53.3	74.1	105.7	0.08	24.7	36.2	52.1	77.8
0.085	37.8	53.7	74.8	106.3	0.085	24.6	36.4	52.7	78.2
0.09	37.9	54.1	75.4	106.9	0.09	24.6	36.6	53.3	78.6
0.095	37.9	54.5	76.0	107.5	0.095	24.6	36.8	53.8	79.0
0.1	38.0	54.9	76.6	108.1	0.1	24.5	37.0	54.2	79.4
0.105	38.0	55.2	77.2	108.6	0.105	24.5	37.1	54.7	79.8
0.11	37.9	55.5	77.7	109.1	0.11	24.4	37.2	55.1	80.2

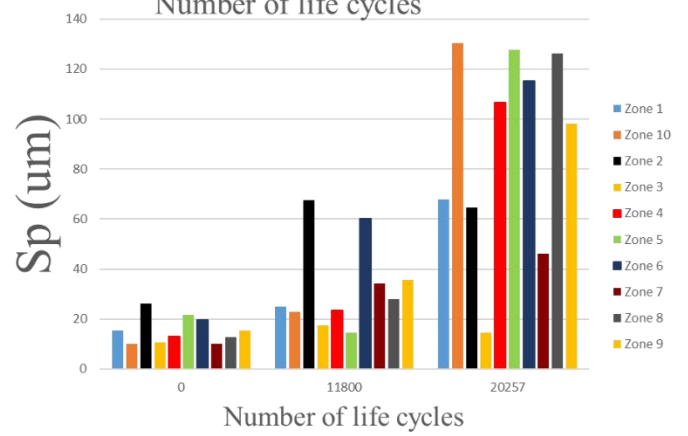
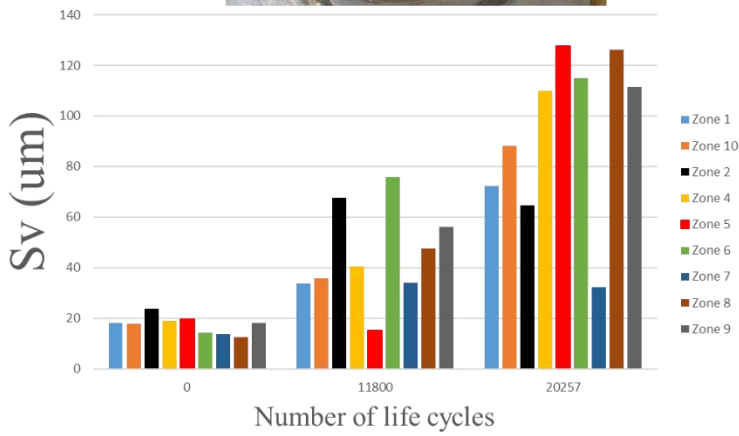
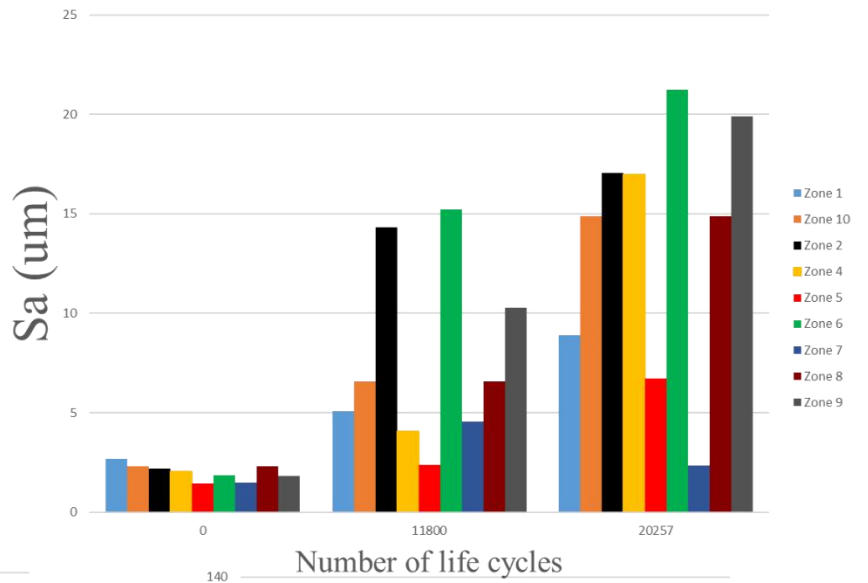
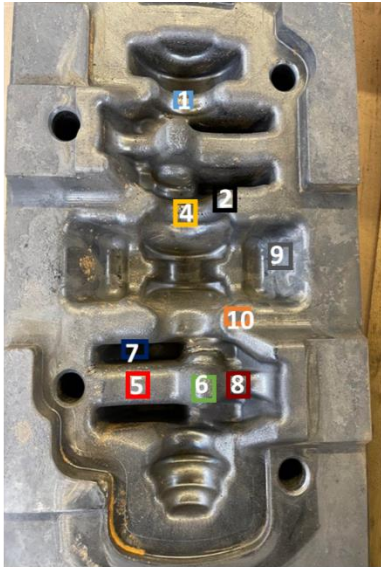
0.115	37.9	55.8	78.3	109.6	0.115	24.4	37.3	55.5	80.5
0.12	37.8	56.0	78.7	110.1	0.12	24.3	37.3	55.9	80.8
0.125	37.8	56.3	79.2	110.6	0.125	24.2	37.4	56.2	81.2
0.13	37.7	56.5	79.6	111.0	0.13	24.2	37.4	56.5	81.5
0.135	37.6	56.6	80.1	111.4	0.135	24.1	37.4	56.8	81.7
0.14	37.5	56.8	80.5	111.8	0.14	24.0	37.4	57.1	82.0
0.145	37.4	56.9	80.8	112.2	0.145	23.9	37.4	57.3	82.3
0.15	37.3	57.0	81.2	112.6	0.15	23.8	37.3	57.5	82.5
0.155	37.2	57.1	81.5	113.0	0.155	23.8	37.3	57.7	82.8
0.16	37.0	57.2	81.9	113.4	0.16	23.7	37.3	57.9	83.0
0.165	36.9	57.2	82.2	113.7	0.165	23.6	37.2	58.0	83.2
0.17	36.8	57.3	82.4	114.0	0.17	23.5	37.1	58.2	83.4
0.175	36.7	57.3	82.7	114.4	0.175	23.4	37.0	58.3	83.6
0.18	36.5	57.2	82.9	114.7	0.18	23.4	36.9	58.4	83.8
0.185	36.4	57.2	83.2	115.0	0.185	23.3	36.8	58.4	83.9
0.19	36.2	57.2	83.4	115.3	0.19	23.2	36.7	58.4	84.1
0.195	36.1	57.1	83.6	115.6	0.195	23.1	36.6	58.5	84.2
0.2	35.9	57.0	83.7	115.8	0.2	23.1	36.5	58.5	84.4
0.205	35.8	56.9	83.9	116.1	0.205	23.0	36.4	58.4	84.5
0.21	35.7	56.8	84.0	116.4	0.21	22.9	36.3	58.4	84.6
0.215	35.5	56.7	84.1	116.6	0.215	22.8	36.1	58.3	84.7
0.22	35.4	56.5	84.2	116.8	0.22	22.8	36.0	58.2	84.8
0.225	35.3	56.4	84.3	117.0	0.225	22.7	35.9	58.1	84.9
0.23	35.1	56.2	84.3	117.2	0.23	22.6	35.7	58.0	84.9
0.235	35.0	56.0	84.4	117.4	0.235	22.6	35.6	57.9	85.0
0.24	34.9	55.8	84.4	117.6	0.24	22.5	35.5	57.8	85.1
0.245	34.7	55.6	84.4	117.8	0.245	22.4	35.3	57.6	85.1
0.25	34.6	55.4	84.3	117.9	0.25	22.4	35.2	57.4	85.1
0.255	34.5	55.2	84.3	118.1	0.255	22.3	35.0	57.3	85.1
0.26	34.4	55.0	84.2	118.2	0.26	22.3	34.9	57.1	85.1
0.265	34.3	54.7	84.2	118.4	0.265	22.2	34.7	56.9	85.1
0.27	34.2	54.5	84.1	118.5	0.27	22.2	34.6	56.7	85.1
0.275	34.1	54.2	84.0	118.6	0.275	22.1	34.4	56.5	85.1
0.28	34.0	54.0	83.8	118.7	0.28	22.1	34.3	56.2	85.1
0.285	33.9	53.7	83.7	118.8	0.285	22.0	34.2	56.0	85.1
0.29	33.8	53.5	83.5	118.8	0.29	22.0	34.0	55.8	85.0
0.295	33.7	53.2	83.4	118.9	0.295	21.9	33.9	55.5	85.0
0.3	33.6	52.9	83.2	118.9	0.3	21.9	33.7	55.3	84.9
0.305	33.5	52.7	83.0	119.0	0.305	21.9	33.6	55.1	84.8
0.31	33.5	52.4	82.8	119.0	0.31	21.8	33.5	54.9	84.8
0.315	33.4	52.1	82.5	119.0	0.315	21.8	33.4	54.6	84.7
0.32	33.3	51.9	82.3	119.0	0.32	21.8	33.2	54.4	84.6
0.325	33.3	51.6	82.1	119.0	0.325	21.7	33.1	54.2	84.5
0.33	33.2	51.3	81.8	119.0	0.33	21.7	33.0	54.0	84.4
0.335	33.1	51.1	81.6	119.0	0.335	21.7	32.9	53.7	84.3
0.34	33.1	50.8	81.3	119.0	0.34	21.7	32.7	53.5	84.2
0.345	33.0	50.6	81.0	119.0	0.345	21.6	32.6	53.3	84.1
0.35	33.0	50.3	80.8	118.9	0.35	21.6	32.5	53.1	83.9

0.355	32.9	50.1	80.5	118.9	0.355	21.6	32.4	53.0	83.8
0.36	32.9	49.9	80.2	118.8	0.36	21.6	32.3	52.8	83.7
0.365	32.8	49.6	80.0	118.7	0.365	21.6	32.2	52.6	83.6
0.37	32.8	49.4	79.7	118.6	0.37	21.6	32.1	52.4	83.4
0.375	32.8	49.2	79.4	118.6	0.375	21.5	32.0	52.3	83.3
0.38	32.7	49.0	79.2	118.5	0.38	21.5	31.9	52.2	83.1
0.385	32.7	48.8	78.9	118.4	0.385	21.5	31.8	52.0	83.0
0.39	32.7	48.6	78.7	118.3	0.39	21.5	31.8	51.9	82.8
0.395	32.6	48.4	78.4	118.1	0.395	21.5	31.7	51.8	82.7
0.4	32.6	48.2	78.2	118.0	0.4	21.5	31.6	51.7	82.5
0.405	32.6	48.0	77.9	117.9	0.405	21.5	31.5	51.6	82.4
0.41	32.6	47.8	77.7	117.8	0.41	21.5	31.5	51.5	82.2
0.415	32.6	47.7	77.5	117.7	0.415	21.5	31.4	51.4	82.1
0.42	32.5	47.5	77.3	117.5	0.42	21.4	31.3	51.3	81.9
0.425	32.5	47.4	77.1	117.4	0.425	21.4	31.3	51.3	81.8
0.43	32.5	47.2	76.9	117.2	0.43	21.4	31.2	51.2	81.6
0.435	32.5	47.1	76.7	117.1	0.435	21.4	31.1	51.2	81.5
0.44	32.5	47.0	76.6	117.0	0.44	21.4	31.1	51.1	81.3
0.445	32.5	46.9	76.4	116.8	0.445	21.4	31.0	51.1	81.1
0.45	32.4	46.8	76.3	116.7	0.45	21.4	31.0	51.0	81.0
0.455	32.4	46.7	76.2	116.5	0.455	21.4	30.9	51.0	80.9
0.46	32.4	46.6	76.0	116.4	0.46	21.4	30.9	51.0	80.7
0.465	32.4	46.5	75.9	116.2	0.465	21.4	30.9	51.0	80.6
0.47	32.4	46.4	75.8	116.1	0.47	21.4	30.8	51.0	80.4
0.475	32.4	46.3	75.7	115.9	0.475	21.4	30.8	51.0	80.3
0.48	32.4	46.2	75.6	115.8	0.48	21.4	30.7	51.0	80.2
0.485	32.4	46.2	75.6	115.6	0.485	21.4	30.7	51.0	80.0
0.49	32.4	46.1	75.5	115.5	0.49	21.4	30.7	51.0	79.9
0.495	32.4	46.1	75.5	115.3	0.495	21.4	30.6	51.0	79.8
0.5	32.4	46.0	75.4	115.2	0.5	21.4	30.6	51.0	79.7
0.505	32.4	46.0	75.4	115.1	0.505	21.4	30.6	51.0	79.6
0.51	32.4	45.9	75.3	114.9	0.51	21.4	30.6	51.0	79.4
0.515	32.4	45.9	75.3	114.8	0.515	21.4	30.5	51.0	79.3
0.52	32.3	45.9	75.3	114.7	0.52	21.4	30.5	51.0	79.2
0.525	32.3	45.8	75.3	114.6	0.525	21.4	30.5	51.0	79.1
0.53	32.3	45.8	75.3	114.4	0.53	21.4	30.5	51.1	79.0
0.535	32.3	45.8	75.2	114.3	0.535	21.4	30.5	51.1	79.0
0.54	32.3	45.8	75.2	114.2	0.54	21.4	30.4	51.1	78.9
0.545	32.3	45.8	75.2	114.1	0.545	21.4	30.4	51.1	78.8
0.55	32.3	45.7	75.2	114.0	0.55	21.4	30.4	51.1	78.7
0.555	32.3	45.7	75.3	113.9	0.555	21.4	30.4	51.2	78.6
0.56	32.3	45.7	75.3	113.8	0.56	21.4	30.4	51.2	78.6
0.565	32.3	45.7	75.3	113.7	0.565	21.4	30.4	51.2	78.5
0.57	32.3	45.7	75.3	113.6	0.57	21.4	30.4	51.2	78.4
0.575	32.3	45.7	75.3	113.6	0.575	21.4	30.3	51.2	78.4
0.58	32.3	45.7	75.3	113.5	0.58	21.4	30.3	51.2	78.3
0.585	32.3	45.7	75.3	113.4	0.585	21.4	30.3	51.3	78.3
0.59	32.3	45.7	75.3	113.3	0.59	21.4	30.3	51.3	78.2

0.595	32.3	45.7	75.4	113.3	0.595	21.4	30.3	51.3	78.2
0.6	32.3	45.7	75.4	113.2	0.6	21.4	30.3	51.3	78.1
0.605	32.3	45.7	75.4	113.2	0.605	21.4	30.3	51.3	78.1
0.61	32.3	45.7	75.4	113.1	0.61	21.4	30.3	51.3	78.1
0.615	32.3	45.7	75.4	113.1	0.615	21.4	30.3	51.4	78.0
0.62	32.3	45.7	75.5	113.0	0.62	21.4	30.3	51.4	78.0
0.625	32.3	45.7	75.5	113.0	0.625	21.4	30.3	51.4	78.0
0.63	32.3	45.7	75.5	113.0	0.63	21.4	30.3	51.4	78.0
0.635	32.3	45.7	75.5	112.9	0.635	21.4	30.3	51.4	77.9
0.64	32.3	45.7	75.5	112.9	0.64	21.4	30.3	51.4	77.9
0.645	32.3	45.8	75.5	112.9	0.645	21.4	30.3	51.5	77.9
0.65	32.3	45.8	75.6	112.8	0.65	21.4	30.3	51.5	77.9
0.655	32.3	45.8	75.6	112.8	0.655	21.4	30.2	51.5	77.9
0.66	32.3	45.8	75.6	112.8	0.66	21.4	30.2	51.5	77.9
0.665	32.3	45.8	75.6	112.8	0.665	21.4	30.2	51.5	77.9
0.67	32.3	45.8	75.6	112.8	0.67	21.4	30.2	51.5	77.8
0.675	32.3	45.8	75.6	112.8	0.675	21.4	30.2	51.5	77.8
0.68	32.3	45.8	75.7	112.8	0.68	21.4	30.2	51.5	77.8
0.685	32.3	45.8	75.7	112.7	0.685	21.4	30.2	51.6	77.8
0.69	32.3	45.8	75.7	112.7	0.69	21.4	30.2	51.6	77.8
0.695	32.3	45.8	75.7	112.7	0.695	21.4	30.2	51.6	77.8
0.7	32.3	45.8	75.7	112.7	0.7	21.4	30.2	51.6	77.8
0.705	32.3	45.8	75.7	112.7	0.705	21.4	30.2	51.6	77.8
0.71	32.3	45.8	75.7	112.7	0.71	21.4	30.2	51.6	77.8
0.715	32.3	45.9	75.8	112.7	0.715	21.4	30.2	51.6	77.8
0.72	32.3	45.9	75.8	112.7	0.72	21.4	30.2	51.6	77.8
0.725	32.3	45.9	75.8	112.7	0.725	21.4	30.2	51.6	77.8
0.73	32.3	45.9	75.8	112.7	0.73	21.4	30.2	51.6	77.9
0.735	32.3	45.9	75.8	112.7	0.735	21.4	30.2	51.6	77.9
0.74	32.3	45.9	75.8	112.7	0.74	21.4	30.2	51.7	77.9
0.745	32.3	45.9	75.8	112.8	0.745	21.4	30.2	51.7	77.9
0.75	32.3	45.9	75.8	112.8	0.75	21.4	30.2	51.7	77.9
0.755	32.3	45.9	75.8	112.8	0.755	21.4	30.2	51.7	77.9
0.76	32.3	45.9	75.9	112.8	0.76	21.4	30.2	51.7	77.9
0.765	32.3	45.9	75.9	112.8	0.765	21.4	30.2	51.7	77.9
0.77	32.3	45.9	75.9	112.8	0.77	21.4	30.2	51.7	77.9
0.775	32.3	45.9	75.9	112.8	0.775	21.4	30.2	51.7	77.9
0.78	32.3	45.9	75.9	112.8	0.78	21.4	30.2	51.7	77.9
0.785	32.3	45.9	75.9	112.8	0.785	21.4	30.2	51.7	77.9
0.79	32.3	45.9	75.9	112.8	0.79	21.4	30.2	51.7	77.9
0.795	32.3	45.9	75.9	112.8	0.795	21.4	30.2	51.7	77.9
0.8	32.3	45.9	75.9	112.8	0.8	21.4	30.2	51.7	77.9
0.805	32.3	46.0	75.9	112.8	0.805	21.4	30.2	51.7	78.0
0.81	32.3	46.0	75.9	112.8	0.81	21.4	30.2	51.7	78.0
0.815	32.3	46.0	75.9	112.9	0.815	21.4	30.2	51.7	78.0
0.82	32.3	46.0	76.0	112.9	0.82	21.4	30.2	51.8	78.0
0.825	32.3	46.0	76.0	112.9	0.825	21.4	30.2	51.8	78.0
0.83	32.3	46.0	76.0	112.9	0.83	21.4	30.2	51.8	78.0

0.835	32.3	46.0	76.0	112.9	0.835	21.4	30.2	51.8	78.0
0.84	32.3	46.0	76.0	112.9	0.84	21.4	30.2	51.8	78.0
0.845	32.3	46.0	76.0	112.9	0.845	21.4	30.2	51.8	78.0
0.85	32.3	46.0	76.0	112.9	0.85	21.4	30.2	51.8	78.0
0.855	32.3	46.0	76.0	112.9	0.855	21.4	30.2	51.8	78.0
0.86	32.3	46.0	76.0	112.9	0.86	21.4	30.2	51.8	78.0
0.865	32.3	46.0	76.0	112.9	0.865	21.4	30.2	51.8	78.0
0.87	32.3	46.0	76.0	112.9	0.87	21.4	30.2	51.8	78.0
0.875	32.3	46.0	76.0	112.9	0.875	21.4	30.2	51.8	78.1
0.88	32.3	46.0	76.0	113.0	0.88	21.4	30.2	51.8	78.1
0.885	32.3	46.0	76.0	113.0	0.885	21.4	30.2	51.8	78.1
0.89	32.3	46.0	76.0	113.0	0.89	21.4	30.2	51.8	78.1
0.895	32.3	46.0	76.0	113.0	0.895	21.4	30.2	51.8	78.1
0.9	32.3	46.0	76.0	113.0	0.9	21.4	30.2	51.8	78.1
0.905	32.3	46.0	76.1	113.0	0.905	21.4	30.2	51.8	78.1
0.91	32.3	46.0	76.1	113.0	0.91	21.4	30.2	51.8	78.1
0.915	32.3	46.0	76.1	113.0	0.915	21.4	30.2	51.8	78.1
0.92	32.3	46.0	76.1	113.0	0.92	21.4	30.2	51.8	78.1
0.925	32.3	46.0	76.1	113.0	0.925	21.4	30.2	51.8	78.1
0.93	32.3	46.0	76.1	113.0	0.93	21.4	30.2	51.8	78.1
0.935	32.3	46.0	76.1	113.0	0.935	21.4	30.2	51.8	78.1
0.94	32.3	46.0	76.1	113.0	0.94	21.4	30.2	51.8	78.1
0.945	32.3	46.0	76.1	113.0	0.945	21.4	30.2	51.8	78.1
0.95	32.3	46.0	76.1	113.0	0.95	21.4	30.2	51.8	78.1
0.955	32.3	46.0	76.1	113.0	0.955	21.4	30.2	51.8	78.1
0.96	32.3	46.0	76.1	113.0	0.96	21.4	30.2	51.8	78.1
0.965	32.3	46.0	76.1	113.0	0.965	21.4	30.2	51.9	78.1
0.97	32.3	46.0	76.1	113.0	0.97	21.4	30.2	51.9	78.1
0.975	32.3	46.0	76.1	113.0	0.975	21.4	30.2	51.9	78.1
0.98	32.3	46.0	76.1	113.1	0.98	21.4	30.2	51.9	78.2
0.985	32.3	46.0	76.1	113.1	0.985	21.4	30.2	51.9	78.2
0.99	32.3	46.1	76.1	113.1	0.99	21.4	30.2	51.9	78.2
0.995	32.3	46.1	76.1	113.1	0.995	21.4	30.2	51.9	78.2
1	32.3	46.1	76.1	113.1	1	21.4	30.2	51.9	78.2

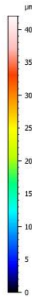
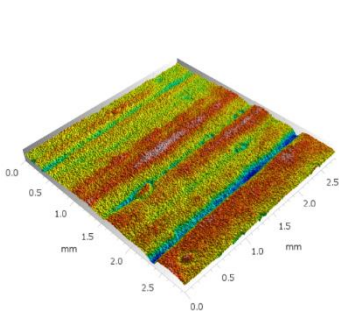
Appendix 2 : Evolution of the topography of the tool as function of lifecycles.



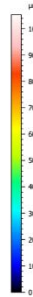
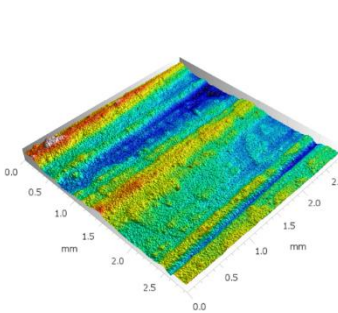
Appendix 3 : Evolution of the topography of the WHUST specimens as function of lifecycles.

Flat 270 MPa

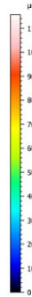
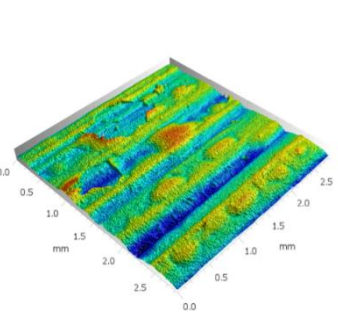
0 Cycle



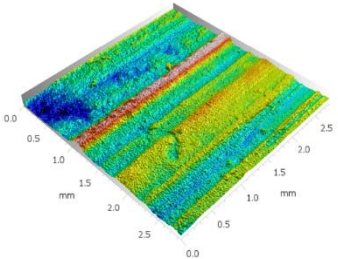
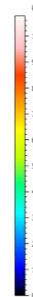
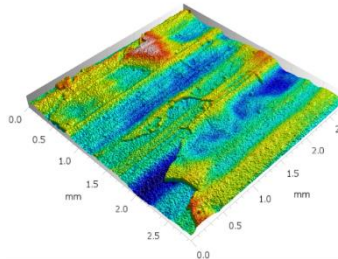
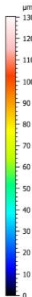
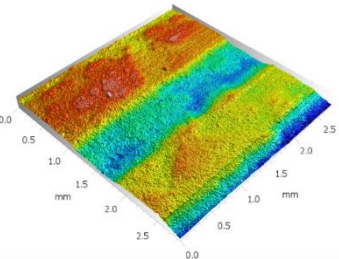
11,800 Cycles



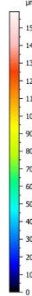
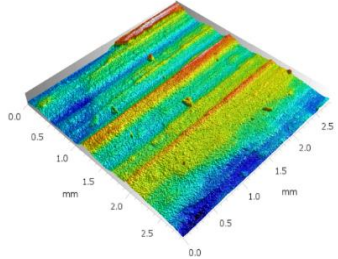
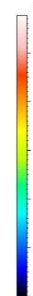
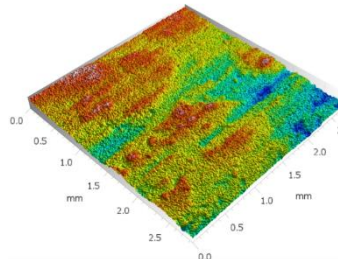
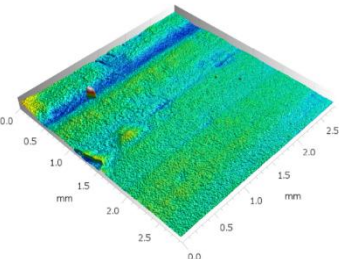
20,000 Cycles



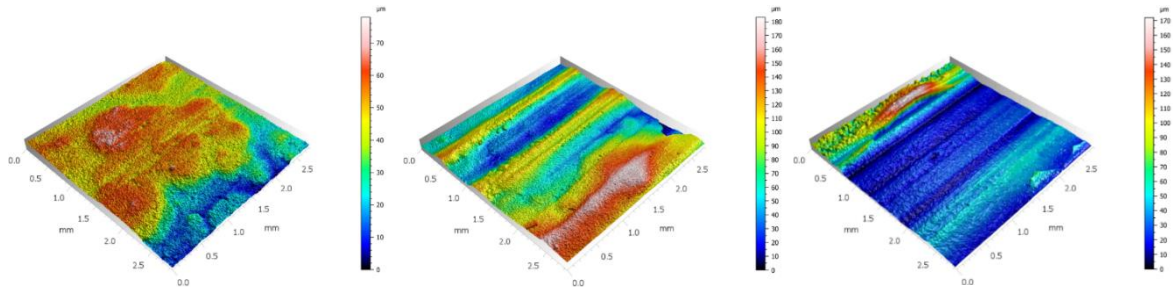
Concave 150 MPa



Flat 100 MPa



Convex 200 MPa



Flat 100 MPa

